

October 6, 2020

Comparative Roles of Charge, π and Hydrophobic Interactions in Sequence-Dependent Phase Separation of Intrinsically Disordered Proteins

Suman DAS,¹ Yi-Hsuan LIN,^{1,2} Robert M. VERNON,² Julie D. FORMAN-KAY^{2,1}
and Hue Sun CHAN^{1,*}

¹Department of Biochemistry, University of Toronto, Toronto, Ontario M5S 1A8, Canada;

²Molecular Medicine, Hospital for Sick Children, Toronto, Ontario M5G 0A4, Canada

*Corresponding author

E-mail: chan@arrhenius.med.utoronto.ca; Tel: (416)978-2697; Fax: (416)978-8548

Mailing address:

Department of Biochemistry, University of Toronto, Medical Sciences Building – 5th Fl.,
1 King's College Circle, Toronto, Ontario M5S 1A8, Canada.

Abstract

Endeavoring toward a transferable, predictive coarse-grained explicit-chain model for biomolecular condensates underlain by liquid-liquid phase separation (LLPS) of proteins and nucleic acids, we conducted multiple-chain simulations of the N-terminal intrinsically disordered region (IDR) of DEAD-box helicase Ddx4, as a test case, to assess the roles of electrostatic, hydrophobic, cation- π , and aromatic interactions in amino acid sequence-dependent LLPS. We evaluated three different residue-residue interaction schemes with a shared electrostatic potential. Neither a common hydrophobicity scheme nor one augmented with arginine/lysine-aromatic cation- π interactions consistently accounted for the available experimental LLPS data on the wildtype, a charge-scrambled, a phenylalanine-to-alanine (FtoA), and an arginine-to-lysine (RtoK) mutant of Ddx4 IDR. In contrast, interactions based on contact statistics among folded globular protein structures reproduce the overall experimental trend, including that the RtoK mutant has a much diminished LLPS propensity. Consistency between simulation and LLPS experiment was also found for RtoK mutants of P-granule protein LAF-1, underscoring that, to a degree, the important LLPS-driving π -related interactions are embodied in classical statistical potentials. Further elucidation will be necessary, however, especially of phenylalanine's role in condensate assembly because experiments on FtoA and tyrosine-to-phenylalanine mutants suggest that LLPS-driving phenylalanine interactions are significantly weaker than those posited by common statistical potentials. Protein-protein electrostatic interactions are modulated by relative permittivity, which in general depends on aqueous protein concentration. Analytical theory suggests that this dependence entails enhanced inter-protein interactions in the condensed phase but more favorable protein-solvent interactions in the dilute phase. The opposing trends lead to only a modest overall impact on LLPS.

Significance Statement

Mesoscopic condensates of proteins and nucleic acids, including various “membraneless organelles”, serve myriad biological functions, whereas dysregulation of condensates can cause disease. Deciphering how condensates are governed by genetically encoded biomolecular sequences is of central importance. Critical assessment of how various interactions reproduce experimental phase behaviors indicates that π -interactions’ notable facilitation of condensate formation is well reflected in established contact statistics among folded protein structures, although the condensate-driving capability of the large hydrophobic/aromatic residue phenylalanine is weaker than expected. By elucidating physical aspects of the residue-residue contacts in condensates, highlighting these contacts’ largely solvent-exposed character with ramifications such as reduced hydrophobic strengths relative to buried non-polar contacts, fundamental conceptual and quantitative progress is made toward predictive models for biomolecular condensates.

INTRODUCTION

A preponderance of recent advances demonstrate that liquid-liquid phase separation (LLPS) of intrinsically disordered proteins (IDPs), proteins containing intrinsically disordered regions (IDRs), folded proteins, and nucleic acids is a general biophysical mechanism to achieve functional spatial and temporal organization of biomolecules in both intra- and extra-cellular organismal space.^{1–9} LLPS underpins formation of a variety of biomolecular condensates,¹⁰ including intracellular bodies, such as nucleoli and stress granules, that are often referred to as membraneless organelles,^{4,11} and precursor of extracellular materials as in the case of sandcastle worm adhesive¹² and elastin in vertebrate tissues⁸. These dynamic, phase-separated condensates perform versatile functions, as underscored by their recently elucidated roles in synapse formation and plasticity,^{7,13} organization of chromatin,¹⁴ regulation of translation,^{15,16} B cell response,¹⁷ and autophagosome formation.¹⁸ The pace of discovery in this very active area of research has been accelerating.^{19–28}

While experimental progress has been tremendous, theory for the physico-chemical basis of biomolecular condensates is still in its infancy. Biomolecular condensates *in vivo* are complex, involving many species of proteins and nucleic acids maintained often by non-equilibrium processes,^{10,19,29–31} rendering atomistic modeling impractical. Facing this challenge, promising initial theoretical steps using coarse-grained approaches were made to tackle simpler *in-vitro* LLPS systems, as their elucidation is a prerequisite for physical insights into more complex *in vivo* condensates. These recent efforts encompass analytical theories at various levels of approximation,^{32–42} field theory simulations,^{43–46} and lattice^{47–49,51} or continuum^{50,52–54} coarse-grained explicit-chain simulations that account for either individual amino acid residues^{47,52,53,55} or, at lower structural resolution, groups of residues^{56,57}—including using patchy particle representations.^{58,59} The different theoretical/computational approaches are complementary, and were applied to address how amino acid composition (number/fraction of hydrophobic,⁵⁴ aromatic,^{39,60} or charged⁴ residues) and the sequence pattern of charge,^{34,48,53,61} hydrophobic,^{50,51,54} or aromatic⁶⁰ residues affect LLPS propensity of heteropolymers as well as pertinent impact of temperature,^{20,43,50,54} hydrostatic pressure,^{62–64} salt,^{41,46} and osmolyte,^{27,63} offering physical insights into the LLPS behaviors of, for example, the DEAD-box RNA helicase Ddx4,^{34,65} RNA-binding protein fused in sarcoma (FUS),⁵² prion-like domains,⁶⁰ and postsynaptic densities.⁶⁴

Developing LLPS models with transferable interaction potentials applicable to a wide range of amino acid sequences is essential for advancing fundamental physical understanding of natural biomolecular condensates and engineering of bio-inspired materials.⁶⁶ In this endeavor, the rapidly expanding repertoire of experimental data offers critical assessment of theoretical and computational approaches. Building on aforementioned progress,^{34,41,52,53} the present study evaluates a variety of interaction schemes for coarse-grained residue-based chain simulations of LLPS of IDPs or IDRs, including but not limited to schemes proposed in the literature.⁵² We do so by first comparing their sequence-specific predictions against

experiment on the RNA helicase Ddx4 for which extensive LLPS data on the wildtype (WT) and three mutant sequences are available to probe the contribution of hydrophobic, electrostatic,⁴ cation- π , and possibly other π -related^{4,65,68} interactions. We use these data to benchmark the relative strengths of different types of interaction in our model. Of particular interest are the aromatic⁶⁷ and other π -related⁶⁸ interactions, which have significant impact on folded protein structure, conformational distribution of IDPs and LLPS properties,^{4,34,39,60,69–73} but are often not adequately accounted for in model potentials.⁶⁸ Interestingly, a simple statistical potential based upon folded protein structures^{74,75} accounts for the general trend of LLPS properties of the four Ddx4 IDR sequences, including LLPS is more favored by arginine than lysine despite their essential identical electric charges, but a model potential that rely solely on hydrophobicity⁷⁶ does not. This finding indicates that, at the coarse-grained level of residue-residue interactions, IDP/IDR LLPS is governed largely by similar forces—including the π -related ones—that drive protein folding. Analogous agreement between statistical potential model prediction and experiment with respect to the arginine/lysine contrast is also found for the N-terminal RGG domain of P-granule RNA Ddx3 helicase LAF-1.⁷⁷ However, experimental data on tyrosine-to-phenylalanine mutants of LAF-1 and FUS³⁹ indicate that the contribution of the large aromatic residue phenylalanine to LLPS is overestimated by statistical potentials, most likely because the interactions involving phenylalanine in the sequestered hydrophobic core of globular proteins are not sufficiently representative of more solvent-accessible LLPS-driving interactions, pointing to a crucial aspect of LLPS energetics that future investigations should be directed. To gain further insights into the electrostatic driving forces for LLPS, we have conducted explicit-water simulation and develop new analytical theory which suggest, at variance with previous analyses,^{35,37} that the physically expected dependence of effective permittivity on IDR concentration may have a modest instead of drastic impact on LLPS propensity because of a tradeoff between solvent-mediated electrostatic interchain interactions and self-interactions. These findings and their ramifications are discussed below.

RESULTS AND DISCUSSION

As described in Materials and Methods and SI Appendix, SI Text, our coarse-grained protein chain model for IDP LLPS basically follows the approaches in Refs. 52, 53, which in turn are based on a recently proposed efficient simulation protocol.⁷⁸ In the first step of our analysis, we critically assess the models against the experimental data on the Ddx4 IDR (SI Appendix, Fig. S1), which indicate that all three Ddx4 IDR mutants—the charge scrambled (CS), phenylalanine-to-alanine (FtoA), and arginine-to-lysine (RtoK) variants—have significantly reduced LLPS propensities relative to the WT.^{4,65,68} The CS, FtoA, and RtoK variants are useful probes for LLPS energetics. They were constructed specifically to study the experimental effects of sequence charge pattern (the arrangement of charges along CS sequence is less blocky than that in WT while the amino acid composition is unchanged),

the relative importance of aromatic/ π -related vs hydrophobic/nonpolar interactions (all 14 Phe residues in WT Ddx4 IDR are mutated to Ala in FtoA), and the role of Arg vs Lys (all 24 Arg residues in WT IDR are mutated to Lys in RtoK) on the LLPS of Ddx4.

Assessing Biophysical Perspectives Embodied by Different Coarse-Grained Interaction Schemes For Modeling Biomolecular Condensates. We consider the potential functions in the hydrophobicity-scale (HPS) and the Kim-Hummer (KH) models in Dignon et al.⁵² as well as the HPS potential with augmented cation- π terms,⁷² all of which share the same bond energy term, U_{bond} , for chain connectivity and screened electrostatic term, U_{el} , for pairs of charged residues, as described in SI Appendix, SI Text. We focus first on the pairwise contact interactions between amino acid residues, which correspond to the U_{aa} energies of either the HPS or KH model (excluding U_{bond} and U_{el}).

The HPS model assumes that the dominant driving force for IDP LLPS is hydrophobicity as characterized by a scale for the 20 amino acid residues. Pairwise contact energy is taken to be the sum of the hydrophobicities of the two individual residues of the pair. The HPS model adopts the scale of Kapcha and Rossky, in which the hydrophobicity of a residue is a composite quantity based on a binary hydrophobicity scale of the atoms in the residue.⁷⁶

In contrast, the KH model⁷⁹ relies on knowledge-based potentials derived from contact statistics of folded protein structures in the Protein Data Bank (PDB). As such, it assumes that the driving forces for IDP LLPS are essentially identical to those for protein folding at a coarse-grained residue-by-residue level, as obtained by Miyazawa and Jernigan,⁷⁵ without singling out a priori a particular interaction type as being dominant.

The HPS model has been applied successfully to study the FUS low-complexity-domain,⁸⁰ the RNA-binding protein TDP-43,⁸¹ and the LAF-1 RGG domain as well as its charge shuffled variants.⁷⁷ A temperature-dependent version of HPS (HSP-T)⁵⁰ was also able to rationalize the experimental LLPS properties of artificial designed sequences.⁸² When both the HPS and KH models were applied to FUS and LAF-1, the predicted phase diagrams were qualitatively similar for a given sequence though they exhibited significantly different critical temperatures,⁵² which should be attributable to the difference in effective energy/temperature scale of the two models. Here we conduct a systematic assessment of the two models' underlying biophysical assumptions by evaluating their ability to provide a consistent rationalization of the LLPS properties of a set of IDR sequences.

The scatter plot in Fig. 1a of HPS and KH energies indicates that, despite an overall correlation, there are significant outliers. The most conspicuous outliers are interactions involving Arg (red), which are much less favorable in HPS than in KH. By comparison, most of the interactions involving Pro, as depicted by the 16 outlying blue circles as well as the single yellow and single green circles to the left of the main trend, are considerably more favorable in HPS than in KH. Interactions involving Phe (yellow) and Lys (green) essentially follow the main trend. Those involving Phe are favorable to various degrees in both models. However, some interactions involving Lys are attractive in HPS but repulsive in KH. For example, Lys-Lys interaction is attractive at ≈ -0.1 kcal mol⁻¹ for HPS but is repulsive

at $\approx +0.2$ kcal mol⁻¹ for KH. Figure 1b underscores the difference in interaction pattern of the two models for the WT Ddx4 IDR. The KH pattern is clearly more heterogeneous with both attractions and repulsions, whereas the HPS pattern is more uniform with no repulsive interactions. These differences should lead to significantly different predictions in sequence-dependent LLPS properties, as will be explored below.

Because of the importance of cation- π interactions in protein folded structure⁶⁹ as well as conformational distribution of IDP and LLPS,^{4,39,72,73,77} we study another set of model interaction schemes—in addition to HPS and KH, referred to as HPS+cation- π —that augment the HPS potentials with terms specific for cation- π interactions between Arg or Lys and the aromatic Tyr, Phe, or Trp (Fig. 2). As explained in the SI Appendix, SI Text, we consider two alternate scenarios: (i) the cation- π interaction strength is essentially uniform, irrespective of the cation-aromatic pair (Fig. 2a), as suggested by an earlier analysis;⁶⁹ and (ii) the cation- π interaction strength is significantly stronger for Arg than for Lys (Fig. 2b). The latter scheme is motivated by recent experiments showing that Arg to Lys substitutions reduce LLPS propensity, as in the cases of the RtoK mutant of Ddx4 IDR⁶⁸ and variants of FUS³⁹ and LAF-1,⁷⁷ as well as a recent theoretical investigation pointing to different roles of Arg and Lys in cation- π interactions.⁸³ Contact statistics of PDB structures, including those of Miyazawa and Jernigan^{74,75} on which the KH potential is based, may also suggest that Arg- π attractions are stronger than Lys- π 's. Indeed, among a set of 6,943 high-resolution X-ray protein structures,⁶⁸ we find that an Arg-aromatic pair is at least 75% more likely than a Lys-aromatic pair to be within a C _{α} -C _{α} distance of ≤ 6.5 Å (SI Appendix, Fig. S2), a separation that is often taken as a criterion for residue-residue contact.⁷⁴ On top of that, given an Arg-aromatic and a Lys-aromatic pair are separated by the same C _{α} -C _{α} distance (Fig. 2c), the Arg-aromatic pair (solid curves) are more likely than the Lys-aromatic pair (dashed curves) to adopt configurations consistent with a cation- π interaction. We emphasize, however, that although a significantly stronger Arg- than Lys-associated cation- π interaction is explored here as an alternate scenario, it is probable, as argued by Gollivan and Dougherty using a comparison between Lys-like ammonium-benzene and Arg-like guanidinium-benzene interactions, that the strengths of the “pure” cation- π parts of Arg- and Lys-aromatic interactions are similar despite the relative abundance of Arg-aromatic contacts due to other factors⁶⁹ such as π - π effects.⁶⁸

Hydrophobicity, Electrostatics And Cation- π Interactions Are Insufficient By Themselves To Rationalize Ddx4 LLPS Data In Their Entirety. We begin our assessment of models by applying the HPS and HPS+cation- π potentials to simulate the phase diagrams of the four Ddx4 IDRs (SI Appendix, Fig. S1), the sequence patterns of which are illustrated in Fig. 3a using a style employed previously, e.g., in Refs. 4, 34, 39. The phase diagrams presented here are coexistence curves. When the overall average IDR density lies in between the left and right arms of the coexistence curve at a given temperature, the system phase separates into a dilute phase and a condensed phase with IDR densities given, respectively, by the low- and high-density values of the coexistence curve at the given

temperature. When the average IDR density is not in the region underneath the coexistence curve, the system is not phase separated (see, e.g., Refs. 20, 35, 84 for introductory discussions). Consistent with experiments,^{4,65} the simulated phase diagrams (Fig. 3b) exhibit upper critical solution temperatures, which is a maximum temperature above which phase separation does not occur (corresponding to the local maxima of the coexistence curves at IDR density ≈ 200 mg/ml in Fig. 3). We emphasize, however, that although the simulated critical temperatures are assuringly in the same range as those deduced experimentally,⁶⁵ the model temperature (in K) of our simulated phase diagrams in Figs. 3b and 4 should not be compared directly with experimental temperature. This is because not only of uncertainties about the overall model energy scale but also because the models do not account for the temperature dependence of effective residue-residue interactions.^{20,43,50} For simplicity, our models include only temperature-independent energies as they are purposed mainly for comparing the LLPS propensities of different amino acid sequences on the same footing rather than for highly accurate prediction of LLPS behaviors of any individual sequence.

The leftmost panel of Fig. 3b provides the HPS phase diagrams at relative permittivity $\epsilon_r = 80$ (approximately equal to that of bulk water, as in Ref. 52). The predicted behaviors of the CS and FtoA variants are consistent with experiments in that their LLPS propensities are reduced relative to WT;^{4,65} but the predicted enhanced LLPS propensity of RtoK is opposite to the experimental finding of Vernon et al. that the LLPS propensity of RtoK is lower than that of WT.⁶⁸ This shortcoming of the HPS model is a consequence of its assignment of much less favorable interactions for Arg than for Lys, as noted in Fig. 1a.

The other panels of Fig. 3b provide the HPS+cation- π phase diagrams. They are computed for $\epsilon_r = 80, 40,$ and 20 to gauge the effect of electrostatic interactions relative to other types of interactions. The ϵ_r -dependent results are also preparatory for our subsequent investigation of the effect of IDR-concentration-dependent permittivity^{35,37} on predicted LLPS properties. All of the HPS+cation- π phase diagrams here still disagree with experiment^{65,68} as they all predict a higher LLPS propensity for the RtoK variant than for WT. Apparently, the bias of the HPS potential against Arg interactions is so strong that it cannot be overcome by additional Arg-aromatic interactions that are reasonably more favorable than Lys-aromatic interactions (Fig. 2b). The $\epsilon_r = 80$ results for both uniform and variable cation- π strength exhibit an additional mismatch: Contrary to experiments,^{4,65} they predict similar LLPS propensities for the CS variant and WT, suggesting that under this dielectric condition, electrostatic interactions are unphysically overwhelmed by the presumed cation- π interactions. The $\epsilon_r = 20$ results for variable cation- π also indicate an additional mismatch, in this case they fail to reproduce the experimental trend of a significantly lower LLPS propensity of the FtoA variant relative to that of WT,⁴ probably because the relatively weak cation- π contribution is overwhelmed by strong electrostatic interactions in this low- ϵ_r situation. Taken together, although a perspective involving only electrostatic and cation- π interactions was adequate to account for sequence-specific LLPS trend of WT and CS (and possibly also FtoA) before the RtoK experiment was performed,³⁴ such a perspective is

incomplete when RtoK enters the picture. Fig. 3b shows that the HPS+cation- π model, which takes into account hydrophobic, charged, and cation- π interactions, cannot account for the general trend of available Ddx4 LLPS data. It follows that these interactions—at least when hydrophobicity is accorded by the particular scale⁷⁶ adopted by HPS—are insufficient by themselves to account for LLPS of IDRs in general.

Structure-Based Statistical Potentials Provide An Approximate Account Of π -Related Driving Forces for Ddx4 LLPS. In contrast to the HPS and HPS+cation- π models, direct application of the KH model—without augmented cation- π terms—leads to an overall trend largely in agreement with experiments^{4,65,68} for the ϵ_r values tested, i.e., all three Ddx4 IDR variants are predicted by the KH potential to have lower LLPS propensities than WT (Fig. 4). For WT at $\epsilon_r = 80$ and $T = 300$ K, the simulated condensed phase density of ~ 500 mg ml⁻¹ is comparable to the experimental value of ~ 400 mg ml⁻¹ with [NaCl] = 100 mM at the same temperature (Ref. 65). Similar KH- and HPS-simulated condensed phase densities were obtained for FUS and LAF-1 IDRs.⁵² Illustrations of our simulated chain configurations are provided in Fig. 5. Time-dependent mean-square deviation of molecular coordinates have been used to verify liquid-like chain dynamics in the condensed phase of HPS and KH models.⁵² Examples of similar calculation are provided in SI Appendix, Fig. S3 and S4 for the Ddx4 IDRs examined in this work.

This success of the KH model suggests that empirical, knowledge-based statistical potentials derived from the PDB may capture key effects governing both protein folding and IDR LLPS without prejudging the dominance of, or lack thereof, particular types of energetics such as hydrophobicity in the HPS model. In this respect, it would not be surprising that cation- π and other π -related interactions are reflected in these knowledge-based potentials as well. After all, the importance of cation- π interactions in folded protein structure⁶⁹ and π - π interactions in IDR LLPS⁶⁸ is recognized largely by bioinformatics analyses of the PDB.

As discussed above, a major cause of the shortcoming of HPS in accounting for the LLPS of Ddx4 IDRs (Fig. 3b) is the high degree of unfavorability it ascribes to Arg interactions. Its hydrophobicity scale, based on the atomic partial charges in the OPLS forcefield, posits that Arg has the least hydrophobicity value of +14.5, the next-least hydrophobic is Asp with +7.5, whereas Lys has +5.0, and the most hydrophobic is Phe with -4.0 (Ref. 76). This assignment results in highly unfavorable Arg-associated interactions relative to Lys-associated interactions. In the HPS model, when one of the residues, i , in the pairwise energy $E_{ij}(r_0)$ (Fig. 1a) is Arg, the average of $E_{ij}(r_0)$ over j for all amino acids except the charged residues Arg, Lys, Asp, and Glu is equal to -0.0762 in units of kcal mol⁻¹, whereas the corresponding average for Lys is much more favorable at -0.1276. When the charged residues are included, the trend is the same with the average being -0.0677 for Arg and -0.119 for Lys. In contrast, for the KH model, the trend is opposite with Arg-associated interactions much more favorable: the corresponding average is -0.123 for Arg and -0.041 for Lys when charged residues are excluded in the averaging and -0.0990 for Arg and -0.0161 for Lys when charge residues are included. This trend echoes an earlier eigenvalue

analysis of the Miyazawa-Jernigan energies⁷⁵ (which underlie the KH potential) indicating that Arg has a significantly larger projection than Lys along the dominant eigenvector.⁹⁰

Whereas correlation among hydrophobicity scales inferred from different methods is limited^{85–88} with significant variations especially for the nonhydrophobic polar and charged residues,⁸⁶ the extremely low hydrophobicity assigned by HPS^{52,76} to Arg relative to Lys is unusual. For instance, Lys is substantially less hydrophobic than Arg in two of the three scales tabulated and compared in Ref. 88. In a commonly-utilized scale based on the free energies of transfer of amino acid derivatives from water to octanol measured by Fauchère and Pliška⁸⁹ (the second scale tabulated in Ref. 88), Arg is only slightly less hydrophobic (+5.72 kJ mol⁻¹) than Lys (+5.61 kJ mol⁻¹) and thus, essentially, Arg and Lys are deemed to possess equally low hydrophobicities. Accordingly, this scale affords a better correlation with the Miyazawa-Jernigan energies⁷⁵ (Fig. 3b of Ref. 88) than that exhibited in Fig. 1a.

It is reasonable to expect the 210 (or more) residue-residue contact energy parameters in PDB-structures-based potentials to contain more comprehensive energetic information than merely the hydrophobicities of the 20 types of amino acid residues. In this regard, it is notable that a higher propensity for Arg than Lys to engage favorably with another residue appears to be a robust feature of PDB statistics. It holds for the cation-aromatic pairs we analyze in SI Appendix, Fig. S2, for the KH potential, and also for the original Miyazawa-Jernigan energies put forth in 1985.⁷⁴ According to Table V of Ref. 74, the contact energies e_{ij} between Arg and aromatic or negatively charged residues are -3.54 , -3.56 , -2.75 , -2.07 , and $-1.98k_B T$, respectively, for Arg-Phe, Arg-Trp, Arg-Tyr, Arg-Glu, and Arg-Asp (k_B is Boltzmann constant, T is absolute temperature), whereas the corresponding contact energies are weaker for Lys at -2.83 , -2.49 , -2.01 , -1.60 , and $-1.32k_B T$, respectively, for Lys-Phe, Lys-Trp, Lys-Tyr, Lys-Glu, and Lys-Asp. All twenty Arg interactions are more favorable than the corresponding Lys interactions. The average e_{ij} over all Arg-associated pairs is $-2.22k_B T$, which is substantially more favorable than the corresponding average of $-1.4795k_B T$ for the Lys-associated pairs. It is apparent from the present application of KH to the Ddx4 IDRs that this feature is crucial, at least at a coarse-grained level, for an adequate accounting of the π -related energetics of biomolecular LLPS. Physically, the general preference for Arg- π over Lys- π contacts is underpinned in part by the Arg geometry which allows for favorable guanidinium-aromatic coplanar packing,⁷¹ as discussed recently by Wang et al. (Ref. 39 and references therein) and that Arg-aromatic is less attenuated by the aqueous dielectric medium because it is less dominated than Lys-aromatic interactions by electrostatics.⁸³ Consistent with this perspective, RtoK mutants of FUS³⁹ and LAF-1 RGG⁷⁷ also exhibit substantially reduced LLPS propensity relative to WT.

Phenylalanine Interactions in Liquid Condensates, Expected to be More Solvent-Exposed, are Weaker than Statistical Estimates Based on Mostly Core Phenylalanine Contacts in Folded Proteins. To assess further the generality of the KH model, we apply it to simulate the phase behavior of WT LAF-1 and its RtoK and tyrosine-to-phenylalanine (YtoF) mutants (Fig. 6, and SI Appendix, Fig. S5). Simulation

studies of LLPS of full-length and the RGG IDR⁵² of LAF-1, including the latter’s charge shuffled variants,⁷⁷ have been conducted extensively using the HPS^{52,77} and KH⁵² models to gain valuable insights; but phase behaviors of the RtoK and YtoF LAF-1 RGG mutants have not been simulated using these models. Recent experiments indicate that the RtoK mutant does not phase separate under the conditions tested, whereas the LLPS propensity of the YtoF mutant is reduced relative to that of WT.⁷⁷ As for the Ddx4 IDR, the KH-predicted coexistence curve for RtoK in Fig. 6 (purple curve) is consistent with the experimental trend, as it has a far lower critical temperature than that of the WT (red curve). However, KH posits a significantly higher LLPS propensity for YtoF (green dashed curve with a much higher critical temperature), which is opposite to experimental observation. On closer inspection, the basic feature that causes this shortcoming is that KH deems Phe interactions more favorable than Tyr interactions. According to KH, $E_{ij}(r_0)$ for $i = \text{Phe}$ averaged over j for all amino acids is $-0.453 \text{ kcal mol}^{-1}$ for Phe, which is significantly more negative than the corresponding average $E_{ij}(r_0)$ of $-0.281 \text{ kcal mol}^{-1}$ for Tyr. For this reason, KH is unlikely to reproduce the experimentally observed reduced LLPS propensities for any other YtoF mutant either, including the YtoF mutants of FUS.³⁹

This overestimation of the favorability of Phe-related interactions in the LLPS context also causes the KH-predicted LLPS propensity of the FtoA mutant of Ddx4 IDR (Fig. 4, green curves) to be substantially lower than that of the RtoK mutant (purple curves). Experimentally, however, FtoA mutant LLPS is observed at $\sim 350 \text{ mg ml}^{-1}$ protein concentration, but the RtoK mutant does not phase separate up to 400 mg ml^{-1} (in comparison, LLPS of WT is observed at 25 mg ml^{-1}).⁶⁸ In other words, the KH-predicted rank ordering of LLPS propensities of Ddx4 FtoA and RtoK is opposite to experiment. This is because the KH energy $E_{ij}(r_0)$ for Ala averaged over all 20 residue types, at $-0.160 \text{ kcal mol}^{-1}$, is much less favorable than the corresponding $-0.453 \text{ kcal mol}^{-1}$ for Phe, and that the change in average KH $E_{ij}(r_0)$ from Phe to Ala ($-0.160 + 0.453 = +0.293 \text{ kcal mol}^{-1}$) is far larger than the corresponding change of $-0.0161 + 0.0990 = +0.0829 \text{ kcal mol}^{-1}$ from Arg to Lys.

Interestingly, while these Ala-, Tyr-, and Phe-related KH energies do not reproduce experimental observations for YtoF and FtoA mutants, the KH energies are largely in line with rank ordering in common hydrophobicity scales. For instance, in the water-to-octanol scale of Fauchère and Pliška,⁸⁹ the transfer free energies for Ala, Tyr, and Phe are, respectively, -1.76 , -5.44 , $-10.1 \text{ kJ mol}^{-1}$. By comparison, the average interaction energies in the HPS model for Ala, Tyr, and Phe differ less—being -0.141 , -0.154 , and $-0.168 \text{ kcal mol}^{-1}$, respectively; but Phe-related interactions are still generally more favorable than Tyr-related interactions. Thus, HPS is not only insufficient to account for RtoK experiments (Fig. 3), HPS is not expected to capture the observed YtoF trend either.

The above consideration underscores once again that the energetic contributions of amino acid residues to LLPS are not necessarily dominated by their hydrophobicities. Phe is generally considered to be more hydrophobic than Tyr. However, even for the globular proteins ribonuclease Sa and Sa3, 14 out of 16 YtoF single-site substitutions destabilize the

folded state. One of the physical reasons for this behavior is that the Tyr hydroxyl group—which is absent in Phe—makes a hydrogen bond with the N^ε atom of an Arg residue.⁹¹ It would be enlightening to investigate whether similar hydrogen bonding effects account to any degree for the preference for Tyr–Arg over Phe–Arg interactions in the LLPS context.

For a relative large residue that possesses both hydrophobic and aromatic properties such as phenylalanine, the character of its LLPS-driving contributions can also differ significantly from those stabilizing the well-packed core of a folded protein, because most residue-residue contacts in the LLPS context are at least partially exposed to solvent even in the condensed phase. This observation offers a perspective to understand KH’s inability to capture LLPS behaviors of YtoF and FtoA mutants because KH is derived from statistical potentials which in turn are based upon contact frequencies in folded proteins. Since Phe is one of the most buried residues in folded proteins with on average 0.88 of its surface area inaccessible to solvent upon folding (the corresponding fractions for Tyr, Ala, Lys, and Arg are, respectively, 0.76, 0.74, 0.52, and 0.64),⁹² the difference in character between Phe’s LLPS-driving and folded-state-stabilizing interactions is expected to be more prominent.

Indeed, it has long been recognized that “pair” interactions in solvent-exposed environments have properties—including thermodynamic signatures^{93,94}—that are distinctly different from those of “bulk” interactions quantified by common hydrophobicity measurements.⁹⁵ In this regard, computational evidence suggests that Phe-related interaction in a highly solvent accessible environment—which is more pertinent to LLPS—is not substantially stronger than Ala-related interactions. For instance, using ethane and ethylbenzene as models, respectively, for Ala and Phe, explicit-TIP3P water simulations of pairwise potentials of mean force (PMFs) at 298 K by Makowski et al. indicate that the lowest free energies at the ethane-ethane, ethane-ethylbenzene,⁹⁶ and ethylbenzene-ethylbenzene⁹⁷ contact minima are all ≈ -1 kcal mol⁻¹ (Tyr was not considered in these studies^{96,97}). Thus, in contrast to the vastly different Ala-Ala, Ala-Phe, and Phe-Phe interaction strengths in KH, with $E_{ij}(r_0) = -0.142, -0.425, \text{ and } -0.756$ kcal mol⁻¹, respectively,⁵² these explicit-water PMFs suggest a more modest difference in interaction strength between Ala and Phe in the LLPS context, which would be in line with the FtoA experiment. With this knowledge, future investigations should tackle hitherto overlooked features of solvent-accessible contacts among amino acid residues to improve coarse-grained interaction potentials for LLPS.

IDR Concentration Can Significantly Affect The Dielectric Environment Of Condensed Droplets But Its Impact On LLPS Propensity Can Be Modest. In recent^{52,53,55} and the above coarse-grained, implicit-solvent simulations of LLPS of IDRs, electrostatic interactions are assumed, for simplicity, to operate in a uniform dielectric medium with a position-independent ϵ_r . However, the dielectric environment is certainly nonuniform upon LLPS: The electrostatic interaction between two charges are affected to a larger extent by the intervening IDR materials in the condensed phase—where there is a higher IDR concentration—than in the dilute phase. Protein materials have lower ϵ_r s than bulk water.^{98–100} Analytical treatments with effective medium theories suggest that a

decrease in effective ϵ_r with increasing IDR concentration enhances polyampholytes LLPS in a cooperative manner because the formation of condensed phase lowers ϵ_r and that in turn induces stronger electrostatic attractions that favor the condensed phase.^{35,37}

In principle, LLPS of IDR chains in polarizable aqueous media can be directly simulated using explicit-water atomic models wherein partial charges are assigned to appropriate sites of the water and protein molecules; but such simulations are computationally extremely costly because a large number of IDR chains are needed to model LLPS. Here we use explicit-water atomic simulation involving only a few IDR molecules, not to model LLPS but to estimate how the effective ϵ_r depends on IDR concentration. We will then combine this information with analytical formulations to provide a more complete account of the electrostatic driving forces for LLPS. The dielectric properties of folded proteins,^{98,99} their solutions,¹⁰¹ and related biomolecular¹⁰² and cellular¹⁰³ settings have long been of interest.¹⁰⁴ For the current focus on biomolecular condensates, their interior dielectric environments are expected to be of functional significance, e.g., as drivers for various ions and charged molecules to preferentially partition into a condensate.¹⁰⁵

As outlined in Materials and Methods, GROMACS¹⁰⁶ and the amber99sb-ildn forcefield¹⁰⁷ are used for our explicit-water simulations using either the TIP3P¹⁰⁸ or the SPC/E¹⁰⁹ model of water in simulation boxes containing WT Ddx4 IDR chains. Relative permittivities are estimated by fluctuations of the system dipole moment.^{99,101} Simulations are also performed on artificially constructed Ddx4 (aDdx4) in which the sidechain charges of Arg, Lys, Asp, and Glu are neutralized for possible applications when sidechain charges are treated separately from that of the background dielectric medium. Methodological details are provided in SI Appendix, SI Text.

Some of the simulated ϵ_r values are plotted in Fig. 7a to illustrate their dependence on IDR volume fraction ϕ (the $\phi \propto$ concentration relation and an extended set of simulated ϵ_r s are provided by SI Appendix, SI Text, Fig. S6, and Table S1). The difference in simulated $\epsilon_r(\phi)$ for Ddx4 and aDdx4 is negligible except at very low IDR concentration (Fig. 7a and SI Appendix, Fig. S6), likely because the main contribution to the dielectric effect of IDR in the atomic model is from the partial charges on the protein backbone. Consistent with expectation,^{35,37} simulated $\epsilon_r(\phi)$ in Fig. 7a decreases with increasing ϕ for all solvent conditions considered. Permittivity is known to decrease with salt.^{113,114} Here this expected effect is observed for TIP3P solution of IDR at low but not at high IDR concentration. Interestingly, the $\epsilon_r(\phi)$ simulated with SPC/E water and 100 mM NaCl exhibits nonlinear decrease with increasing ϕ , which is akin to that predicted by the Bragg-Pippard¹¹² and Clausius-Mossotti models; but the TIP3P-simulated $\epsilon_r(\phi)$ appears to be linear in ϕ , which is more in line with the Maxwell Garnett and Bruggeman models.³⁷

We utilize the salient features of the coarse-grained KH chain model for Ddx4 (Fig. 4) and the IDR-concentration-dependent permittivities from explicit-water simulations (Fig. 7a) to inform an analytical theory for IDR LLPS, referred to as RPA+FH, that combines a random-phase-approximation (RPA) of charge-sequence-specific electrostatics and Flory-

Huggins (FH) mean-field treatment for the other interactions.^{34,35} An in-depth analysis of our previous RPA formulation for IDR-concentration-dependent ϵ_r (Ref. 35) indicates that only an $\epsilon_r(\phi)$ linear in ϕ can be consistently treated by RPA (SI Appendix, SI Text). In view of this recognition, and considering the uncertainties of simulated $\epsilon_r(\phi)$ for different water models (Fig. 7a), three alternative linear forms of $\epsilon_r(\phi)$ (straight lines in Fig. 7a) are used for the present RPA formulation to cover reasonable variations in $\epsilon_r(\phi)$.

The mean-field FH interaction parameters in our RPA+FH models for the four Ddx4 IDRs are obtained from the four sequences' average pairwise non-electrostatic KH contact energies. For each of the 236-residue sequences, we calculate the average of the $E_{ij}(r_0)$ [KH] quantity (Fig. 1a), for a given pair of residue types, over all pairs of residues on the sequence, including a residue with itself ($236 \times 237/2 = 27,966$ pairs total), except those pairs involving two charged residues (Arg-Arg, Arg-Lys, Arg-Asp, Arg-Glu, Lys-Lys, Lys-Asp, Lys-Glu, Asp-Asp, Asp-Glu, and Glu-Glu) because interactions of charged pairs are accounted for by RPA separately. The resulting average energies in units of kcal mol⁻¹, -0.1047 for WT and CS, -0.0689 for FtoA, and -0.0924 for RtoK, are then input with an overall multiplicative scaling factor into RPA+FH theories with ϕ -independent ϵ_r for three different fixed $\epsilon_r = 80, 40,$ and 20 . The computed RPA+FH phase diagrams are then fitted to the corresponding phase diagrams simulated by coarse-grained KH chain models in Fig. 4 to determine a single energy scaling factor from the best possible fit (SI Appendix, Fig. S7). The product of this factor and the sequence-dependent averages of $E_{ij}(r_0)$ [KH] defined above is now used as the enthalpic FH χ parameters in the final RPA+FH theories with IDR-concentration-dependent $\epsilon_r(\phi)$. Details of unit conversion between our explicit-chain simulation and our analytical RPA+FH formulation are in SI Appendix, SI Text.

In this connection, it is instructive to note that the corresponding averages of $E_{ij}(r_0)$ [HPS] for the HPS model are -0.1214 for WT and CS, -0.1179 for FtoA, and -0.1294 for RtoK. In this case, the more favorable (more negative) average energy of RtoK than WT underlies the mismatch of HPS prediction with experiment seen in Fig. 3b.

Figure 7b and c show the phase diagrams of the four Ddx4 IDRs predicted using RPA+FH theories with three alternative IDR-concentration-dependent $\epsilon_r(\phi)$ functions and KH-derived mean-field FH parameters as prescribed above. In all cases considered, the WT sequence (red curves) exhibit a higher propensity to LLPS than the three variants, indicating that this general agreement with the experimental trend seen in Fig. 4 holds up not only under the simplifying assumption of a constant ϵ_r but also when the dielectric effect of the IDRs is taken into account. As discussed in SI Appendix, SI Text, we have previously subtracted the self-energy term in the RPA formulation for numerical efficiency because the term has no impact on the predicted phase diagram when ϵ_r is a constant independent of ϕ because the self-energy contribution is identical for the dilute and condensed phases. However, with an IDR-concentration-dependent $\epsilon_r(\phi)$, as for the cases considered here, the self energy—with the short-distance cutoff of Coulomb interaction in the RPA formulation corresponding roughly to a finite Born radius¹¹⁵—is physically relevant as

it decreases with increasing ϵ_r , and therefore it affects the predicted LLPS properties as manifested by the difference between Fig. 7b and c. It follows that the self-energy term quantifies a tendency for an individual polyampholyte chain to prefer the dilute phase with a higher ϵ_r —because of its more favorable electrostatic interactions with the more polarizable environment—over the condensed phase with a lower ϵ_r . This tendency disfavors LLPS. At the same time, the lower ϵ_r in the condensed phase entails a stronger inter-chain attractive electrostatic force that drives the association of polyampholyte chains. Therefore, taken together, relative to the assumption of a constant ϵ_r , the overall impact of an IDR-concentration-dependent $\epsilon_r(\phi)$ is expected to be modest because it likely entails a partial tradeoff between these two opposing effects. This consideration is borne out in Fig. 7b and c. When self energy is neglected in Fig. 7c, LLPS propensities predicted using $\epsilon_r(\phi)$ s are relatively high (as characterized by the critical temperatures), comparable to those for a fixed $\epsilon_r = 40$ in Fig. 4b. When the physical effect of self energy is accounted for in Fig. 7b, LLPS propensities predicted using $\epsilon_r(\phi)$ s are significantly lower: overall they are comparable but slightly lower than those for a fixed $\epsilon_r = 80$ in Fig. 4a. Consistent with this physical picture, whereas the $\epsilon_r(\phi)$ with a sharper decrease with increasing ϕ leads to a higher LLPS propensity when self energy is neglected (dashed curves have higher critical temperatures than dashed-dotted curves of the same color in Fig. 7c), for the physically appropriate formulation with self energy, a sharper decrease in $\epsilon_r(\phi)$ with increasing ϕ leads to a lower LLPS propensity (dashed curves have lower critical temperatures than dashed-dotted curves of the same color in Fig. 7b).

CONCLUSION

In summary, we have gained new insights into the physical forces that drive the formation of biomolecular condensates by systematically evaluating coarse-grained, residue-based protein chain models embodying different outlooks as to the types of interactions that are important for LLPS of IDRs by comparing model predictions against experimental data on WT Ddx4 IDR and its three variants as well as WT LAF-1 RGG and its two variants, acquiring essential knowledge from agreement as well as disagreement between simulation and experiment. Aiming to account for all observed relative LLPS propensities of the sequences, we find that hydrophobicity, electrostatic, and cation- π interactions are insufficient by themselves. Rationalization of experiment on arginine-to-lysine variants entails significantly more favorable arginine-associated over lysine-associated contacts, an effect that is most likely underpinned by π - π interactions. This perspective is in line with bioinformatics analysis of LLPS propensities⁶⁸ and recent experiments on other IDRs.^{39,60} In this regard, it is reassuring that the balance of forces for LLPS of IDRs appears to be partly captured by common PDB-derived statistical potentials developed to study protein folding and binding. However, we found that the condensate-stabilizing contributions of phenylalanine interactions are significantly weaker than that estimated from statistical potentials, most likely because such

interactions exist in a highly solvent accessible environments rather than in the sequestered cores or binding interfaces of globular proteins. We have also highlighted the reduced electric permittivity inside condensed IDR phases. Although this effect’s overall influence on LLPS propensity may be modest because of a tradeoff between its consequences on IDR self energies and on inter-IDR interactions, the effect of IDR-concentration-dependent permittivity by itself should be of functional importance in biology because of its potential impact on biochemical reactions and preferential partition of certain molecules into a given biomolecular condensate. All told, the present study serves not only to clarify the aforementioned issues of general principles, it also represents a useful step toward a transferable coarse-grained model for sequence-specific biomolecular LLPS. Many questions remain to be further investigated nonetheless. These include—and are not limited to—an adequate description of solvent-exposed interactions involving large hydrophobic/aromatic residues such as phenylalanine, a proper balance between attractive and repulsive interactions,⁵³ devising temperature-dependent effective interactions,⁵⁰ an accurate account of small ion effects,^{41,116,117} and incorporation of nucleic acids into LLPS simulations.⁴³ Progress in these directions will deepen our understanding of fundamental molecular biological processes and will advance the design of novel IDR-like materials as well.

Materials and Methods

Our implicit-water coarse-grained explicit-chain modeling setup used in the first part of the present investigation for multiple IDP molecules follows largely the Langevin dynamics formulations in Refs. 52, 53 for IDP LLPS. The simulation protocol features an initial slab-like condensed configuration that allows for efficient equilibration to produce simulated LLPS data⁷⁸. As discussed, model energy functions embodying different physical perspectives are considered. The subsequent explicit-water simulations for estimating IDR-concentration-dependent relative permittivity are conducted on five WT Ddx4 IDRs using GROMACS¹⁰⁶ in conjunction with the amber99sb-ildn forcefield¹⁰⁷ and with TIP3P¹⁰⁸ or SPC/E¹⁰⁹ waters. Details of our methodology and the development of analytical RPA formulation are provided in SI Appendix, SI Text.

Acknowledgments

We thank Robert Best, Alex Holehouse, Jeetain Mittal, Rohit Pappu, and Wenwei Zheng for helpful discussions. This work was supported by Canadian Institutes of Health Research grants MOP-84281 and NJT-155930 to H.S.C., Natural Sciences and Engineering Research Council of Canada Discovery grants RGPIN-2016-06718 to J.D.F.-K. and RGPIN-2018-04351 to H.S.C., and computational resources provided generously by Compute/Calcul Canada.

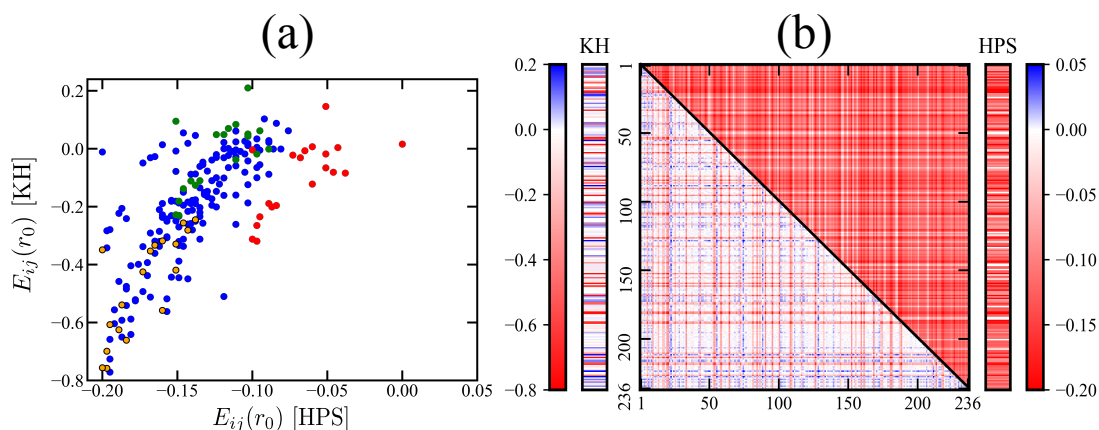


Fig. 1. Comparing two amino acid residue-based coarse-grained potentials. (a) Scatter plot of 210 pairwise contact energies (in units of kcal mol^{-1}) in the HPS (horizontal variable) versus those in the KH (vertical variable) model.⁵² $E_{ij}(r_0)$ s are the pairwise potential energies $U_{\text{aa|HPS}}(r)$ or $U_{\text{aa|KH}}(r)$ (SI Appendix, SI Text), between two residues of types i, j separated by $r_{ij} = r_0$ where the Lennard-Jones component of the potential is minimum (i, j here stand for labels for the 20 amino acid types). Energies of contacts involving Arg (red circles), Lys (green circles) and Phe (yellow-filled black circles) are colored differently from others (blue circles). (b) Contact energies between residue pairs at positions i, j of the $n = 236$ sequence of WT Ddx4 IDR (Ddx4^{N1}, Ref. 4) in the two potentials are color coded by the scales. The vertical and horizontal axes represent residue positions $i, j \leq n$. The $i \neq j$ contact energies in the HPS and KH models are provided in the two-dimensional plot, whereas the $i = j$ contact energies are shown alongside the model potentials' respective color scales.

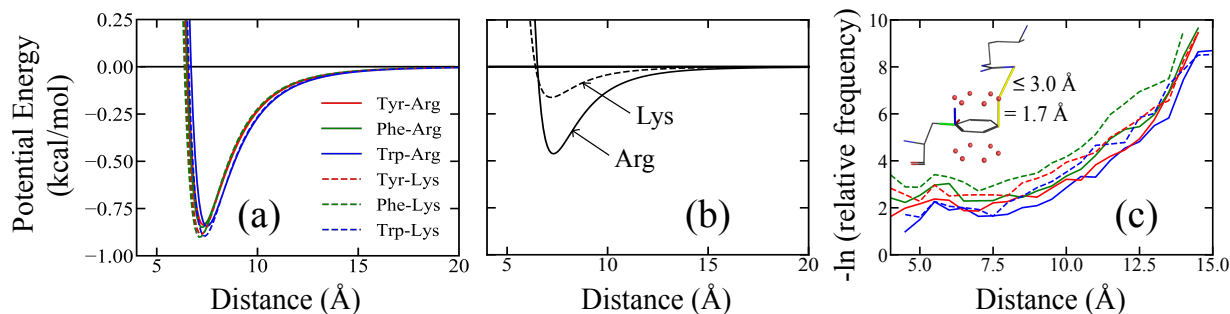


Fig. 2. Possible cation- π interaction potentials. (a) Sum of the coarse-grained HPS potential and a model cation- π interaction with a uniform $(\epsilon_{c\pi})_{ij} = 3.0 \text{ kcal mol}^{-1}$ as a function of residue-residue distance for the residue pairs Arg-Tyr, Arg-Phe, Arg-Trp, Lys-Tyr, Lys-Phe and Lys-Trp, wherein Tyr/Phe/Trp are labeled as red/green/blue and Arg/Lys are represented by solid/dashed curves. (b) An alternate cation- π potential in which Arg-Tyr/Phe/Trp is significantly more favorable (solid curve, $(\epsilon_{c\pi})_{ij} = 1.85 \text{ kcal mol}^{-1}$) than Lys-Tyr/Phe/Trp (dashed curve, $(\epsilon_{c\pi})_{ij} = 0.65 \text{ kcal mol}^{-1}$). Note that the plotted curves here—unlike those in (a)—do not contain the HPS potential. (c) Normalized C_{α} - C_{α} distance-dependent contact frequencies for the aforementioned six cation- π pairs (color coded as in (a)) computed using a set of 6,943 high-resolution X-ray protein crystal structures (resolution $\leq 1.8 \text{ \AA}$) from a published non-redundant set.⁶⁸ Contact pair statistics are collected from residues on different chains in a given structure and residues separated by ≥ 50 amino acids along the same chain. C_{α} - C_{α} distances are divided into 0.2 \AA bins. For each bin, the relative frequency is the number of instances of a cation- π -like contact (defined below) divided by the total number of residue pairs with C_{α} - C_{α} distances within the narrow range of the bin. Thus, the shown curves quantify the tendency for a given pair of residues to engage in cation- π interaction provided that the pair is spatially separated by a given C_{α} - C_{α} distance. Here a cation- π -like contact is recognized if either a Lys NZ or an Arg NH1 nitrogen atom is within 3.0 \AA of any one of the points 1.7 \AA above or below a sp^2 carbon atom along the normal of the aromatic ring in a Tyr, Phe, or Trp residue. This criterion is exemplified by the molecular drawing (inset) of a contact between an Arg (top) and a Phe (bottom). Colors of the chemical bonds indicate types of atom involved, with carbon in black, oxygen in red, and nitrogen in blue. The red dots here are points on the exterior surfaces of the electronic orbitals farthest from the sp^2 carbons in the aromatic ring. The blue, green, and red lines emanating from a corner of the aromatic ring constitute a local coordinate frame, with the blue line being the normal vector of the plane of the aromatic ring determined from the positions of its first three atoms. The yellow lines mark spatial separations used to define the cation- π -like contact.

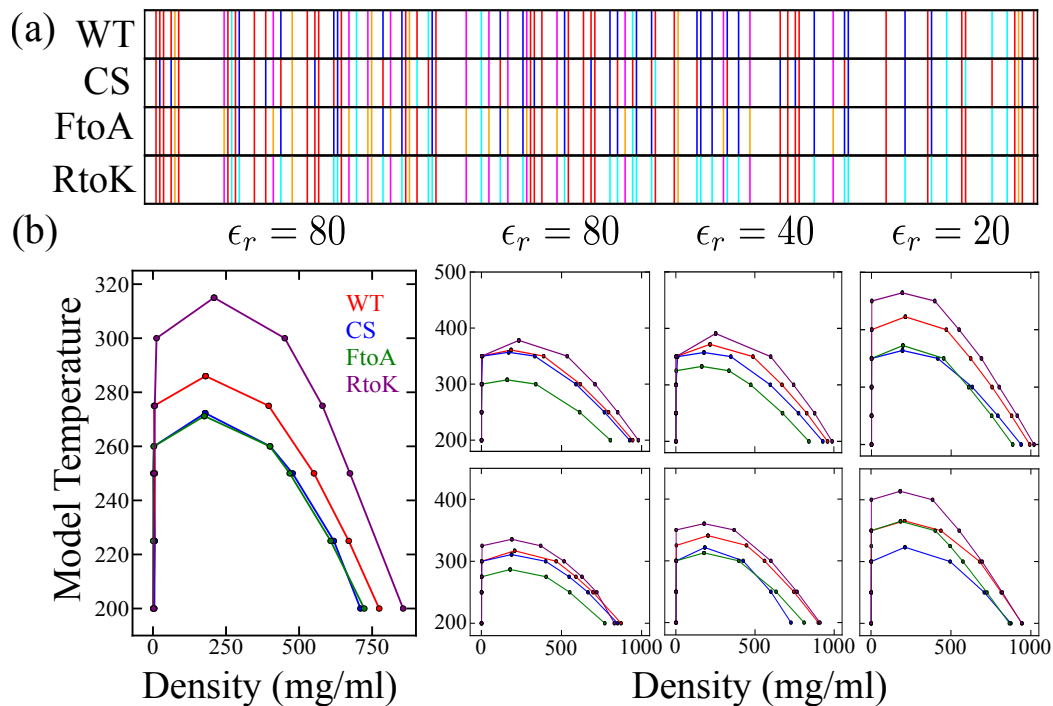


Fig. 3. Simulated phase behaviors of Ddx4 IDR variants in a hydrophobicity-dominant potential augmented by cation- π interactions. (a) Sequence patterns of the wildtype (WT) and its charge-scrambled (CS), Phe to Ala (FtoA) and Arg to Lys (RtoK) variants. Select residue types are highlighted: Ala (orange), Asp and Glu (red), Phe (magenta), Lys (cyan), and Arg (dark blue); other residue types are not distinguished. (b) Simulated phase diagrams of WT, CS, FtoA and RtoK Ddx4 IDR at various relative permittivities (ϵ_r) as indicated, using the HPS model only (leftmost panel) and the HPS model augmented with cation- π interactions (other panels on the right) with either a uniform $(\epsilon_{c\pi})_{ij}$ as described in Fig. 2a (top) or with different $(\epsilon_{c\pi})_{ij}$ values for Arg and Lys as given in Fig. 2b (bottom).

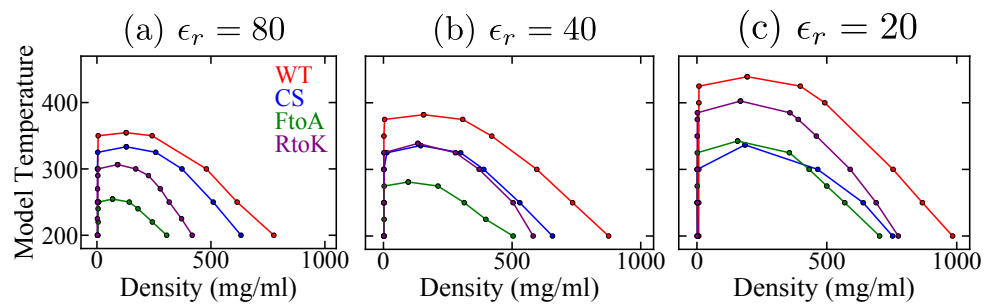


Fig. 4. Simulated phase behaviors of Ddx4 IDR variants using an interaction scheme based largely on PDB-derived statistical potentials. Phase diagrams were computed using the KH model at three different relative permittivities (ϵ_r).

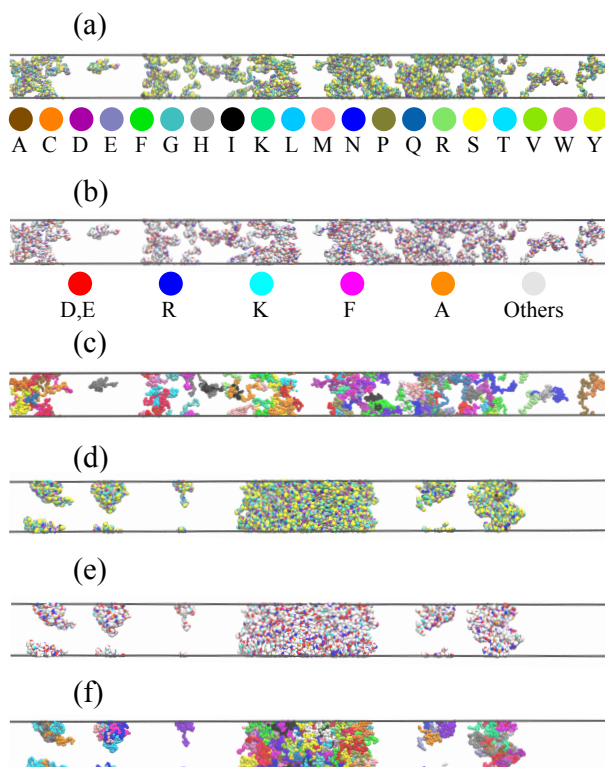


Fig. 5. Illustrative snapshots of $Ddx4^{N1}CS$ phase behaviors simulated using the KH potential for $\epsilon_r = 40$. (a) A non-phase-separated snapshot at model temperature 375 K, wherein the amino acid residues are colored using the default VMD scheme^{110,111} as provided by the key below the snapshot. (b) Same as (a) except the color scheme (as shown) is essentially identical to that in Fig. 3a. (c) Same as (a) and (b) except all residues along the same chain share the same color. Neighboring chains are colored differently to highlight the diversity of conformations in the system. (d–f) A phase-separated snapshot at model temperature 325 K. The color schemes are the same, respectively, as those in (a–c).

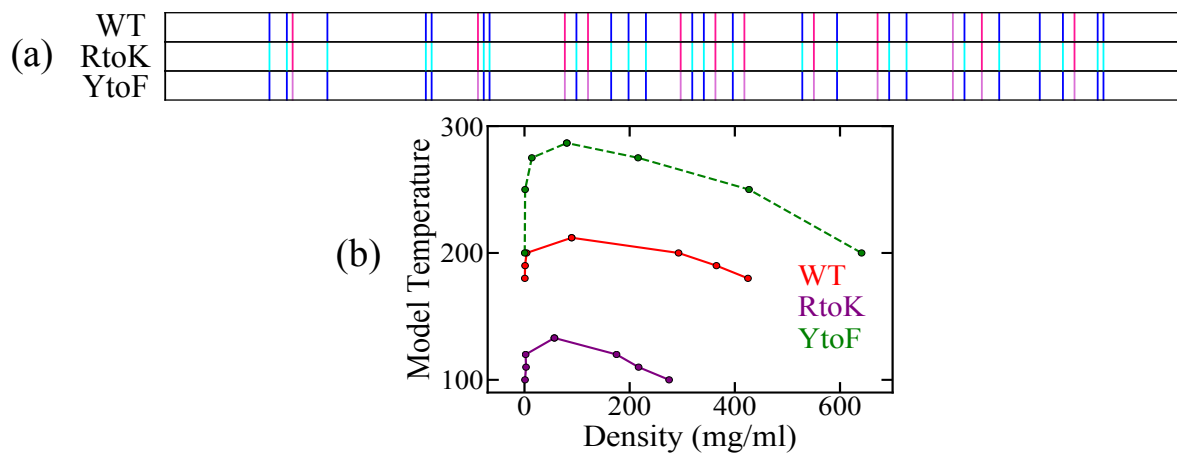


Fig. 6. Simulated phase diagrams of LAF-1 IDRs computed by the KH model at $\epsilon_r = 40$ for the three sequences in SI Appendix, Fig. S5. (a) Sequence patterns of the WT and two variants. Highlighted residues are Phe (magenta), Lys (cyan), Arg (dark blue), as in Fig. 3a, and Tyr (pink); other residue types, including Ala, Asp, and Glu which were highlighted in Fig. 3a, are not distinguished here. (b) Phase diagrams for WT and mutant sequences are plotted in different colors as indicated.

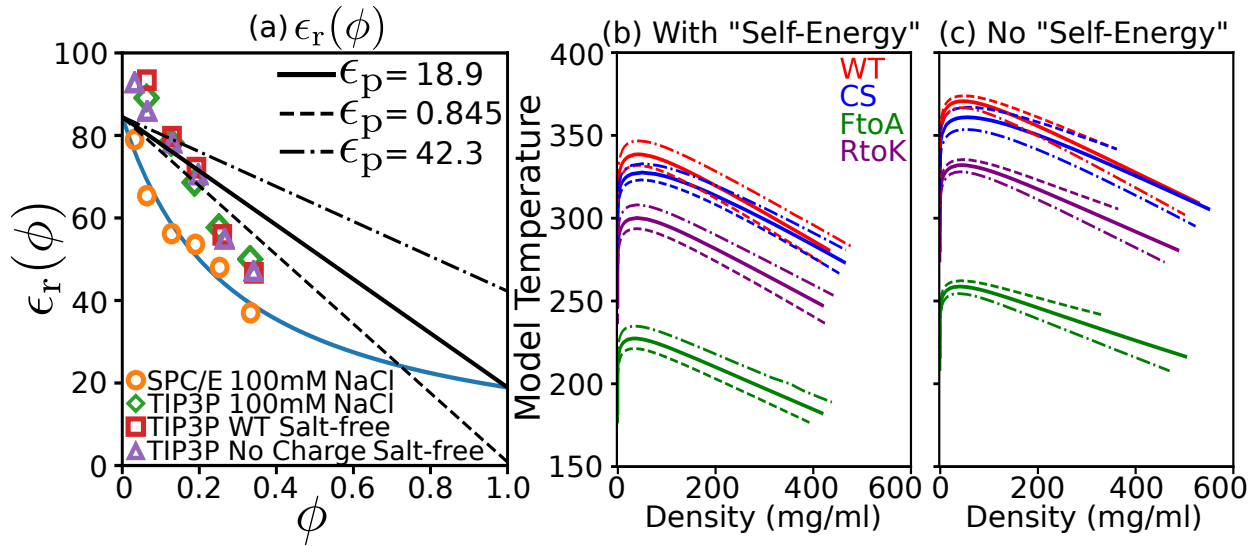


Fig. 7. Effects of IDR-concentration-dependent relative permittivity on phase behaviors. (a) Relative permittivity $\epsilon_r(\phi)$ values obtained by atomic simulations (symbols) using various explicit-water models (as indicated, bottom) are shown as functions of Ddx4 volume fraction ϕ ($\phi = 1$ corresponds to pure Ddx4). The blue curve is a theoretical fit of the SPC/E, [NaCl] = 100 mM explicit-water simulated data based on the Slab (Bragg and Pippard¹¹²) model [Eq. (34) of Ref. 37], viz., $1/\epsilon_r(\phi) = \phi/\epsilon_p + (1 - \phi)/\epsilon_w$ with the fitted $\epsilon_p = 18.9$ and $\epsilon_w = 84.5$ where ϵ_p and ϵ_w are, respectively, the relative permittivity of pure protein and pure water. The black solid, dashed, and dashed-dotted lines are approximate linear models of $\epsilon_r(\phi) = \epsilon_p\phi + \epsilon_w(1 - \phi)$ with the same ϵ_w but different ϵ_p values as indicated (top-right), resulting in $d\epsilon_r(\phi)/d\phi$ slopes, respectively, of -65.6 , -83.9 , and -42.2 . (b, c) Theoretical phase diagrams of the four Ddx4 IDR variants were obtained by a RPA theory that incorporates an $\epsilon_r(\phi)$ linear in ϕ . Solid, dashed, and dashed-dotted curves correspond, as in (a), to the three different ϵ_p values used in the theory. The electrostatic contribution to the phase behaviors is calculated here using either (b) the expression for f_{el} given by Eq. (S51) in SI Appendix SI Text [i.e., Eq. (68) of Ref. 35 with its self-interaction term $\mathcal{G}_2(\vec{k})$ excluded] or (c) the full expression for f_{el} [Eq. (68) in the same reference, or equivalently Eq. (S2) in SI Appendix, SI Text]. Further details are provided in SI Appendix, SI Text.

Supplementary Information

(SI Appendix)

for

Comparative Roles of Charge, π and Hydrophobic Interactions in Sequence-Dependent Phase Separation of Intrinsically Disordered Proteins

Suman DAS,^a Yi-Hsuan LIN,^{a,b} Robert M. VERNON,^b Julie D. FORMAN-KAY^{b,a}
and Hue Sun CHAN^{a,1}

^aDepartment of Biochemistry, University of Toronto, Toronto, Ontario M5S 1A8, Canada;

^bMolecular Medicine, Hospital for Sick Children, Toronto, Ontario M5G 0A4, Canada

¹Corresponding author

E-mail: chan@arrhenius.med.utoronto.ca; Tel: (416)978-2697; Fax: (416)978-8548

Department of Biochemistry, University of Toronto, Medical Sciences Building – 5th Fl.,
1 King's College Circle, Toronto, Ontario M5S 1A8, Canada.

Contents

SI Text	25
Models and Methods	25
RPA Theory	31
SI Figures	47
Figure S1	47
Figure S2	48
Figure S3	49
Figure S4	50
Figure S5	51
Figure S6	52
Figure S7	53
SI Table	54
Table S1	54
Combined Main-Text and SI References	55

SI Text

Models and Methods

COARSE-GRAINED CHAIN MODELS

The coarse-grained protein chain models in the present study basically follow those in Refs. 52, 53, but with modified and additional features. In accordance with our previous notation for explicit-chain simulation studies,^{47,53} let $\mu, \nu = 1, 2, \dots, n$ be the labels for the n IDP chains in the system, and $i, j = 1, 2, \dots, N$ be the labels of the N residues in each IDP chain. The total potential energy U_T is a function of the residue positions, denoted here as $\{\mathbf{R}_{\mu i}\}$. Writing

$$U_T = U_{\text{bond}} + U_{\text{el}} + U_{\text{aa}} , \quad (\text{S1})$$

where U_{bond} is the bond-length term for chain connectivity:

$$U_{\text{bond}} = \frac{K_{\text{bond}}}{2} \sum_{\mu=1}^n \sum_{i=1}^{N-1} (r_{\mu i, \mu i+1} - l)^2 \quad (\text{S2})$$

with $r_{\mu i, \nu j} \equiv |\mathbf{R}_{\mu i} - \mathbf{R}_{\nu j}|$, $l = 3.8 \text{ \AA}$ is the $\text{C}_\alpha\text{-C}_\alpha$ virtual bond length [l is equivalent to a in Eq. (3) of Ref. 53], $K_{\text{bond}} = 10 \text{ kJ mol}^{-1} \text{ \AA}^{-2}$ [this value would be identical to that used in Ref. 52 if the 10 kJ/\AA^2 value quoted above Eq. (1) in this reference is a typographical error, i.e., it misses a “/mol”; by comparison, the much stiffer K_{bond} value used in Eq. (3) in Ref. 53, which follows Ref. 78 with the aim of comparing with fixed-bond-length Monte Carlo simulations, is equivalent to $23.7 \text{ MJ mol}^{-1} \text{ \AA}^{-2}$], and U_{el} is the electrostatic interaction:

$$U_{\text{el}} = \sum_{\mu, \nu=1}^n \sum_{\substack{i, j=1 \\ (\mu, i) \neq (\nu, j)}}^N \frac{\sigma_{\mu i} \sigma_{\nu j} e^2}{4\pi \epsilon_0 \epsilon_r r_{\mu i, \nu j}} \exp\left(-\kappa r_{\mu i, \nu j}\right) , \quad (\text{S3})$$

wherein $\sigma_{\mu i}$ is the charge of the i th residue in units of elementary electronic charge e , ($\sigma_{\mu i}$ is independent of μ), ϵ_0 is vacuum permittivity, ϵ_r is relative permittivity (dielectric constant), and κ is the reciprocal of the Debye screening length, which is taken to be 10.0 \AA in this study ($\kappa = 0.1 \text{ \AA}^{-1}$). Following Table S1 of Ref. 52, σ values for Arg and Lys are assigned to be +1, those of Asp and Glu are -1 , and that of His is $+0.5$. All other residues are taken to be neutral, i.e., with $\sigma = 0$.

The U_{aa} in Eq. (S1) is the sum of pairwise interaction energies among the residues, viz.,

$$U_{\text{aa}} = \sum_{\mu, \nu=1}^n \sum_{\substack{i, j=1 \\ (\mu, i) \neq (\nu, j)}}^N (U_{\text{aa}})_{\mu i, \nu j} , \quad (\text{S4})$$

where $(U_{\text{aa}})_{\mu i, \nu j}$ is the interaction between the i th residue of the μ th chain with the j th residue of the ν th chain. We investigate several physically plausible U_{aa} functions, as follows:

The HPS model

The hydrophobicity scale (HPS) model is identical to the one introduced by Dignon et al.⁵² based on an atomic-level hydrophobicity scale devised by Kapcha and Rossky.⁷⁶ The interaction between amino-acid pairs in this model is given by

$$(U_{\text{aa}})_{\mu i, \nu j} = (U_{\text{aa|HPS}})_{\mu i, \nu j} \equiv \begin{cases} (U_{\text{LJ}})_{\mu i, \nu j} + (1 - \lambda_{ij}^{\text{HPS}})\epsilon, & \text{if } r \leq 2^{1/6}a_{ij} \\ \lambda_{ij}^{\text{HPS}}(U_{\text{LJ}})_{\mu i, \nu j} & \text{otherwise} \end{cases} \quad (\text{S5})$$

where $\lambda_{ij}^{\text{HPS}} \equiv (\lambda_i + \lambda_j)/2$, $a_{ij} \equiv (a_i + a_j)/2$, with λ_i and a_i being the hydrophobicity and diameter, respectively, of the model amino acid residue at sequence position i , as given, respectively, by the λ and σ values in Table S1 of Ref. 52; $(U_{\text{LJ}})_{\mu i, \nu j}$ is the Lennard-Jones (LJ) potential,

$$(U_{\text{LJ}})_{\mu i, \nu j} = 4\epsilon_{ij} \left[\left(\frac{a_{ij}}{r_{\mu i, \nu j}} \right)^{12} - \left(\frac{a_{ij}}{r_{\mu i, \nu j}} \right)^6 \right], \quad (\text{S6})$$

where the LJ well depth ϵ_{ij} (not to be confused with the permittivities) is set to be $\epsilon_{ij} = 0.2$ kcal mol⁻¹ irrespective of i, j for the HPS model, as in Ref. 52.

The HPS+cation- π models

In view of the importance of cation- π interactions in protein structure (see discussion in the main text), we consider also a class of model potentials, $U_{\text{aa|HPS+c}\pi}$ s, that augment the HPS potential with cation- π terms for Arg-Phe, Arg-Trp, Arg-Tyr, Lys-Phe, Lys-Trp, and Lys-Tyr residue pairs. In these interaction schemes,

$$(U_{\text{aa}})_{\mu i, \nu j} = (U_{\text{aa|HPS+c}\pi})_{\mu i, \nu j} \equiv (U_{\text{aa|HPS}})_{\mu i, \nu j} + (U_{\text{aa|c}\pi})_{\mu i, \nu j}, \quad (\text{S7})$$

where

$$(U_{\text{aa|c}\pi})_{\mu i, \nu j} = (\epsilon_{c\pi})_{ij} \left[\left(\frac{a_{ij}}{r_{\mu i, \nu j}} \right)^{12} - \left(\frac{a_{ij}}{r_{\mu i, \nu j}} \right)^6 \right], \quad (\text{S8})$$

and $(\epsilon_{c\pi})_{ij}$ is the cation- π interaction strength, $(\epsilon_{c\pi})_{ij} > 0$ only if residue pair $\mu i, \nu j$ is one of the aforementioned six cation- π pairs, otherwise $(\epsilon_{c\pi})_{ij} = 0$. This simple form is adopted from the cation- π term in Eq. (S1) of Ref. 72.

Two sets of $(\epsilon_{c\pi})_{ij}$ values are analyzed in the present study:

(i) $(\epsilon_{c\pi})_{ij} = 3.0$ kcal mol⁻¹ for all six cation- π pairs. The rationale for using a single $(\epsilon_{c\pi})_{ij}$ value is the suggestion by statistical and other inferences that the variations of

interaction strengths among the six cation- π amino acid residue pairs could be relatively small,^{69,72} though subsequently we will also explore scenarios in which significant variations in cation- π interaction strengths exist among the pairs. When combined with the $(U_{\text{aa|HPS}})_{\mu i, \nu j}$ contribution in Eq. (S7), $(\epsilon_{c\pi})_{ij} = 3.0 \text{ kcal mol}^{-1}$ leads to well depths for $(U_{\text{aa}})_{\mu i, \nu j} = (U_{\text{aa|HPS+c}\pi})_{\mu i, \nu j}$ of $\approx 0.85 \text{ kcal mol}^{-1}$ for Arg-Phe, Arg-Trp, Arg-Tyr, and corresponding well depths of $\approx 0.90 \text{ kcal mol}^{-1}$ for Lys-Phe, Lys-Trp, and Lys-Tyr (see Fig. 2a of the main text). It should be noted here that we have chosen an $(\epsilon_{c\pi})_{ij}$ value significantly smaller than those used in Ref. 72 in order for the model cation- π interactions to be more compatible with the shallow well depths of the $(U_{\text{aa|HPS}})_{\mu i, \nu j}$ potentials in the HPS model, which has a maximum well depth of $0.2 \text{ kcal mol}^{-1}$. Nonetheless, the $(\epsilon_{c\pi})_{ij} = 3.0 \text{ kcal mol}^{-1}$ value still entails a cation- π interaction strength which is about double that of electrostatic interaction when ϵ_r in Eq. (S3) corresponds to that of bulk water ($\epsilon_r \approx 80$). This ratio between the strengths of cation- π and electrostatic interactions in an aqueous environment conforms to a similar ratio deduced computationally.⁷⁰

(ii) Different $(\epsilon_{c\pi})_{ij}$ values for cation- π pairs involving Arg and pairs involving Lys, with $(\epsilon_{c\pi})_{ij} = 1.85 \text{ kcal mol}^{-1}$ for Arg-Phe, Arg-Trp, Arg-Tyr and $(\epsilon_{c\pi})_{ij} = 0.65 \text{ kcal mol}^{-1}$ for Lys-Phe, Lys-Trp, and Lys-Tyr. This alternate model cation- π interaction scheme is motivated by observed trends of statistical potentials derived from PDB protein structures such as the Miyazawa-Jernigan energies^{74,75} used in the KH/MJ model⁵² (described below) and the new analysis presented in the main text as well as recent experimental evidence,^{39,68} all of which suggest that cation- π interactions involving Arg is more favorable than those involving Lys. The $(\epsilon_{c\pi})_{ij}$ values in this scheme are chosen such that the combined well depth of $(U_{\text{aa|HPS+c}\pi})_{\mu i, \nu j}$ for cation-aromatic pairs are comparable to the deepest well depth of $\approx 0.5 \text{ kcal mol}^{-1}$ in the KH/MJ model. In particular, $(\epsilon_{c\pi})_{ij} = 1.85 \text{ kcal mol}^{-1}$ leads to a combined well depth of $\approx 0.55 \text{ kcal mol}^{-1}$ for terms in $(U_{\text{aa|HPS+c}\pi})_{\mu i, \nu j}$ involving Arg-aromatic pairs, whereas $(\epsilon_{c\pi})_{ij} = 0.65 \text{ kcal mol}^{-1}$ leads to a corresponding combined well depth of $\approx 0.3 \text{ kcal mol}^{-1}$ for Lys-aromatic pairs (Fig. 2b of the main text).

The KH (KH/MJ) model

The Kim-Hummer/Miyazawa-Jernigan (KH/MJ) model corresponds to the KH-D model used by Dignon et al.,⁵² and is based on the statistical potentials of Miyazawa and Jernigan (MJ).⁷⁵ Following Ref. 52, we refer to this model as KH in the main text and hereafter. The basic functional form of the KH potential, $U_{\text{aa|KH}}$, is similar to that for the HPS potential in Eq. (S5). For the KH model,

$$(U_{\text{aa}})_{\mu i, \nu j} = (U_{\text{aa|KH}})_{\mu i, \nu j} \equiv \begin{cases} (U_{\text{LJ}})_{\mu i, \nu j} + (1 - \lambda_{ij}^{\text{KH}})\epsilon, & \text{if } r \leq 2^{1/6}a_{ij} \\ \lambda_{ij}^{\text{KH}}(U_{\text{LJ}})_{\mu i, \nu j} & \text{otherwise} \end{cases} \quad (\text{S9})$$

where $(U_{\text{LJ}})_{\mu i, \nu j}$ is given by Eq. (S6), but now ϵ_{ij} depends on i, j . Specifically, for the KH

model

$$\epsilon_{ij} = |\alpha(e_{\text{MJ},ij} - e_0)|, \quad (\text{S10})$$

where $e_{\text{MJ},ij}$ is the MJ statistical potential between the residue type at position i and the residue type at position j , e_0 is a constant shift of the energies, and

$$\lambda_{ij}^{\text{KH}} = \begin{cases} 1 & \text{if } e_{\text{MJ},ij} \leq e_0 \\ -1 & \text{otherwise} \end{cases}. \quad (\text{S11})$$

We use $\alpha = 0.228$ and $e_0 = -1.0 \text{ kcal mol}^{-1}$ in the present study. The resulting pairwise energies e_{MJ} correspond to the KH-D parameter set for IDRs in Table S3 of Ref. 52.

Simulation method

Molecular (Langevin) dynamics simulations are carried out using the protocol outlined in the ‘‘Simulation framework’’ section of Ref. 52, with parameters modified for the present applications. For each simulation, we consider 100 copies of one of the four Ddx4 IDR sequences (Fig. S1) or the three LAF-1 IDR sequences (Fig. S5), governed by one of the above coarse-grained model potential functions. At the initial step, all the IDR chains are randomly placed in a relatively large, $300 \times 300 \times 300 \text{ \AA}^3$ simulation box. Energy minimization is then applied to minimize unfavorable steric clashes among the amino acid residues. Equilibrating *NPT* simulation is then performed for 50 ns at a temperature of 100 K and pressure of 1 bar, maintained by Martyna-Tobias-Klein (MTK) thermostat and barostat^{118,119} with a coupling constant of 1 ps. It should be noted that the simulation pressure does not correspond to physical pressure because solvent (water) pressure is not accounted for in the present coarse-grained, implicit-solvent model setup. In this regard, pressure is used entirely as an efficient computational device for achieving condensed configurations as starting point of subsequent simulations. Throughout the dynamics simulation, equations of motion are integrated with a timestep of 10 fs and periodic boundary conditions are applied to all three spatial dimensions. After the initial *NPT* step, the simulation box is compressed again for 50 ns along all three spatial dimensions at 100 K as successive *NVT* ensembles (P changes during the process) using Langevin thermostat with friction coefficient 1 ps^{-1} . The extent of compression varies for different systems. Then the dimension along one of the three Cartesian axes of the simulation box is expanded 20 times relative to its initial value for a period of 50 ns while maintaining the temperature at 100 K. Equilibration *NVT* simulation is then performed at the chosen temperature for $2 \mu\text{s}$. Finally, production *NVT* runs are carried out for $4 \mu\text{s}$ and the chain configurations are saved every 0.5 ns for subsequent analysis. During the production run, the friction coefficient of the Langevin thermostat is decreased to 0.01 ps^{-1} for sampling efficiency. All simulations are performed by the HOOMD-blue software package.^{120,121} After the snapshots of simulated chain configurations are collected, the procedure for constructing phase diagrams from the configurations follows that described

in the ‘‘Simulation framework’’ section of Ref. 52 and the ‘‘Results and discussion’’ section of Ref. 53.

EXPLICIT-WATER SIMULATION OF IDR-CONCENTRATION-DEPENDENT PERMITTIVITY

Computational procedure

We estimate the IDR-concentration-dependent relative permittivity^{35,37} by atomistic explicit-water molecular dynamic simulations performed at six Ddx4 IDR (wildtype, WT) concentrations using GROMACS, version 2016.5.¹⁰⁶ The simulation proceeds as follows. Initially, a fully extended configuration of a Ddx4 IDR is prepared by PYMOL,¹²² to be used as input for Packmol¹²³ to place five Ddx4 IDRs at random locations in a cubic simulation box. The size of the box is varied to achieve different Ddx4 IDR concentrations. The Ddx4 IDRs are solvated by explicit water models in the simulation box. Each of the systems so constructed is then charge neutralized by adding appropriate number of Na⁺ ions. This is followed by energy minimization by steepest descent to minimize steric clashes. Hydrogen bonds are constrained with the LINCS algorithm.¹²⁴ Equation of motion is integrated using a time step of 2 fs with the leap-frog integrator¹²⁵ and cubic periodic boundary conditions. Long spatial-range electrostatic interaction is treated with particle mesh Ewald (PME) method¹²⁶ with a grid spacing of 0.16 nm and an interpolation order of 4. A cut-off of 1 nm is used for short-range van der Waals and electrostatic interactions. Initial equilibration is carried out for 2 ns under *NVT* conditions at 300 K. Temperature is maintained by Velocity-rescale thermostat¹²⁷ with a time constant of 0.1 ps for all simulations. This is followed by equilibration for 2 ns at 300 K under *NPT* conditions under 1 atm pressure, which is maintained by a Berendsen barostat¹²⁸ with a coupling constant of 2 ps. Since the Berendsen barostat does not always yield an *NPT* ensemble with high accuracy, the resulting system is equilibrated again for 1 ns as an *NPT* ensemble using the Parrinello-Rahman barostat^{129,130} with the same coupling constant, after which the production *NPT* run is carried out for 20 ns using the same Parrinello-Rahman barostat. Configurations are saved every 1.0 ps during the production run for subsequent analysis. In addition to simulations of Ddx4 IDR in essentially pure water (except a few Na⁺ ions), we also conduct simulations with Na⁺ and Cl⁻ ions at [NaCl] = 100 mM.

In order to enable a potentially more direct comparison with analytical theory that does not include the charges of amino acid residues in the estimation of effective permittivity of the aqueous medium,^{35,37} we carry out another set of simulations with Ddx4 IDR concentrations similar to the ones for which the above protocol is applied but with the charges of the sidechains of the charged amino acids Arg, Lys, Asp, and Glu artificially turned off. This set of simulation data is referred to as artificial Ddx4 or aDdx4. The same aforementioned procedure for equilibration and production is applied for this set of

simulations. The amber99sb-ildn force field¹⁰⁷ and the TIP3P water model¹⁰⁸ are used for both sets of simulations. To assess the robustness of the computed ϵ_r values, all simulations are also repeated using the SPC/E water model.¹⁰⁹

Relative permittivity analysis

Static relative permittivity ϵ_r (dielectric constant) is determined by the fluctuation of the total dipole moment vector, \mathbf{M}_T , of the system via the relation⁹⁹

$$\epsilon_r = \frac{\langle M_T^2 \rangle - \langle M_T \rangle^2}{3V\epsilon_0 k_B T} + 1, \quad (\text{S12})$$

where $M_T \equiv (\mathbf{M}_T \cdot \mathbf{M}_T)^{1/2}$ is the magnitude of the system dipole moment, $\langle \dots \rangle$ denotes averaging over system configurations under equilibrium conditions, and V is the volume of the simulation box. This relation, Eq. (S12), has been used to compute the static dielectric constant of several biological systems.^{99,101,131} Following the formulation in Ref. 101, \mathbf{M}_T is obtained as sum of dipole moments of individual water molecules and individual Ddx4 IDR chain molecules. Irrespective of the net charge of the molecule (water has net charge 0 whereas Ddx4 IDR has net charge $\approx -4e$), the dipole moment, \mathbf{m} , of a molecule comprising of N_m atoms with masses m_s ($s = 1, 2, \dots, N_m$) at positions \mathbf{r}_s with point charges q_s is given by $\mathbf{m} = \sum_s^{N_m} q_s (\mathbf{r}_s - \mathbf{r}_{\text{cm}})$, where $\mathbf{r}_{\text{cm}} \equiv \sum_s^{N_m} m_s \mathbf{r}_s / \sum_s^{N_m} m_s$ is the center-of-mass position of the molecule. Accordingly, atomic ions, Na^+ s and Cl^- s in our case, have zero dipole moment in this formulation. Once the dipole moments of the water and Ddx4 molecules are determined in this manner, they are combined to yield \mathbf{M}_T which in turn provides the system relative permittivity through Eq. (S12). Our computed ϵ_r for various concentrations of Ddx4 IDR at different salt concentrations using both the TIP3P and SPC/E water models are given in Table S1.

Random-Phase-Approximation (RPA) Theory of Phase Separation with IDR-Concentration-Dependent Permittivity

BACKGROUND

Our group has previously considered, within our RPA theory of liquid-liquid phase separation (LLPS), the effects of relative permittivity ϵ_r being dependent upon local protein concentration;^{35,37} i.e., $\epsilon_r = \epsilon_r(\phi_m)$ where ϕ_m is polymer (IDR) volume fraction. An $\epsilon_r(\phi_m)$ necessitates changes to our earlier RPA expressions for electrostatic interaction for a constant, position-independent ϵ_r , viz. [Eq. (33) of Ref. 35],

$$f_{\text{el}} = \frac{1}{2} \int \frac{d^3(ka)^3}{(2\pi)^3} \left\{ \ln[\det(1 + \hat{G}_k \hat{U}_k)] - \text{Tr}(\hat{\rho} \hat{U}_k) \right\}. \quad (\text{S13})$$

Here, as in Ref. 35, a^3 is unit volume, \hat{G}_k is the position correlation matrix, $\hat{\rho}$ is the density operator that provides the densities of various molecular species in the system (accounting for matter, not electric charge), and \hat{U}_k accounts for sequence-dependent Coulomb interactions [the expression for \hat{U}_k is provided by Eq. (35) of Ref. 35]. For the simple illustrative case here, which is a system of only IDR polymers without salt or counterions, \hat{G}_k reduces to the monomer-monomer correlation (\hat{G}_k)_{ij} = (ρ_m/N)($\hat{G}_M(kl)$)_{ij} = $\rho_m \exp[-(kl)^2|i-j|/6]/N$, where ρ_m is monomer density, l is the length of a polymer link (virtual bond length, denoted as b in Ref. 35), $i, j = 1, 2, \dots, N$ are monomer labels along the polymer chain with N being the length of a chain, and $\hat{\rho} \hat{U}_k = \rho_m \hat{U}_k/N$ [Eq. (4) of Ref. 34].

When $\epsilon_r = \epsilon_r(\phi_m)$, we applied the following modified version of f_{el} [Eq. (68) of Ref. 35]:

$$f_{\text{el}} = \int \frac{d\tilde{k}\tilde{k}^2}{4\pi^2} \left\{ \frac{1}{\eta} \ln [1 + \eta \mathcal{G}_1(\tilde{k})] - \mathcal{G}_2(\tilde{k}) \right\}, \quad (\text{S14})$$

where $\tilde{k} = kb$, $\eta = (b/a)^3$ and, in the absence of salt and counterions, Eqs. (69a) and (69b) of Ref. 35 become

$$\mathcal{G}_1(\tilde{k}) = \frac{4\pi}{\tilde{k}^2[1 + \tilde{k}^2]T_0^* \epsilon_r(\phi_m)} \left(\frac{\phi_m}{N} \langle \sigma | \hat{G}_M(\tilde{k}) | \sigma \rangle \right), \quad (\text{S15a})$$

$$\mathcal{G}_2(\tilde{k}) = \frac{4\pi}{\tilde{k}^2[1 + \tilde{k}^2]T_0^* \epsilon_r(\phi_m)} \left(\frac{\phi_m}{N} \sum_{i=1}^N |\sigma_i| \right). \quad (\text{S15b})$$

As in Refs. 35 and 37, column vector $|\sigma\rangle$ is the charge sequence—its i th element, σ_i , being the charge of the i th monomer (residue) of the IDR in units of the electronic charge e , and $\langle \sigma | \equiv |\sigma\rangle^T$; $T_0^* \equiv 4\pi\epsilon_0 k_B T b / e^2$ is a reduced temperature. As noted above, ϵ_0 is vacuum permittivity, k_B is Boltzmann constant, and T is absolute temperature. Previously,^{35,37} expressions such as above Eqs. (S14) and (S15) for $\epsilon_r(\phi_m)$ were obtained heuristically by replacing every instance of ϵ_r in the corresponding constant- ϵ_r expressions by $\epsilon_r(\phi_m)$.

CONCENTRATION-DEPENDENT PERMITTIVITY IN THE RPA CONTEXT

We now examine whether—and if so what—restrictive conditions have to be satisfied for the heuristic prescription Eqs. (S14) and (S15) to be valid.

When ϵ_r is position-independent, the electrostatic interaction energy (potential), in units of $k_B T$, between two unit point charges e at positions \mathbf{r} and \mathbf{r}' is given by $\mathcal{U}(\mathbf{r}, \mathbf{r}') = \mathcal{U}(\mathbf{r} - \mathbf{r}') = e^2 / (4\pi\epsilon_0\epsilon_r k_B T |\mathbf{r} - \mathbf{r}'|)$. However, when ϵ_r is position-dependent, i.e., $\epsilon_r = \epsilon_r(\mathbf{r})$, in general the electrostatic potential \mathcal{U} is not expressible in a simple closed form because it is the solution to the generalized Poisson equation

$$-\nabla_{\mathbf{r}} \cdot [\epsilon_r(\mathbf{r}) \nabla_{\mathbf{r}} \mathcal{U}(\mathbf{r} - \mathbf{r}')] = 4\pi l_B \delta(\mathbf{r} - \mathbf{r}') , \quad (\text{S16})$$

as noted by Wang,¹¹⁵ where $l_B = e^2 / (4\pi\epsilon_0 k_B T)$ is vacuum Bjerrum length (unlike Ref. 35, here l_B does not include ϵ_r). Thus, position dependence of ϵ_r can entail rather complex modifications of the charge-charge interactions. It cannot be analytically treated, in general, by simply replacing the constant ϵ_r in $\mathcal{U}(\mathbf{r}, \mathbf{r}') = e^2 / (4\pi\epsilon_0\epsilon_r k_B T |\mathbf{r} - \mathbf{r}'|)$ by $\epsilon_r(\mathbf{r})$ or $\epsilon_r(\mathbf{r}')$.

Another concern is that, by construction, RPA theory accounts only for the lowest-order polymer density fluctuations beyond the mean-field homogeneous density. In contrast, some of the proposed IDR-concentration-dependent form of $\epsilon_r = \epsilon_r(\phi_m)$, such as the “slab”¹¹² and Clausius-Mossotti¹³² models and the effective medium approximations of Maxwell Garnett and of Bruggeman¹³³ considered in Refs. 35, 37 involve higher-order dependence on ϕ_m , raising questions as to whether application of these $\epsilon_r(\phi_m)$ formula in the context of RPA is consistent with the basic premises of RPA. We address these issues below.

DERIVATION OF RPA WITH CONCENTRATION-DEPENDENT PERMITTIVITY

Unless specified otherwise, the notation in this subsection follows that of Ref. 41, as the following formal development is, on one hand, a restricted case of the theory in Ref. 41 in that here we do not consider salt, counterions or Kuhn-length renormalization. On the other hand, the present analysis is an extension of the theory in Ref. 41, which is limited to constant ϵ_r s, to case with a position-dependent $\epsilon_r(\mathbf{r})$. Accordingly, we note that the number of chains in the system, which is symbolized by n in the main text and elsewhere in this Supporting Information, is denoted by n_p (following Ref. 41) in the derivation below.

In general, the Boltzmann factor for the electrostatic interaction energy of a system with charge density $\rho(\mathbf{r})$ is given by $\exp[-(1/2) \int d\mathbf{r} d\mathbf{r}' \rho(\mathbf{r}) \mathcal{U}(\mathbf{r}, \mathbf{r}') \rho(\mathbf{r}')]$. (Note that the electric charge density $\rho(\mathbf{r})$ here and in subsequent development in this section should not be confused with the matter density operator $\hat{\rho}$ or its matrix elements.) We focus first on obtaining an equivalent mathematical form of this factor that is amenable to RPA analyses. By standard field-theoretic Hubbard-Stratonovich transformation, this factor may

be expressed as a functional integral over a conjugate field $\psi(\mathbf{r})$:

$$\frac{1}{(\det \hat{\mathcal{U}})^{1/2}} \left\{ \prod_{\mathbf{r}} \int \frac{d\psi(\mathbf{r})}{\sqrt{2\pi}} \right\} \exp \left[-\frac{1}{2} \int d\mathbf{r}' d\mathbf{r}'' \psi(\mathbf{r}') \mathcal{U}^{-1}(\mathbf{r}', \mathbf{r}'') \psi(\mathbf{r}'') - i \int d\mathbf{r}' \rho(\mathbf{r}') \psi(\mathbf{r}') \right], \quad (\text{S17})$$

where $\hat{\mathcal{U}}$ denotes, in matrix notation, the operator $\mathcal{U}(\mathbf{r}, \mathbf{r}')$ [i.e., the matrix element $\hat{\mathcal{U}}_{\mathbf{r}, \mathbf{r}'} = \mathcal{U}(\mathbf{r}, \mathbf{r}')$], $\mathcal{U}^{-1}(\mathbf{r}', \mathbf{r}'')$ is the $\mathbf{r}', \mathbf{r}''$ matrix element of the inverse operator $\hat{\mathcal{U}}^{-1}$ of $\hat{\mathcal{U}}$. By definition, $\int d\mathbf{r}'' \mathcal{U}^{-1}(\mathbf{r}, \mathbf{r}'') \mathcal{U}(\mathbf{r}'', \mathbf{r}') = \delta(\mathbf{r} - \mathbf{r}')$. Consider now the operator $-\nabla_{\mathbf{r}''} \cdot [\epsilon_{\mathbf{r}}(\mathbf{r}'') \nabla_{\mathbf{r}''} \delta(\mathbf{r} - \mathbf{r}'')]/(4\pi l_{\text{B}})$. Since

$$\begin{aligned} \int d\mathbf{r}'' \{ \nabla_{\mathbf{r}''} \cdot [\epsilon_{\mathbf{r}}(\mathbf{r}'') \nabla_{\mathbf{r}''} \delta(\mathbf{r} - \mathbf{r}'')] \} \mathcal{U}(\mathbf{r}'', \mathbf{r}') &= \int d\mathbf{r}'' [\epsilon_{\mathbf{r}}(\mathbf{r}'') \nabla_{\mathbf{r}''} \delta(\mathbf{r} - \mathbf{r}'')] \cdot \nabla_{\mathbf{r}''} \mathcal{U}(\mathbf{r}'', \mathbf{r}') \\ &= \int d\mathbf{r}'' \delta(\mathbf{r} - \mathbf{r}'') \{ \nabla_{\mathbf{r}''} \cdot [\epsilon_{\mathbf{r}}(\mathbf{r}'') \nabla_{\mathbf{r}''} \mathcal{U}(\mathbf{r}'', \mathbf{r}') \} \end{aligned} \quad (\text{S18})$$

follows from repeated applications of integration by parts under the reasonable assumption that the values of the integrand cancel or vanish at the pertinent boundaries of integration, and by Eq. (S16) the quantity in curly brackets in the last term in Eq. (S18) is $-4\pi l_{\text{B}} \delta(\mathbf{r}'' - \mathbf{r}')$, Eq. (S18) is evaluated as $-4\pi l_{\text{B}} \int d\mathbf{r}'' \delta(\mathbf{r} - \mathbf{r}'') \delta(\mathbf{r}'' - \mathbf{r}') = -4\pi l_{\text{B}} \delta(\mathbf{r} - \mathbf{r}')$ and therefore $-\nabla_{\mathbf{r}''} \cdot [\epsilon_{\mathbf{r}}(\mathbf{r}'') \nabla_{\mathbf{r}''} \delta(\mathbf{r} - \mathbf{r}'')]/(4\pi l_{\text{B}})$ is the \mathbf{r}, \mathbf{r}'' matrix element of the inverse of $\hat{\mathcal{U}}$, viz.,

$$\mathcal{U}^{-1}(\mathbf{r}, \mathbf{r}'') = -\frac{1}{4\pi l_{\text{B}}} \nabla_{\mathbf{r}''} \cdot [\epsilon_{\mathbf{r}}(\mathbf{r}'') \nabla_{\mathbf{r}''} \delta(\mathbf{r} - \mathbf{r}'')] . \quad (\text{S19})$$

Equivalently, the \mathbf{r}'', \mathbf{r} matrix element of $\hat{\mathcal{U}}^{-1}$ takes the form

$$\mathcal{U}^{-1}(\mathbf{r}'', \mathbf{r}) = -\frac{1}{4\pi l_{\text{B}}} \nabla_{\mathbf{r}} \cdot [\epsilon_{\mathbf{r}}(\mathbf{r}) \nabla_{\mathbf{r}} \delta(\mathbf{r}'' - \mathbf{r})] . \quad (\text{S20})$$

It follows that the $-(1/2) \int d\mathbf{r}' d\mathbf{r}'' \psi(\mathbf{r}') \mathcal{U}^{-1}(\mathbf{r}', \mathbf{r}'') \psi(\mathbf{r}'')$ factor in Eq. (S17) is given by

$$\begin{aligned} -\frac{1}{2} \int d\mathbf{r}' d\mathbf{r}'' \psi(\mathbf{r}') \mathcal{U}^{-1}(\mathbf{r}', \mathbf{r}'') \psi(\mathbf{r}'') &= \frac{1}{8\pi l_{\text{B}}} \int d\mathbf{r} d\mathbf{r}' \psi(\mathbf{r}) \{ \nabla_{\mathbf{r}'} \cdot [\epsilon_{\mathbf{r}}(\mathbf{r}') \nabla_{\mathbf{r}'} \delta(\mathbf{r} - \mathbf{r}')] \} \psi(\mathbf{r}') \\ &= -\frac{1}{8\pi l_{\text{B}}} \int d\mathbf{r} d\mathbf{r}' \psi(\mathbf{r}) [\epsilon_{\mathbf{r}}(\mathbf{r}') \nabla_{\mathbf{r}'} \delta(\mathbf{r} - \mathbf{r}')] \cdot [\nabla_{\mathbf{r}'} \psi(\mathbf{r}')] \\ &= \frac{1}{8\pi l_{\text{B}}} \int d\mathbf{r} d\mathbf{r}' \psi(\mathbf{r}) [\epsilon_{\mathbf{r}}(\mathbf{r}') \nabla_{\mathbf{r}} \delta(\mathbf{r} - \mathbf{r}')] \cdot [\nabla_{\mathbf{r}'} \psi(\mathbf{r}')] \\ &= -\frac{1}{8\pi l_{\text{B}}} \int d\mathbf{r} d\mathbf{r}' \epsilon_{\mathbf{r}}(\mathbf{r}') \delta(\mathbf{r} - \mathbf{r}') [\nabla_{\mathbf{r}} \psi(\mathbf{r}')] \cdot [\nabla_{\mathbf{r}'} \psi(\mathbf{r}')] \\ &= -\frac{1}{8\pi l_{\text{B}}} \int d\mathbf{r} \epsilon_{\mathbf{r}}(\mathbf{r}) [\nabla_{\mathbf{r}} \psi(\mathbf{r})] \cdot [\nabla_{\mathbf{r}} \psi(\mathbf{r})] \\ &= -\frac{1}{8\pi l_{\text{B}}} \int d\mathbf{r} \epsilon_{\mathbf{r}}(\mathbf{r}) |\nabla \psi(\mathbf{r})|^2 , \end{aligned} \quad (\text{S21})$$

where the first equality follows from a mere change in the integration variable, the second and fourth equalities from integration by parts assuming that boundary contribution vanishes, the third equality from $\nabla_{\mathbf{r}'}\delta(\mathbf{r}-\mathbf{r}') = -\nabla_{\mathbf{r}}\delta(\mathbf{r}-\mathbf{r}')$, and the \mathbf{r} subscript of $\nabla_{\mathbf{r}}$ is dropped in the final expression because there is little danger of notational ambiguity. Equation (S21) is identical to the corresponding terms in the Hamiltonians in Eq. (3) of Ref. 134 and Eq. (2.7) of Ref. 115 for systems with an inhomogeneous dielectric medium.

We turn next to the $(\det \hat{\mathcal{U}})^{-1/2}$ factor in Eq. (S17). For any matrices A and B , $(\det A)^{-1} = (\det A^{-1})$ and $(\det AB) = (\det A)(\det B)$, we write $(\det \hat{\mathcal{U}})^{-1/2} = (\det \hat{\mathcal{U}}^{-1})^{1/2} = (\det \hat{\epsilon}_{\mathbf{r}})^{1/2}(\det \hat{\mathcal{U}}_0^{-1})^{1/2}$, where $\hat{\mathcal{U}}^{-1}$'s matrix elements $\mathcal{U}_{\mathbf{r}\mathbf{r}'}^{-1} \equiv \mathcal{U}^{-1}(\mathbf{r}, \mathbf{r}')$ is given by Eq. (S19), the \mathbf{r}, \mathbf{r}' matrix elements of the operators $\hat{\epsilon}_{\mathbf{r}}$ and $\hat{\mathcal{U}}_0^{-1}$ are defined, respectively, by

$$(\hat{\epsilon}_{\mathbf{r}})_{\mathbf{r}\mathbf{r}'} \equiv \epsilon_{\mathbf{r}}(\mathbf{r})\delta(\mathbf{r}-\mathbf{r}') , \quad (\text{S22})$$

$$(\hat{\mathcal{U}}_0^{-1})_{\mathbf{r}\mathbf{r}'} \equiv -\frac{1}{4\pi l_{\text{B}}}\nabla_{\mathbf{r}}^2\delta(\mathbf{r}-\mathbf{r}') . \quad (\text{S23})$$

Then, $\hat{\epsilon}_{\mathbf{r}}\hat{\mathcal{U}}_0^{-1} = \hat{\mathcal{U}}^{-1}$ can be readily verified using integration by parts:

$$\begin{aligned} (\hat{\epsilon}_{\mathbf{r}}\hat{\mathcal{U}}_0^{-1})_{\mathbf{r}\mathbf{r}'} &= \int d\mathbf{r}'' (\hat{\epsilon}_{\mathbf{r}})_{\mathbf{r}\mathbf{r}''} (\hat{\mathcal{U}}_0^{-1})_{\mathbf{r}''\mathbf{r}'} \\ &= -\frac{1}{4\pi l_{\text{B}}}\int d\mathbf{r}'' \epsilon_{\mathbf{r}}(\mathbf{r})\delta(\mathbf{r}-\mathbf{r}'')\nabla_{\mathbf{r}''}^2\delta(\mathbf{r}''-\mathbf{r}') \\ &= \frac{1}{4\pi l_{\text{B}}}\int d\mathbf{r}'' \epsilon_{\mathbf{r}}(\mathbf{r}'')[\nabla_{\mathbf{r}''}\delta(\mathbf{r}-\mathbf{r}'')] \cdot [\nabla_{\mathbf{r}''}\delta(\mathbf{r}''-\mathbf{r}')] \\ &= -\frac{1}{4\pi l_{\text{B}}}\int d\mathbf{r}'' \nabla_{\mathbf{r}''} \cdot \{\epsilon_{\mathbf{r}}(\mathbf{r}'')[\nabla_{\mathbf{r}''}\delta(\mathbf{r}-\mathbf{r}'')]\}\delta(\mathbf{r}''-\mathbf{r}') \\ &= -\frac{1}{4\pi l_{\text{B}}}\nabla_{\mathbf{r}'} \cdot [\epsilon_{\mathbf{r}}(\mathbf{r}')\nabla_{\mathbf{r}'}\delta(\mathbf{r}-\mathbf{r}')] \\ &= \hat{\mathcal{U}}_{\mathbf{r}\mathbf{r}'}^{-1} , \text{ Q.E.D.} \end{aligned} \quad (\text{S24})$$

Because $\hat{\epsilon}_{\mathbf{r}}$ in Eq. (S22) is a diagonal matrix,

$$(\det \hat{\epsilon}_{\mathbf{r}}) = \prod_{\mathbf{r}} \epsilon_{\mathbf{r}}(\mathbf{r}) . \quad (\text{S25})$$

Using Fourier transformation from \mathbf{r} to \mathbf{k} space,⁴¹

$$(\det \hat{\mathcal{U}}_0^{-1}) = \prod_{\mathbf{k} \neq \mathbf{0}} \frac{k^2}{4\pi l_{\text{B}}} , \quad (\text{S26})$$

where $k^2 \equiv |\mathbf{k}|^2$. Note that the $\mathbf{k} = \mathbf{0}$ term is excluded in the above and subsequent considerations because it does not contribute to the exponential factor in Eq. (S17) for our electrically neutral system of overall neutral polyampholytes.

The free energy per unit volume l^3 in units of $k_B T$ of our system is given by

$$f = \frac{\phi_m}{N} \ln \phi_m + (1 - \phi_m) \ln(1 - \phi_m) - \frac{l^3}{\Omega} \ln \mathcal{Z}_{\text{el}}, \quad (\text{S27})$$

where N is the chain length (number of monomers) of the polyampholyte, Ω is solution (system) volume, $\phi_m \equiv l^3 n_p N / \Omega$ is monomer volume fraction with n_p being the total number of identical polyampholyte chains in the solution [n_p corresponds to the variable n used above in the formulation for explicit-chain simulations; it should also be noted here that the alternately defined $\phi_m = a^3 n_p N / \Omega$ in Eq. (3) of Ref. 35—which applies to Eqs. (S14) and (S15) in the present work—is equal to polyampholyte volume fraction only when the size of a monomer $\approx l^3$ is equal to the model volume unit a^3 of the model, i.e., when $r_m = 1$; whereas polyampholyte volume fraction is given by $r_m \phi_m$ in general³⁵; for simplicity, $r_m = 1$ is assumed below unless specified otherwise], and \mathcal{Z}_{el} is the electrostatic partition function, which may be viewed as a special case of \mathcal{Z}' in Eq. (A9) of Ref. 41 with no salt, no counterion, and $v_2 = 0$, but now extended to $\epsilon_r = \epsilon_r(\mathbf{r})$. \mathcal{Z}_{el} is given by integrals over monomer coordinates,

$$\mathcal{Z}_{\text{el}} = \int \prod_{\alpha=1}^{n_p} \prod_{\tau=1}^N d\mathbf{R}_{\alpha,\tau} e^{-\mathcal{H}[\mathbf{R}]}, \quad (\text{S28})$$

where $\mathbf{R}_{\alpha,\tau}$ denotes the coordinate of the τ th monomer in the α th polyampholyte [$\mathbf{R}_{\alpha,\tau}$ corresponds to the position variable $\mathbf{R}_{\mu i}$ defined before Eq. (S1) in the formulation for explicit-chain simulations; the monomer label τ corresponds also to the label i in Eq. (S15b)], and

$$\mathcal{H}[\mathbf{R}] = \frac{3}{2l^2} \sum_{\alpha=1}^{n_p} \sum_{\tau=1}^{N-1} (\mathbf{R}_{\alpha,\tau+1} - \mathbf{R}_{\alpha,\tau})^2 + \frac{1}{2} \sum_{\alpha,\beta=1}^{n_p} \sum_{\tau,\mu=1}^N \mathcal{V}_{\alpha\beta}^{\tau\mu}(\mathbf{R}_{\alpha,\tau}, \mathbf{R}_{\beta,\mu}). \quad (\text{S29})$$

The first term of $\mathcal{H}[\mathbf{R}]$ is for Gaussian-chain connectivity of the polyampholyte chains and $\mathcal{V}_{\alpha\beta}^{\tau\mu}$ in the second term is the interaction potential energy between the τ th monomer in the α th chain and the μ th monomer in the β th chain, viz.,

$$\mathcal{V}_{\alpha\beta}^{\tau\mu}(\mathbf{r}, \mathbf{r}') = l_B \sigma_\tau \sigma_\mu \mathcal{U}(\mathbf{r}, \mathbf{r}'), \quad (\text{S30})$$

where σ_τ, σ_μ are the charges, respectively, of monomers τ, μ along each of the n_p polyampholyte chains. We may now rewrite Eq. (S28) as a functional integral over the charge density $\rho(\mathbf{r})$ by including in the integrand a δ -functional for $\rho(\mathbf{r})$:

$$\mathcal{Z}_{\text{el}} = \int \prod_{\mathbf{r}} d\rho(\mathbf{r}) \int \prod_{\alpha=1}^{n_p} \prod_{\tau=1}^N d\mathbf{R}_{\alpha,\tau} e^{-\mathcal{H}[\rho, \mathbf{R}]} \delta[\rho(\mathbf{r}) - \sum_{\alpha=1}^{n_p} \sum_{\tau=1}^N \sigma_\tau \delta(\mathbf{r} - \mathbf{R}_{\alpha,\tau})], \quad (\text{S31})$$

which follows from $\rho(\mathbf{r}) = \sum_{\alpha=1}^{n_p} \sum_{\tau=1}^N \sigma_{\tau} \delta(\mathbf{r} - \mathbf{R}_{\alpha,\tau})$, whereas $\mathcal{H}[\rho, \mathbf{R}]$ is defined as

$$\mathcal{H}[\rho, \mathbf{R}] = \frac{3}{2l^2} \sum_{\alpha=1}^{n_p} \sum_{\tau=1}^{N-1} (\mathbf{R}_{\alpha,\tau+1} - \mathbf{R}_{\alpha,\tau})^2 + \frac{1}{2} \int d\mathbf{r} d\mathbf{r}' \rho(\mathbf{r}) \mathcal{U}(\mathbf{r}, \mathbf{r}') \rho(\mathbf{r}') . \quad (\text{S32})$$

Now, by applying Eqs. (S17) and (S21), the partition function \mathcal{Z}_{el} in Eq. (S31) may be expressed as a functional integral over $\rho(\mathbf{r})$, $\mathbf{R}_{\alpha,\tau}$, and the conjugate fields $\psi(\mathbf{r})$:

$$\begin{aligned} \mathcal{Z}_{\text{el}} = & \int \prod_{\mathbf{r}} d\rho(\mathbf{r}) \int \prod_{\alpha=1}^{n_p} \prod_{\tau=1}^N d\mathbf{R}_{\alpha,\tau} \exp \left[-\frac{3}{2l^2} \sum_{\alpha=1}^{n_p} \sum_{\tau=1}^{N-1} (\mathbf{R}_{\alpha,\tau+1} - \mathbf{R}_{\alpha,\tau})^2 \right] \\ & \times \frac{1}{(\det \hat{\mathcal{U}})^{1/2}} \left\{ \prod_{\mathbf{r}} \int \frac{d\psi(\mathbf{r})}{\sqrt{2\pi}} \right\} \exp \left[-\frac{1}{8\pi l_B} \int d\mathbf{r} \epsilon_r(\mathbf{r}) |\nabla \psi(\mathbf{r})|^2 - i \int d\mathbf{r}' \rho(\mathbf{r}') \psi(\mathbf{r}') \right] \\ & \times \delta \left[\rho(\mathbf{r}) - \sum_{\alpha=1}^{n_p} \sum_{\tau=1}^N \sigma_{\tau} \delta(\mathbf{r} - \mathbf{R}_{\alpha,\tau}) \right] . \end{aligned} \quad (\text{S33})$$

After performing the $\prod_{\mathbf{r}} d\rho(\mathbf{r})$ functional integrals in the above expression, \mathcal{Z}_{el} becomes

$$\mathcal{Z}_{\text{el}} = \int \prod_{\alpha=1}^{n_p} \prod_{\tau=1}^N d\mathbf{R}_{\alpha,\tau} \frac{1}{(\det \hat{\mathcal{U}})^{1/2}} \left\{ \prod_{\mathbf{r}} \int \frac{d\psi(\mathbf{r})}{\sqrt{2\pi}} \right\} e^{-\mathcal{H}[\psi, \mathbf{R}]}, \quad (\text{S34})$$

where

$$\mathcal{H}[\psi, \mathbf{R}] = \frac{3}{2l^2} \sum_{\alpha=1}^{n_p} \sum_{\tau=1}^{N-1} (\mathbf{R}_{\alpha,\tau+1} - \mathbf{R}_{\alpha,\tau})^2 + \frac{1}{8\pi l_B} \int d\mathbf{r} \epsilon_r(\mathbf{r}) |\nabla \psi(\mathbf{r})|^2 + i \sum_{\alpha=1}^{n_p} \sum_{\tau=1}^N \sigma_{\tau} \psi(\mathbf{R}_{\alpha,\tau}) . \quad (\text{S35})$$

We now proceed to evaluate the $(\det \hat{\mathcal{U}})^{-1/2}$ factor in Eq. (S34) via the aforementioned relations $(\det \hat{\mathcal{U}})^{-1/2} = (\det \hat{\mathcal{U}}^{-1})^{1/2}$ and $\hat{\mathcal{U}}^{-1} = \hat{\epsilon}_r \hat{\mathcal{U}}_0^{-1}$. Using Eq. (S25) and applying the correspondence

$$\sum_{\mathbf{r}} \rightarrow \frac{\mathcal{N}_r}{\Omega} \int d\mathbf{r} \quad (\text{S36})$$

where \mathcal{N}_r is formally the number of \mathbf{r} positions in the system, we may write

$$\sqrt{\det \hat{\epsilon}_r} = \prod_{\mathbf{r}} \sqrt{\epsilon_r(\mathbf{r})} = \exp \left\{ \frac{1}{2} \sum_{\mathbf{r}} \ln[\epsilon_r(\mathbf{r})] \right\} = \exp \left\{ \frac{\mathcal{N}_r}{2\Omega} \int d\mathbf{r} \ln[\epsilon_r(\mathbf{r})] \right\} . \quad (\text{S37})$$

For reasons to be enunciated below, consider the case in which $\epsilon_r(\mathbf{r})$ is a linear combination of polyampholyte and water relative permittivities, i.e.,

$$\epsilon_r(\mathbf{r}) = \epsilon_p \phi_m(\mathbf{r}) + \epsilon_w [1 - \phi_m(\mathbf{r})] = \epsilon_w + \epsilon' \phi_m(\mathbf{r}) , \quad (\text{S38})$$

where ϵ_p and ϵ_w are, respectively, the relative permittivities of polymer and water, and $\epsilon' = \epsilon_p - \epsilon_w$. Since the position-dependent monomer density

$$\phi_m(\mathbf{r}) = l^3 \sum_{\alpha=1}^{n_p} \sum_{\tau=1}^N \delta(\mathbf{r} - \mathbf{R}_{\alpha,\tau}) , \quad (\text{S39})$$

$$\begin{aligned} \ln[\epsilon_r(\mathbf{r})] &= \ln \epsilon_w + \ln \left[1 + \frac{\epsilon'}{\epsilon_w} \phi_m(\mathbf{r}) \right] \\ &= \ln \epsilon_w + \ln \left[1 + \frac{\epsilon' l^3}{\epsilon_w} \sum_{\alpha=1}^{n_p} \sum_{\tau=1}^N \delta(\mathbf{r} - \mathbf{R}_{\alpha,\tau}) \right] . \end{aligned} \quad (\text{S40})$$

To be consistent with RPA which accounts only for lowest-order polymer density fluctuations, we approximate the above expression for $\ln[\epsilon_r(\mathbf{r})]$ by including terms only up to the one linear in ϕ_m , viz.,

$$\ln[\epsilon_r(\mathbf{r})] \approx \ln \epsilon_w + \frac{\epsilon' l^3}{\epsilon_w} \sum_{\alpha=1}^{n_p} \sum_{\tau=1}^N \delta(\mathbf{r} - \mathbf{R}_{\alpha,\tau}) . \quad (\text{S41})$$

Hence the argument of the exponential function in Eq. (S37) is given by

$$\begin{aligned} \frac{\mathcal{N}_r}{2\Omega} \int d\mathbf{r} \ln[\epsilon_r(\mathbf{r})] &\approx \frac{\mathcal{N}_r}{2} \ln \epsilon_w + \frac{\mathcal{N}_r \epsilon' l^3 n_p N}{2\epsilon_w \Omega} = \frac{\mathcal{N}_r}{2} \ln \epsilon_w + \frac{\mathcal{N}_r \epsilon'}{2\epsilon_w} \phi_m \\ &\approx \frac{\mathcal{N}_r}{2} \ln \epsilon_w + \frac{\mathcal{N}_r}{2} \ln \left(1 + \frac{\epsilon'}{\epsilon_w} \phi_m \right) \\ &= \frac{\mathcal{N}_r}{2} \ln[\epsilon_r(\phi_m)] , \end{aligned} \quad (\text{S42})$$

where the position-independent $\phi_m \equiv (l^3/\Omega) \int d\mathbf{r} \sum_{\alpha=1}^{n_p} \sum_{\tau=1}^N \delta(\mathbf{r} - \mathbf{R}_{\alpha,\tau}) = l^3 n_p N / \Omega$ is the overall average monomer volume fraction, the second approximate relation is in line with that in Eq. (S41), and the last equality follows from definition Eq. (S38). In formulations involving a size-dependent mean-field lattice model with ϕ_m defined in terms of unit volume $a^3 \neq l^3$ (Ref. 35), the actual average monomer volume fraction ϕ is given by $\phi = r_m \phi_m$ where r_m is the monomer size factor, in which case $\epsilon_r(\phi_m)$ is understood to represent the ϵ_r expression in which all ϕ_m is replaced by $\phi = r_m \phi_m$; i.e., $\epsilon_r(\phi_m) \rightarrow \epsilon_r(\phi_m \rightarrow \phi = r_m \phi_m)$. With Eq. (S42), further application of Eqs. (S26) and (S37) yields

$$\begin{aligned} (\det \hat{\mathcal{U}})^{-1/2} &= \sqrt{\det \hat{\epsilon}_r} \sqrt{\det \hat{\mathcal{U}}_0^{-1}} \approx \left[\sqrt{\epsilon_r(\phi_m)} \right]^{\mathcal{N}_r} \prod_{\mathbf{k} \neq \mathbf{0}} \sqrt{\frac{k^2}{4\pi l_B}} \\ &= \prod_{\mathbf{k} \neq \mathbf{0}} \sqrt{\frac{k^2 [\epsilon_r(\phi_m)]^{\mathcal{N}_r / (\mathcal{N}_r - 1)}}{4\pi l_B}} \approx \prod_{\mathbf{k} \neq \mathbf{0}} \sqrt{\frac{k^2 \epsilon_r(\phi_m)}{4\pi l_B}} \end{aligned} \quad (\text{S43})$$

for the $(\det \hat{U})^{-1/2}$ factor in Eq. (S34). To arrive at this expression, we made use of the fact that the total number of reciprocal space positions \mathbf{k} is $\mathcal{N}_{\mathbf{r}}$ (same as the total number of coordinate space positions \mathbf{r} when $\mathbf{k} = \mathbf{0}$ is included in the count), and that $\mathcal{N}_{\mathbf{r}} \gg 1$. It follows that \mathcal{Z}_{el} in Eq. (S34) may be written as

$$\mathcal{Z}_{\text{el}} = \left\{ \prod_{\mathbf{k} \neq \mathbf{0}} \sqrt{\frac{k^2 \epsilon_{\mathbf{r}}(\phi_m)}{4\pi l_{\text{B}}}} \right\} \int \prod_{\alpha=1}^{n_p} \prod_{\tau=1}^N d\mathbf{R}_{\alpha,\tau} \left\{ \prod_{\mathbf{r}} \int \frac{d\psi(\mathbf{r})}{\sqrt{2\pi}} \right\} e^{-\mathcal{H}[\psi, \mathbf{R}]}, \quad (\text{S44})$$

where $\mathcal{H}[\psi, \mathbf{R}]$ is given by Eq. (S35) with $\epsilon_{\mathbf{r}}(\mathbf{r})$ given by Eq. (S38):

$$\begin{aligned} \mathcal{H}[\psi, \mathbf{R}] &= \frac{\epsilon_w}{8\pi l_{\text{B}}} \int d\mathbf{r} [\nabla \psi(\mathbf{r})]^2 + \frac{\epsilon'}{8\pi l_{\text{B}}} \int d\mathbf{r} \phi_m(\mathbf{r}) [\nabla \psi(\mathbf{r})]^2 \\ &\quad + \frac{3}{2l^2} \sum_{\alpha=1}^{n_p} \sum_{\tau=1}^{N-1} (\mathbf{R}_{\alpha,\tau+1} - \mathbf{R}_{\alpha,\tau})^2 + i \sum_{\alpha=1}^{n_p} \sum_{\tau=1}^N \sigma_{\tau} \psi(\mathbf{R}_{\alpha,\tau}) \\ &= \frac{\epsilon_w}{8\pi l_{\text{B}}} \int d\mathbf{r} [\nabla \psi(\mathbf{r})]^2 + \sum_{\alpha=1}^{n_p} \left\{ \frac{3}{2l^2} \sum_{\tau=1}^{N-1} (\mathbf{R}_{\alpha,\tau+1} - \mathbf{R}_{\alpha,\tau})^2 \right. \\ &\quad \left. + \sum_{\tau=1}^N \left[i\sigma_{\tau} \psi(\mathbf{R}_{\alpha,\tau}) + \frac{\epsilon' l^3}{8\pi l_{\text{B}}} [\nabla \psi(\mathbf{R}_{\alpha,\tau})]^2 \right] \right\}, \end{aligned} \quad (\text{S45})$$

where Eq. (S39) for $\phi_m(\mathbf{r})$ has been applied to yield the last equality. Utilizing the Fourier transformation $\psi_{\mathbf{k}} = (\Omega/\mathcal{N}_{\mathbf{r}}) \sum_{\mathbf{r}} \psi(\mathbf{r}) \exp(-i\mathbf{k} \cdot \mathbf{r})$ of the conjugate field $\psi(\mathbf{r})$ [which may then be expressed as the inverse transformation of $\psi_{\mathbf{k}}$, i.e., $\psi(\mathbf{r}) = (1/\Omega) \sum_{\mathbf{k}} \psi_{\mathbf{k}} \exp(i\mathbf{k} \cdot \mathbf{r})$] and the $\sum_{\mathbf{r}} \leftrightarrow (\mathcal{N}_{\mathbf{r}}/\Omega) \int d\mathbf{r}$ correspondence in Eq. (S36), the first term in the above Eq. (S45) can be rewritten as

$$\begin{aligned} \frac{\epsilon_w}{8\pi l_{\text{B}}} \int d\mathbf{r} [\nabla \psi(\mathbf{r})]^2 &\rightarrow \frac{\epsilon_w}{8\pi l_{\text{B}}} \left(\frac{\Omega}{\mathcal{N}_{\mathbf{r}}} \right) \sum_{\mathbf{r}} \left[\left(\frac{1}{\Omega} \sum_{\mathbf{k}} \psi_{\mathbf{k}} \nabla e^{-i\mathbf{k} \cdot \mathbf{r}} \right) \cdot \left(\frac{1}{\Omega} \sum_{\mathbf{k}'} \psi_{\mathbf{k}'} \nabla e^{-i\mathbf{k}' \cdot \mathbf{r}} \right) \right] \\ &= -\frac{\epsilon_w \Omega}{8\pi l_{\text{B}}} \frac{1}{\Omega^2} \sum_{\mathbf{k}} \sum_{\mathbf{k}'} \psi_{\mathbf{k}} (\mathbf{k} \cdot \mathbf{k}') \psi_{\mathbf{k}'} \delta_{\mathbf{k}+\mathbf{k}'} \\ &= \frac{1}{2\Omega} \sum_{\mathbf{k}} \frac{\epsilon_w k^2}{4\pi l_{\text{B}}} \psi_{\mathbf{k}} \psi_{-\mathbf{k}} = \frac{1}{2\Omega} \sum_{\mathbf{k} \neq \mathbf{0}} \frac{\epsilon_w k^2}{4\pi l_{\text{B}}} \psi_{\mathbf{k}} \psi_{-\mathbf{k}}, \end{aligned} \quad (\text{S46})$$

where the last equality follows because the $\mathbf{k} = \mathbf{0}$ term vanishes by virtue of the k^2 factor. The remaining terms of $\mathcal{H}[\psi, \mathbf{R}]$ in Eq. (S45) can be rewritten as the summation of contributions from n_p independent polymers, as follows. Consider the partition function

$$\mathcal{Q}_p[\psi] = \int \mathcal{D}[\mathbf{R}] e^{-\mathcal{H}_p[\psi, \mathbf{R}]} \quad (\text{S47})$$

for a single polymer, where $\mathcal{D}[\mathbf{R}] = \prod_{\tau=1}^N d\mathbf{R}_\tau$, and

$$\begin{aligned}
\mathcal{H}_p[\psi, \mathbf{R}] &\equiv \frac{3}{2l^2} \sum_{\tau=1}^{N-1} (\mathbf{R}_{\tau+1} - \mathbf{R}_\tau)^2 \\
&\quad + \sum_{\tau=1}^N \left[\frac{i}{\Omega} \sum_{\mathbf{k}} \sigma_\tau \psi_{\mathbf{k}} e^{-i\mathbf{k} \cdot \mathbf{R}_\tau} - \frac{\epsilon' l^3}{8\pi l_B} \frac{1}{\Omega^2} \sum_{\mathbf{k}} \sum_{\mathbf{k}'} (\mathbf{k} \cdot \mathbf{k}') \psi_{\mathbf{k}} \psi_{\mathbf{k}'} e^{-i(\mathbf{k}+\mathbf{k}') \cdot \mathbf{R}_\tau} \right] \\
&= \frac{3}{2l^2} \sum_{\tau=1}^{N-1} (\mathbf{R}_{\tau+1} - \mathbf{R}_\tau)^2 \\
&\quad + \sum_{\tau=1}^N \left[\frac{i}{\Omega} \sum_{\mathbf{k} \neq \mathbf{0}} \sigma_\tau \psi_{\mathbf{k}} e^{-i\mathbf{k} \cdot \mathbf{R}_\tau} - \frac{\epsilon' l^3}{8\pi l_B} \frac{1}{\Omega^2} \sum_{\mathbf{k}, \mathbf{k}' \neq \mathbf{0}} (\mathbf{k} \cdot \mathbf{k}') \psi_{\mathbf{k}} \psi_{\mathbf{k}'} e^{-i(\mathbf{k}+\mathbf{k}') \cdot \mathbf{R}_\tau} \right].
\end{aligned} \tag{S48}$$

Note that the label α in $\mathbf{R}_{\alpha, \tau}$ is dropped in $\prod_{\tau=1}^N d\mathbf{R}_\tau$ and Eq. (S48) because the pertinent integration is only over the monomer coordinates of a single polymer chain. The $\mathbf{k}, \mathbf{k}' = \mathbf{0}$ terms can be excluded in the summations of the last line of Eq. (S48) because in the first summation $\sum_{\tau=1}^N \sigma_\tau = 0$ for the overall neutral polyampholytes considered here and the $(\mathbf{k} \cdot \mathbf{k}')$ factor in the second summation means that the $\mathbf{k}, \mathbf{k}' = \mathbf{0}$ terms are identically zero.

Utilizing the definition of $\psi(\mathbf{r})$ to $\psi_{\mathbf{k}}$ Fourier transformation stated after Eq. (S45), it can readily be verified that $\mathcal{H}_p[\psi, \mathbf{R}]$ is precisely the \mathbf{k} -space version of the quantity enclosed in curly brackets on the right hand side of Eq. (S45). Upon changing the functional integration variables $\psi(\mathbf{r})$ in Eq. (S44) to $\psi_{\mathbf{k}}$ and including the \mathbf{k} -independent functional Jacobian $|\delta\psi(\mathbf{r})/\delta\psi_{\mathbf{k}}|$ (which have no effect on the configurational distribution of the system),

$$\left\{ \prod_{\mathbf{r}} \int \frac{d\psi(\mathbf{r})}{\sqrt{2\pi}} \right\} \rightarrow \left\{ \prod_{\mathbf{k}} \int \sqrt{\frac{\mathcal{N}_{\mathbf{r}}}{2\pi\Omega^2}} d\psi_{\mathbf{k}} \right\} \tag{S49}$$

formally, and thus Eq. (S44) can now be recast in the equivalent form

$$\begin{aligned}
\mathcal{Z}_{\text{el}} &= \left\{ \prod_{\mathbf{k} \neq \mathbf{0}} \sqrt{\frac{k^2 \epsilon_r(\phi_m)}{4\pi l_B}} \right\} \left\{ \prod_{\mathbf{k}} \int \sqrt{\frac{\mathcal{N}_{\mathbf{r}}}{2\pi\Omega^2}} d\psi_{\mathbf{k}} \right\} \exp \left[-\frac{1}{2\Omega} \sum_{\mathbf{k} \neq \mathbf{0}} \frac{\epsilon_w k^2}{4\pi l_B} \psi_{\mathbf{k}} \psi_{-\mathbf{k}} \right] \\
&\quad \times \int \prod_{\alpha=1}^{n_p} \left\{ \prod_{\tau=1}^N d\mathbf{R}_\tau \exp(-\mathcal{H}_p[\psi, \mathbf{R}]) \right\},
\end{aligned} \tag{S50}$$

where we have made use of the fact that in the above expression, the first exponential factor [from Eq. (S46)] is independent of $\mathbf{R}_{\alpha, \tau}$, and the quantity enclosed in the last set of curly brackets [from Eq. (S48)] is identical for all n_p values of α , thus the entire last line of Eq. (S50) is equal to $n_p \ln \mathcal{Q}_p[\psi]$ in accordance with Eq. (S47). Because, as argued above, there is no $\mathbf{k} = \mathbf{0}$ contribution to $\mathcal{H}_p[\psi, \mathbf{R}]$, the $\prod_{\mathbf{k}} (\mathcal{N}_{\mathbf{r}}/2\pi\Omega^2)^{1/2} \int d\psi_{\mathbf{k}}$ functional integral in Eq. (S50) may be restricted to $\prod_{\mathbf{k} \neq \mathbf{0}} (\mathcal{N}_{\mathbf{r}}/2\pi\Omega^2)^{1/2} \int d\psi_{\mathbf{k}}$ with no impact on configurational

distribution. Therefore, \mathcal{Z}_{el} takes the simplified form:

$$\mathcal{Z}_{\text{el}} = \left\{ \prod_{\mathbf{k} \neq \mathbf{0}} \int \sqrt{\frac{\mathcal{N}_{\mathbf{r}}}{2\pi\Omega^2}} d\psi_{\mathbf{k}} \sqrt{\frac{\epsilon_{\mathbf{r}}(\phi_m)k^2}{4\pi l_{\text{B}}}} \right\} e^{-\mathcal{H}[\psi_{\mathbf{k}}]}, \quad (\text{S51})$$

where

$$\mathcal{H}[\psi_{\mathbf{k}}] = \frac{1}{2\Omega} \sum_{\mathbf{k} \neq \mathbf{0}} \frac{\epsilon_{\text{w}}k^2}{4\pi l_{\text{B}}} \psi_{\mathbf{k}}\psi_{-\mathbf{k}} - n_p \ln \mathcal{Q}_p[\psi]. \quad (\text{S52})$$

We are now in a position to apply RPA by expanding $\ln \mathcal{Q}_p$ around $\psi_{\mathbf{k}} = 0$ up to second order in $\psi_{\mathbf{k}}$,⁴¹ namely

$$\ln \mathcal{Q}_p[\psi] \approx \ln \mathcal{Q}_p[\psi = 0] + \sum_{\mathbf{k}} \left(\frac{\delta \ln \mathcal{Q}_p}{\delta \psi_{\mathbf{k}}} \right)_{\psi=0} \psi_{\mathbf{k}} + \frac{1}{2} \sum_{\mathbf{k}, \mathbf{k}'} \left(\frac{\delta^2 \ln \mathcal{Q}_p}{\delta \psi_{\mathbf{k}} \delta \psi_{\mathbf{k}'}} \right)_{\psi=0} \psi_{\mathbf{k}} \psi_{\mathbf{k}'}, \quad (\text{S53})$$

wherein the zeroth order term (first term on the right hand side) is a constant that plays no role in determining configurational distribution. The first order term

$$\begin{aligned} \left(\frac{\delta \ln \mathcal{Q}_p}{\delta \psi_{\mathbf{k}}} \right)_{\psi=0} &= \frac{1}{\mathcal{Q}_p[\psi = 0]} \left. \frac{\delta \mathcal{Q}_p}{\delta \psi_{\mathbf{k}}} \right|_{\psi=0} \\ &= \sum_{\tau=1}^N \left\langle -\frac{i}{\Omega} \sigma_{\tau} e^{-i\mathbf{k} \cdot \mathbf{R}_{\tau}} + 2 \times \frac{\epsilon' l^3}{8\pi l_{\text{B}}} \frac{1}{\Omega^2} \mathbf{k} \cdot \sum_{\mathbf{k}' \neq \mathbf{0}} \mathbf{k}' \psi_{\mathbf{k}'} e^{-i(\mathbf{k}+\mathbf{k}') \cdot \mathbf{R}_{\tau}} \right\rangle_{\psi=0} \\ &= -\frac{i}{\Omega} \sum_{\tau=1}^N \sigma_{\tau} \langle e^{-i\mathbf{k} \cdot \mathbf{R}_{\tau}} \rangle_{\psi=0} \\ &= 0 \end{aligned} \quad (\text{S54})$$

as well. Here, the average $\langle \dots \rangle_{\psi=0}$ is over monomer coordinates $[\mathbf{R}]$ and evaluated at $\psi_{\mathbf{k}} = 0$, the third equality follows because the second term in the second line of the above equation contains a factor of ψ that is set to zero, and the last equality is a consequence of the overall neutrality of the polyampholytes in the system we considered ($\sum_{\tau=1}^N \sigma_{\tau} = 0$). The second order term in the above Eq. (S53) is given by

$$\begin{aligned} \left(\frac{\delta^2 \ln \mathcal{Q}_p}{\delta \psi_{\mathbf{k}} \delta \psi_{\mathbf{k}'}} \right)_{\psi=0} &= \frac{1}{\mathcal{Q}_p[\psi = 0]} \left. \frac{\delta^2 \mathcal{Q}_p}{\delta \psi_{\mathbf{k}} \delta \psi_{\mathbf{k}'}} \right|_{\psi=0} - \frac{1}{\mathcal{Q}_p[\psi = 0]} \left. \frac{\delta \mathcal{Q}_p}{\delta \psi_{\mathbf{k}}} \right|_{\psi=0} \times \frac{1}{\mathcal{Q}_p[\psi = 0]} \left. \frac{\delta \mathcal{Q}_p}{\delta \psi_{\mathbf{k}'}} \right|_{\psi=0} \\ &= \frac{1}{\mathcal{Q}_p[\psi = 0]} \left. \frac{\delta^2 \mathcal{Q}_p}{\delta \psi_{\mathbf{k}} \delta \psi_{\mathbf{k}'}} \right|_{\psi=0} \\ &= \frac{1}{\Omega^2} \frac{\epsilon' l^3}{4\pi l_{\text{B}}} \mathbf{k} \cdot \mathbf{k}' \sum_{\tau=1}^N \left\langle e^{-i(\mathbf{k}+\mathbf{k}') \cdot \mathbf{R}_{\tau}} \right\rangle_{\psi=0} - \frac{1}{\Omega^2} \sum_{\tau, \mu=1}^N \sigma_{\tau} \sigma_{\mu} \left\langle e^{-i(\mathbf{k} \cdot \mathbf{R}_{\tau} + \mathbf{k}' \cdot \mathbf{R}_{\mu})} \right\rangle_{\psi=0}, \end{aligned} \quad (\text{S55})$$

where the second equality follows from Eq. (S54). The two \mathbf{R} -averages over Gaussian chain configurations in the above Eq. (S55) may be evaluated as follows. For $\langle e^{-i(\mathbf{k}+\mathbf{k}')\cdot\mathbf{R}_\tau} \rangle_{\psi=0}$, only a single monomer coordinate variable \mathbf{R}_τ is involved and thus it is unconstrained and \mathbf{R} -averaging entails only a single integration of \mathbf{R}_τ over the entire system volume Ω . The correspondence $\int d\mathbf{R}_\tau \leftrightarrow (\Omega/\mathcal{N}_r) \sum_{\mathbf{R}_\tau}$ yields $\langle e^{-i(\mathbf{k}+\mathbf{k}')\cdot\mathbf{R}_\tau} \rangle_{\psi=0} = \delta_{\mathbf{k},-\mathbf{k}'}$. Next, to compute $\langle e^{-i(\mathbf{k}\cdot\mathbf{R}_\tau+\mathbf{k}'\cdot\mathbf{R}_\mu)} \rangle_{\psi=0}$, we rewrite it as $\langle e^{-i\mathbf{k}\cdot(\mathbf{R}_\tau-\mathbf{R}_\mu)} e^{-i(\mathbf{k}+\mathbf{k}')\cdot\mathbf{R}_\mu} \rangle_{\psi=0}$, which indicates that the \mathbf{R} -averaging involves integrating over two monomer coordinates, one is unconstrained and the other is constrained by the Gaussian chain statistics for two points separated by a contour length $l|\tau-\mu|$. Without loss of generality, we select \mathbf{R}_μ to be the unconstrained coordinates. As for the first average, summing over \mathbf{R}_μ using the $\int d\mathbf{R}_\mu \leftrightarrow (\Omega/\mathcal{N}_r) \sum_{\mathbf{R}_\mu}$ correspondence yields the Kronecker $\delta_{\mathbf{k},-\mathbf{k}'}$. In accordance with the Gaussian statistics governed by the $3/2l^2 \sum_{\tau=1}^{N-1} (\mathbf{R}_{\tau+1}-\mathbf{R}_\tau)^2$ term of $\mathcal{H}_p[\psi, \mathbf{R}]$ in Eq. (S48), $\mathbf{R}_\tau-\mathbf{R}_\mu$ is weighted by $\exp(-3|\mathbf{R}_\tau-\mathbf{R}_\mu|^2/2l^2|\tau-\mu|)$, and therefore the \mathbf{R} -averaging of $e^{-i\mathbf{k}\cdot(\mathbf{R}_\tau-\mathbf{R}_\mu)}$ yields $\exp(-k^2l^2|\tau-\mu|/6)$. These considerations allow us to arrive at the expression

$$\left(\frac{\delta^2 \ln \mathcal{Q}_p}{\delta\psi_{\mathbf{k}}\delta\psi_{\mathbf{k}'}} \right)_{\psi=0} = -\frac{\delta_{\mathbf{k},-\mathbf{k}'}}{\Omega^2} \left[\frac{\epsilon' N l^3 k^2}{4\pi l_B} + \langle \sigma | \hat{G}_M(kl) | \sigma \rangle \right] \quad (\text{S56})$$

for Eq. (S55), where $[\hat{G}_M(kl)]_{\tau\mu} = \exp[-(kl)^2|\tau-\mu|/6]$ as defined above. Therefore, according to Eqs. (S53) and (S54), the $n_p \ln \mathcal{Q}_p[\psi]$ term in Eq. (S52) is given by

$$\begin{aligned} n_p \ln \mathcal{Q}_p[\psi] &\approx \frac{1}{2} n_p \sum_{\mathbf{k}, \mathbf{k}'} \left(\frac{\delta^2 \ln \mathcal{Q}_p}{\delta\psi_{\mathbf{k}}\delta\psi_{\mathbf{k}'}} \right)_{\psi=0} \psi_{\mathbf{k}} \psi_{\mathbf{k}'} \\ &= -\frac{n_p}{2\Omega^2} \sum_{\mathbf{k}, \mathbf{k}'} \delta_{\mathbf{k},-\mathbf{k}'} \left[\frac{\epsilon' N l^3 k^2}{4\pi l_B} + \langle \sigma | \hat{G}_M(kl) | \sigma \rangle \right] \psi_{\mathbf{k}} \psi_{\mathbf{k}'} \\ &= -\frac{1}{2\Omega} \sum_{\mathbf{k} \neq \mathbf{0}} \left[\frac{\epsilon' \phi_m k^2}{4\pi l_B} + \frac{\phi_m}{N l^3} \langle \sigma | \hat{G}_M(kl) | \sigma \rangle \right] \psi_{\mathbf{k}} \psi_{-\mathbf{k}}, \end{aligned} \quad (\text{S57})$$

where we have used the definition of polymer volume fraction $\phi_m = l^3 n_p N / \Omega$, and the fact that the $\mathbf{k} = \mathbf{0}$ terms vanishes: the first term because of the k^2 factor and the second term because of the overall neutrality of the polyampholytes, i.e., $\sum_\tau \sigma_\tau = 0$, and $[\hat{G}_M(0)]_{\tau\mu} = 1$. Combining this result with Eq. (S52), we arrive at

$$\begin{aligned} \mathcal{H}[\psi_{\mathbf{k}}] &\approx \frac{1}{2\Omega} \sum_{\mathbf{k} \neq \mathbf{0}} \left[\frac{(\epsilon_w + \epsilon' \phi_m) k^2}{4\pi l_B} + \frac{\phi_m}{N l^3} \langle \sigma | \hat{G}_M(kl) | \sigma \rangle \right] \psi_{\mathbf{k}} \psi_{-\mathbf{k}} \\ &= \frac{1}{2\Omega} \sum_{\mathbf{k} \neq \mathbf{0}} \left[\frac{\epsilon_r(\phi_m) k^2}{4\pi l_B} + \frac{\phi_m}{N l^3} \langle \sigma | \hat{G}_M(kl) | \sigma \rangle \right] \psi_{\mathbf{k}} \psi_{-\mathbf{k}}, \end{aligned} \quad (\text{S58})$$

where we have made use of the above definition of $\epsilon_r(\phi_m)$ which is linear in ϕ_m . We may now evaluate \mathcal{Z}_{el} by performing the functional integral $\prod_{\mathbf{k} \neq \mathbf{0}} \int d\psi_{\mathbf{k}}$ in Eq. (S51). Because

the $\psi_{\mathbf{k}}$ s are Fourier transformations of the real-valued field $\psi(\mathbf{r})$, $\psi_{\mathbf{k}}^* = \psi_{-\mathbf{k}}$ and $\prod_{\mathbf{k} \neq \mathbf{0}} \int d\psi_{\mathbf{k}} = \prod_{\mathbf{k} > \mathbf{0}} \int d\psi_{\mathbf{k}} \int d\psi_{\mathbf{k}}^*$, where the $\mathbf{k} > \mathbf{0}$ notation means that the product or summation excludes the origin and is over $\mathbf{k} = (k_1, k_2, k_3)$ but not $-\mathbf{k} = (-k_1, -k_2, -k_3)$. This can be effectuated by first excluding $(k_1, k_2, k_3) = (0, 0, 0)$ and then restricting the product or sum to $k_1 \geq 0$ (or to $k_2 \geq 0$ or to $k_3 \geq 0$). Expressing $\psi_{\mathbf{k}}$ in terms of its real part $\psi_{\mathbf{k}}^{\text{R}}$ and imaginary part $\psi_{\mathbf{k}}^{\text{I}}$, i.e., $\psi_{\mathbf{k}} = \psi_{\mathbf{k}}^{\text{R}} + i\psi_{\mathbf{k}}^{\text{I}}$ and $\psi_{\mathbf{k}}^* = \psi_{\mathbf{k}}^{\text{R}} - i\psi_{\mathbf{k}}^{\text{I}}$ where $\psi_{\mathbf{k}}^{\text{R}}$ and $\psi_{\mathbf{k}}^{\text{I}}$ are real numbers, one obtains $\prod_{\mathbf{k} > \mathbf{0}} \int d\psi_{\mathbf{k}} \int d\psi_{\mathbf{k}}^* = \prod_{\mathbf{k} > \mathbf{0}} 2 \int_{-\infty}^{\infty} d\psi_{\mathbf{k}}^{\text{R}} \int_{-\infty}^{\infty} d\psi_{\mathbf{k}}^{\text{I}}$. Since $\psi_{\mathbf{k}}\psi_{-\mathbf{k}} = (\psi_{\mathbf{k}}^{\text{R}})^2 + (\psi_{\mathbf{k}}^{\text{I}})^2$,

$$\begin{aligned} \mathcal{Z}_{\text{el}} &= \left\{ \prod_{\mathbf{k} > \mathbf{0}} \left(\frac{\mathcal{N}_{\mathbf{r}}}{\pi\Omega^2} \right) \left[\frac{\epsilon_{\text{r}}(\phi_m)k^2}{4\pi l_{\text{B}}} \right] \int_{-\infty}^{\infty} d\psi_{\mathbf{k}}^{\text{R}} \int_{-\infty}^{\infty} d\psi_{\mathbf{k}}^{\text{I}} \right\} \\ &\quad \times \exp \left\{ \frac{1}{\Omega} \sum_{\mathbf{k} > \mathbf{0}} \left[\frac{\epsilon_{\text{r}}(\phi_m)k^2}{4\pi l_{\text{B}}} + \frac{\phi_m}{Nl^3} \langle \sigma | \hat{G}_{\text{M}}(kl) | \sigma \rangle \right] \left[(\psi_{\mathbf{k}}^{\text{R}})^2 + (\psi_{\mathbf{k}}^{\text{I}})^2 \right] \right\} \\ &= \prod_{\mathbf{k} > \mathbf{0}} \left(\frac{\mathcal{N}_{\mathbf{r}}}{\pi\Omega^2} \right) \left[\frac{\epsilon_{\text{r}}(\phi_m)k^2}{4\pi l_{\text{B}}} \right] \times \pi\Omega \left[\frac{\epsilon_{\text{r}}(\phi_m)k^2}{4\pi l_{\text{B}}} + \frac{\phi_m}{Nl^3} \langle \sigma | \hat{G}_{\text{M}}(kl) | \sigma \rangle \right]^{-1} \\ &= \prod_{\mathbf{k} \neq \mathbf{0}} \sqrt{\frac{\mathcal{N}_{\mathbf{r}}}{\Omega}} \left[1 + \frac{4\pi l_{\text{B}}}{\epsilon_{\text{r}}(\phi_m)k^2} \frac{\phi_m}{Nl^3} \langle \sigma | \hat{G}_{\text{M}}(kl) | \sigma \rangle \right]^{-1/2}. \end{aligned} \quad (\text{S59})$$

Hence, up to an additive constant $\propto \mathcal{N}_{\mathbf{r}} \ln(\mathcal{N}_{\mathbf{r}}/\Omega)$ that does not affect configurational distribution, the electrostatic contribution to the free energy in Eq. (S27) is equal to

$$\begin{aligned} f_{\text{el}} &\equiv -\frac{l^3}{\Omega} \ln \mathcal{Z}_{\text{el}} = -\frac{l^3}{\Omega} \sum_{\mathbf{k} \neq \mathbf{0}} \ln \left[1 + \frac{4\pi l_{\text{B}}}{\epsilon_{\text{r}}(\phi_m)k^2} \frac{\phi_m}{Nl^3} \langle \sigma | \hat{G}_{\text{M}}(kl) | \sigma \rangle \right]^{-1/2} \\ &\rightarrow \frac{l^3}{2} \int \frac{d^3k}{(2\pi)^3} \ln \left[1 + \frac{4\pi l_{\text{B}}}{\epsilon_{\text{r}}(\phi_m)k^2} \frac{\phi_m}{Nl^3} \langle \sigma | \hat{G}_{\text{M}}(kl) | \sigma \rangle \right], \end{aligned} \quad (\text{S60})$$

where we have applied the correspondence

$$\frac{1}{\Omega} \sum_{\mathbf{k}} \rightarrow \int \frac{d^3k}{(2\pi)^3} \quad (\text{S61})$$

and noted that the $k \rightarrow 0$ contribution vanishes inside the integral in Eq. (S60) because $d^3k \propto k^2 dk$ and thus $\sum_{\mathbf{k} \neq \mathbf{0}}$ may be approximated by $\Omega \int d^3k / (2\pi)^3$ for this quantity. The last expression in Eq. (S60) is formally identical to the one we obtained previously by heuristically replacing the position- and ϕ_m -independent ϵ_{r} in simple RPA theory with $\epsilon_{\text{r}}(\phi_m)$ [Eq. (S14)]. This can be readily verified by setting $b = a = l$, hence $\eta = 1$ in Eqs. (S14) and (S15), and noting that $(1/2)d^3k / (2\pi)^3 = k^2 dk / 4\pi^2$, in which case the last line of Eq. (S60) is seen to be equal to Eq. (S14) with the $\mathcal{G}_1(\tilde{k})$ term [Eq. (S15a)] present but the $\mathcal{G}_2(\tilde{k})$ term [Eq. (S15b)] omitted (no subtraction of self interaction) as well as $\tilde{k}^2(1 + \tilde{k}^2) \rightarrow \tilde{k}^2$ (no short-range cutoff for Coulomb interaction).

In other words, the heuristic RPA formulas for $\epsilon_r \rightarrow \epsilon_r(\phi_m)$ in Eqs. (S14) and (S15) can be rigorously established in the context of RPA approximation provided that ϵ_r is a linear function of ϕ_m . Indeed, if ϵ_r was a more complicated function of ϕ_m , the last term in Eq. (S45) would have individual interaction terms, such as $\delta(\mathbf{R}_{\alpha,\tau} - \mathbf{R}_{\beta,\mu})$, etc., that involve different polymer chains, and that would necessitate an additional summation \sum_α over polymer chains instead of a single \sum_τ over monomers on a single chain. In that case, the subsequent simplification in terms of the single-chain partition function \mathcal{Q}_p [Eq. (S50)] and thus the RPA expansion of $\ln \mathcal{Q}_p$ [Eq. (S53)] cannot proceed in the manner described above. Therefore, it remains unclear whether Eq. (S60) holds in general for $\epsilon_r(\phi_m)$ that is not linear in ϕ_m .

In our previous applications, we considered a Coulomb potential with a physical short-range cutoff by the modification

$$\mathcal{U}(\mathbf{r}, \mathbf{r}') = \frac{l_B}{\epsilon_r |\mathbf{r} - \mathbf{r}'|} \rightarrow \mathcal{U}(\mathbf{r}, \mathbf{r}') = \frac{l_B}{\epsilon_r |\mathbf{r} - \mathbf{r}'|} \left(1 - e^{-|\mathbf{r} - \mathbf{r}'|/l} \right) \quad (\text{S62})$$

[cf. Eq. (6) of Ref. 34; Eq. (34) of Ref. 35], which for constant, position-independent ϵ_r results in a f_{el} with $1/k^2$ replaced by $1/[k^2(1+k^2)]$. In the context of a general position-dependent ϵ_r , this feature can in principle be accounted for by introducing an $\epsilon_r(|\mathbf{r} - \mathbf{r}'|)$, but the necessary formalism has not been developed. In the present work, we incorporate this feature by simply replacing the $1/k^2$ factor by $1/[k^2(1+k^2)]$ in Eq. (S60) so as to capture this physical property as much as possible and place our present results on an essentially equal footing with our earlier results for position-independent ϵ_r . Mathematically, this procedure may be viewed as a regularization for “ultraviolet” large- k (i.e., small- $|\mathbf{r} - \mathbf{r}'|$) divergence. As such, it does serve to impart a physical short-spatial-range cutoff, though it may not correspond exactly to any particularly modified form of f_{el} in Eq. (S62) that is applicable to a general position-dependent $\epsilon_r(\mathbf{r})$.

Taking all of the above into consideration, we use the general formula in Eqs. (S14) and (S15) above (which allows for $a \neq b = l$ and thus $\eta = (b/a)^3 \neq 1$ and $r_m \neq 1$) for comparing RPA theory against explicit-chain simulation, with the understanding that ϵ_r must be a linear function of polymer volume fraction $\phi = r_m \phi_m$. Following previous practice,^{34,35} the electrostatic self-interaction term $\mathcal{G}_2(\tilde{k}) = 4\pi l_B \phi_m / [k^2(1+k^2b^2)\epsilon_r(\phi_m) N b^3] \sum_{\tau=1}^N |\sigma_\tau|$ is subtracted in Eq. (S14). In the context of a position-dependent $\epsilon_r(\mathbf{r})$, however, we recognize that this term can be physically significant for capturing the polyampholyte chains’ varying preference for different dielectric environments.¹⁰⁰ Hence we consider also an electrostatic free energy

$$f_{\text{el}}^{[\text{self}]} \equiv \int \frac{d\tilde{k} \tilde{k}^2}{4\pi^2 \eta} \ln \left[1 + \eta \mathcal{G}_1(\tilde{k}) \right] = a^3 \int \frac{dk k^2}{4\pi^2} \ln \left[1 + \frac{b^3}{a^3} \mathcal{G}_1(kb) \right] \quad (\text{S63})$$

that includes (does not subtract) electrostatic self-interaction, and use both Eq. (S14) and

Eq. (S63) in our comparison of analytical theory with chain simulation.

UNIT CONVERSION FOR COMPARISON WITH EXPLICIT-CHAIN SIMULATIONS

The theory-predicted phase diagrams (coexistence curves) in Fig. S7 of the Supporting Information for position- and IDR concentration-independent ϵ_r are computed numerically using the RPA+FH model described in Ref. 35. Specifically, translational and mixing entropy is given by Eqs. (13) and (14), the RPA formula for f_{el} is provided by Eqs. (39) and (40), and the augmented FH term is the one in Eq. (61) of this reference. Values of the parameters in these formulas are adapted to the present application, as follows:

- a : Unit length of the model. We set the unit volume, a^3 , to be that of the volume occupied by a water molecule in pure water, i.e., $\phi_w^{\text{pure}} = \rho_w^{\text{pure}} \times a^3 = 1$, where the number density of pure water $\rho_w^{\text{pure}} = 10^6 \text{ g m}^{-3} N_A / 18.01528 \text{ g}$ where 10^6 g m^{-3} is density of water, $N_A = 6.02214086 \times 10^{23}$ is Avogadro's constant and 18.01528 g is molar mass of water. Thus, $a = (1/\rho_w^{\text{pure}})^{1/3} = 3.104 \text{ \AA} = 3.104 \times 10^{-10} \text{ m}$.
- b : The C_α - C_α virtual bond length of polypeptides $b = l = 3.8 \text{ \AA} = 3.8 \times 10^{-10} \text{ m}$.
- η [in Eq. (39) of Ref. 35]: From the above values for a and b , $\eta = (b/a)^3 = (3.8/3.104)^3 = 1.835$.
- r_m (monomer size factor in Eq. (14) of Ref. 35): The r_m ratio between the size of one amino acid residue in Ddx4 IDR and the unit volume a^3 is obtained as follows. Because the density of pure protein = $1,587 \text{ mg ml}^{-1}$, number of amino acid residues (monomers) in Ddx4 IDR is $N = 241$, and the molar mass of Ddx4 IDR is $25,833$ (Ref. 65), the monomer (amino acid residue) number density of pure protein is given by

$$\rho_m^{\text{pure}} = (1.587 \times 10^6) \text{ g m}^{-3} \times 241 \times N_A / 25,833 \text{ g} . \quad (\text{S64})$$

Since the volume fraction ϕ of pure protein is unity by definition, i.e., $\phi = \rho_m \times r_m \times a^3$, it follows that

$$r_m = (a^3 \rho_m^{\text{pure}})^{-1} = \rho_w^{\text{pure}} / \rho_m^{\text{pure}} = \frac{25833}{18.0} \cdot \frac{1}{1.587} \cdot \frac{1}{241} = 3.752 . \quad (\text{S65})$$

- r_s and r_c [size factors for salt and counterions, respectively, in Eq. (14) of Ref. 35]: Both r_s and r_c are set to 1.

The conversion between the $\phi_m = n_p N a^3 / \Omega$ in analytical theory to Ddx4 concentration, [Ddx4], in units of mg/ml (mg ml^{-1}), is given by

$$\phi_m = \left\{ [\text{Ddx4}(\text{mg/ml})] \times 1000 \text{ g/mg} \times 236 / (\text{Ddx4 molar mass in g}) \right\} \times N_A \times a^3 , \quad (\text{S66})$$

where $N = 236$ is the chain length of the Ddx4 IDRs, (Ddx4 molar mass in g) of the four Ddx4 IDR sequences are 25412.48, 25412.48, 24346.80, and 24740.48, respectively, for WT, CS, FtoA, and RtoK.⁶⁵ It should be noted that there is a slight mismatch in the lengths of Ddx4 IDRs (236 vs 241) because a Ddx4^{N1} sequence with six amino acids added to its C-terminus as a tag was used in experiments.^{4,65} Nonetheless, $N = 236$ is adopted in Eq. (S66) because the $N = 236$ sequence published in Ref. 4 is used in our simulations. In the context of our approximate analytical theory and coarse-grained chain model, the numerical difference between using $N = 236$ and $N = 241$ is not expected to be significant.

The mean-field Flory-Huggins (FH) χ parameters of non-electrostatic interactions for the four Ddx4 IDR sequences are obtained from averaging the KH potential energies $\epsilon_{ij}(r_0)$ ($= E_{ij}(r_0)$ [KH] in Fig. 1a of main text) for a given sequence (seq) over all i, j pairs of sequence positions except those entailing a charge-charge interaction [i.e., RR (Arg-Arg), RK (Arg-Lys), RD (Arg-Asp), RE (Arg-Glu), KK (Lys-Lys), KD (Lys-Asp), KE (Lys-Glu), DD (Asp-Asp), DE (Asp-Glu), EE (Glu-Glu); see main-text], yielding $\langle E \rangle_{\text{KH,seq}} = -0.1047, -0.1047, -0.0689, \text{ and } -0.0924 \text{ kcal mol}^{-1}$, respectively, for seq = WT, CS, FtoA, and RtoK. These average sequence-dependent mean-field non-electrostatic interaction energies $\langle E \rangle_{\text{KH,seq}}$ s are converted to the FH $\chi = \epsilon_h/T^*$ in Eq. (61) of Ref. 35 as follows:

1. Convert per-mole units to per-interaction units:

$$\begin{aligned} & \langle E \rangle_{\text{KH,seq}}[(\text{J/amino acid pair})] \\ &= \left\{ \langle E \rangle_{\text{KH,seq}}[(\text{kcal/mole of amino acid pairs})]/N_A \right\} \times 1000 \text{ cal/kcal} \times 4.18 \text{ J/cal} . \end{aligned} \quad (\text{S67})$$

2. Convert to the reduced variables used in analytical theory:

$$(z/2) \times \langle E \rangle_{\text{KH,seq}}[(\text{J/amino acid pair})]/(k_B T) = -\epsilon_h/T^* , \quad (\text{S68})$$

where T^* is the reduced temperature given by Eq. (38) in Ref. 35 (see below) and z is an FH geometric factor representing the maximal number of monomers (amino acid residues) that are spatial nearest neighbors to a given monomer; e.g., $z = 6$ for three-dimensional simple cubic lattices. We obtain $z/2 = 4.3$ by fitting our RPA+FH predictions to our explicit-chain simulation results.

3. Convert absolute temperature T in K to the reduced temperature T^* :

$$\frac{1}{T^*} = \frac{e^2}{4\pi\epsilon_0\epsilon_r k_B b T} , \quad (\text{S69})$$

where the electronic charge $e = 1.6 \times 10^{-19} \text{ C}$, $\epsilon_0 = 8.854 \times 10^{-12} \text{ C V}^{-1}\text{m}^{-1}$, $b = 3.8 \times 10^{-10} \text{ m}$, and $\epsilon_r = 80, 40, \text{ or } 20$ in accordance with the corresponding

simulations with position- and IDR concentration-independent relative permittivities. Note that $T^* = \epsilon_r T_0^*$ where T_0^* is defined after Eq. (S15) above and in Eq. (67) of Ref. 35.

4. Convert $\langle E \rangle_{\text{KH,seq}}$ to FH ε_h :

Based on the above consideration,

$$\begin{aligned}
\varepsilon_h &= -T^* \left(\frac{z}{2} \right) \frac{\langle E \rangle_{\text{KH,seq}}[(\text{J/amino acid pair})]}{k_B T} \\
&= - \left(\frac{4\pi\epsilon_0\epsilon_r b}{e^2} \right) \left(\frac{z}{2} \right) \times \left\{ \langle E \rangle_{\text{KH,seq}}[(\text{kcal/mole of amino acid pairs})]/N_A \right\} \\
&\quad \times 1000 \text{ cal/kcal} \times 4.18 \text{ J/cal} \\
&= - \frac{4\pi \times (8.854 \times 10^{-12}) \times (3.8 \times 10^{-10})}{(1.6 \times 10^{-19})^2} \frac{4.3 \times 1000 \times 4.18}{(6.02214086 \times 10^{23})} \\
&\quad \times \epsilon_r \langle E \rangle_{\text{KH,seq}}[(\text{kcal/mole of amino acid pairs})] \\
&= -0.04929 \times \epsilon_r \times \langle E \rangle_{\text{KH,seq}}[(\text{kcal/mole of amino acid pairs})] .
\end{aligned} \tag{S70}$$

Accordingly, the ε_h values for WT, CS, FtoA, and RtoK Ddx4 IDRs are, respectively, $\varepsilon_h = 0.413, 0.413, 0.272,$ and 0.364 when $\epsilon_r = 80$; $\varepsilon_h = 0.206, 0.206, 0.136,$ and 0.182 when $\epsilon_r = 40$; and $\varepsilon_h = 0.103, 0.103, 0.068,$ and 0.091 when $\epsilon_r = 20$.

Note that ε_h decreases with decreasing ϵ_r because the reduced temperature T^* in Eq. (S69) is proportional to ϵ_r . In this formulation using T^* , the result of decreasing ϵ_r is a reduction in the strength of favorable FH interactions relative to that of the electrostatic interactions, which is equivalent to the physical situation (with temperature measured in K) of enhanced electrostatic interactions under a reduced ϵ_r while keeping the non-electrostatic interactions unchanged.

SI Figures

WT:

MGDEDWEAEINPHMSSYVPIFEKDRYSGENGDNFNRTPASSEMDDGPSR
 RDHFMKSGFASGRNFGNRDAGECNKRDNTSTMGGFGVGKSFGNRGSNSR
 FEDGDSSGFWRSSNDCEDNPTNRGFSKRGGYRDGNNSEASGPYRRGGR
 GSFRCRGGFGLGSPNNDLPDECMQRTGGLFGSRRPVLSGTGNGDTSQS
 RSGSGSERGGYKGLNEEVITGSGKNSWKSEAEGGES

CS:

MGDRDWRAEINPHMSSYVPIFEKDRYSGENGRNFDTPASSEMMDGPSE
 RDHFMKSGFASGDNFGNRDAGKCNERNRNTSTMGGFGVGKSFNEGFSNSR
 FERGDSSGFWRSSNDCRDNPTNRDGFSDRGGYEKGNNSEASGPYERGGR
 GSFDCRGGFGLGSPNNRLDPRECMQRTGGLFGSDRPVLSGTGNGDTSQS
 RSGSGSERGGYKGLNEKVTGSGENSWKSEARGGES

FtoA:

MGDEDWEAEINPHMSSYVPIAEKDRYSGENGDNANRTPASSEMDDGPSR
 RDHAMKSGAASGRNAGNRDAGECNKRDNTSTMGGAGVGKSAGNRGASNSR
 AEDGDSSGAWRESSNDCEDNPTNRGASKRGGYRDGNNSEASGPYRRGGR
 GSARGCRGGAAGLGSPNNDLPDECMQRTGGLAGSRRPVLSGTGNGDTSQS
 RSGSGSERGGYKGLNEEVITGSGKNSWKSEAEGGES

RtoK:

MGDEDWEAEINPHMSSYVPIFEKDKYSGENGDNFNKTPASSEMDDGPSK
 KDHFMKSGFASGKNFGNKDAGECNKKDNTSTMGGFGVGKSFGNKGFNSNK
 FEDGDSSGFWKESSNDCEDNPTKNKGFSSKGGYKDGNNEASGPYKKGK
 GSFKGCKGGFGLGSPNNDLPDECMQKTGGLFGSKKPVLSGTGNGDTSQS
 KSGSGSEKGGYKGLNEEVITGSGKNSWKSEAEGGES

Fig. S1: The amino acid sequences (residues given by one-letter code) of the 236-residue Ddx4 IDR (wildtype, WT) and its charge scrambled (CS) variant (introduced by Nott et al.⁴), phenylalanine-to-alanine variant (FtoA) (corresponds to the 14FtoA in Brady et al.⁶⁵ and Vernon et al.⁶⁸) and arginine-to-lysine (RtoK) variant⁶⁸ considered in the present study. Residues of amino acids A, D, E, F, K, and R are shown in the same colors as those in Fig. 3a of the main text. Other residues, including Y which is considered in subsequent simulations, are shown in black.

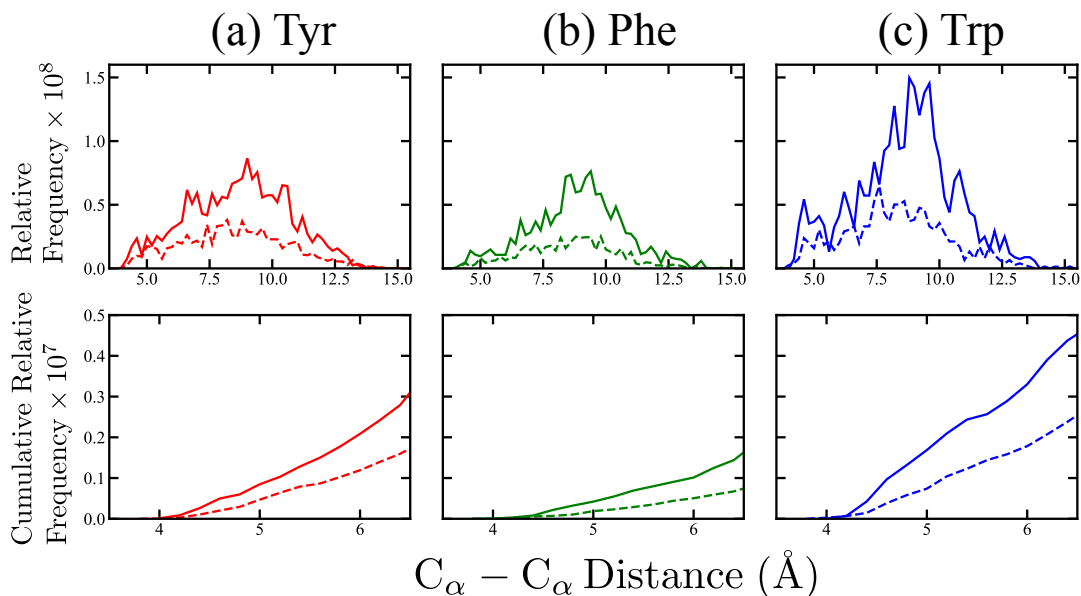


Fig. S2: Statistics of cation- π -like contacts. Distributions of C_{α} - C_{α} distance between a positively charged residue [arginine (solid curve) or lysine (dashed curve)] and an aromatic residue [tyrosine (a), phenylalanine (b), or tryptophan (c)] are obtained from the same dataset of 6,943 high-resolution X-ray structures (from a non-redundant set⁶⁸) used in Fig. 2 of the main text. The bin size for C_{α} - C_{α} distance and the color code for different residue pairs are also identical to those in Fig. 2 of the main text. For a given residue pair [Arg-Tyr, Lys-Tyr (a); Arg-Phe, Lys-Phe (b); or Arg-Trp, Lys-Trp (c)], the relative frequency of a given C_{α} - C_{α} distance bin is the total number of instances in the dataset in which the C_{α} - C_{α} distance between the given pair of residues falls within the bin, normalized (divided) by the product of the two total numbers of residues in the dataset for the two residues making up the pair. Cumulative relative frequency at a given distance is the sum of relative frequencies for distances lower or equal to the given distance. Here, cumulative relative frequencies are reported up to C_{α} - C_{α} distance of 6.5 Å, which is illustrative of common criteria for a residue-residue contact. The plotted distributions show clearly that arginine-aromatic contacts are consistently and significantly more numerous than lysine-aromatic contacts when compared on the same footing, suggesting strongly that the overall arginine-aromatic interactions are energetically more favorable than the overall lysine-aromatic interactions.⁷⁴

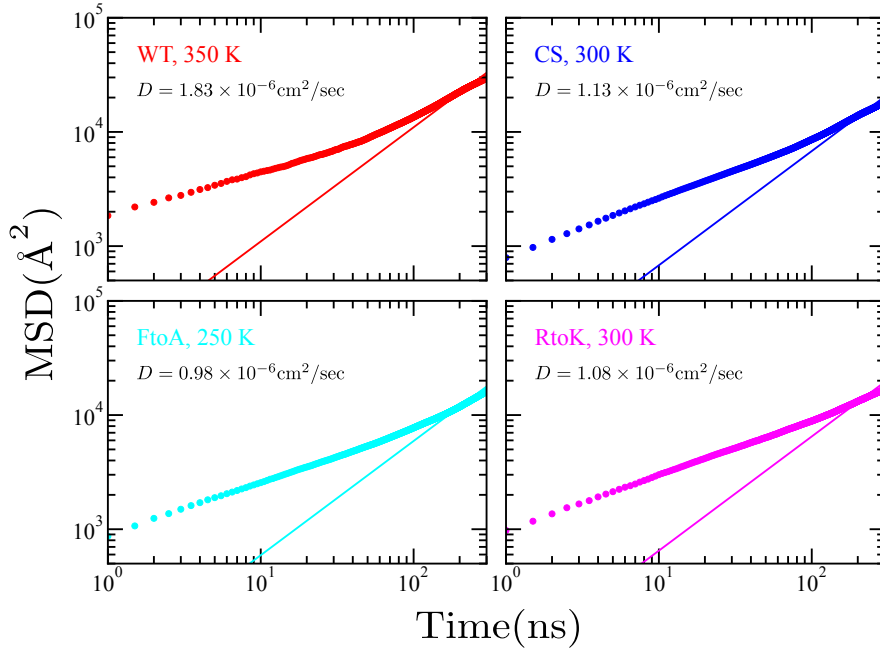


Fig. S3: Verification of liquid-like dynamics of simulated condensed phases. As in Dignon et al.,⁵² a relevant time-dependent mean-square deviation $\text{MSD}(t)$ of molecular coordinates was simulated to provide evidence for liquid-like behavior in our model systems, viz.,¹³⁵

$$\text{MSD}(t) = \frac{1}{n} \left\langle \sum_{\mu=1}^n \left| [\mathbf{r}_{\mu,\text{CM}}(t+t_0) - \mathbf{r}_{\text{CM}}(t+t_0)] - [\mathbf{r}_{\mu,\text{CM}}(t_0) - \mathbf{r}_{\text{CM}}(t_0)] \right|^2 \right\rangle_{t_0},$$

where $\mu = 1, 2, \dots, n$ labels the model IDR chains, n is the total number of IDR chains in the simulation system, $\mathbf{r}_{\mu,\text{CM}} = \sum_{i=1}^N m_i \mathbf{r}_{\mu i} / \sum_{i=1}^N m_i$ is the center-of-mass position of the μ th chain, with m_i being the mass of the i th bead (residue) along an IDR chain, $\mathbf{r}_{\text{CM}} = \sum_{\mu=1}^n \mathbf{r}_{\mu,\text{CM}} / n$ is the center-of-mass of the entire collection of n chains, and the average is over the initial time point t_0 . By subtracting drifts in molecular coordinates arising solely from the diffusion of the entire system's center of mass (see Fig. S4), the above-defined $\text{MSD}(t)$ values, which are provided by the circles in the plots, are a useful measure of the liquidity of our simulated system. Diffusion coefficients, $D = \{\lim_{t \rightarrow \infty} d[\text{MSD}(t)]/dt\}/6$, were then estimated, as indicated by the fitted straight line in each plot. Shown examples for the four Ddx4 IDR variants were simulated using the KH model with relative permittivity $\epsilon_r = 40$ at the indicated temperatures, each of which is lower than the respective system's critical temperature. The magnitudes of our simulated D s are similar to those simulated by Dignon et al. for their model FUS systems (Fig. S12 of Ref. 52). Note that our simulated D s for the model Ddx4 IDR systems are, not unexpectedly, approximately three orders of magnitude higher than the corresponding experimental values⁶⁵ because a unphysically low friction coefficient was necessitated in our Langevin dynamics simulations in order to accelerate sampling and also because a coarse-grained representation of the IDRs was used.

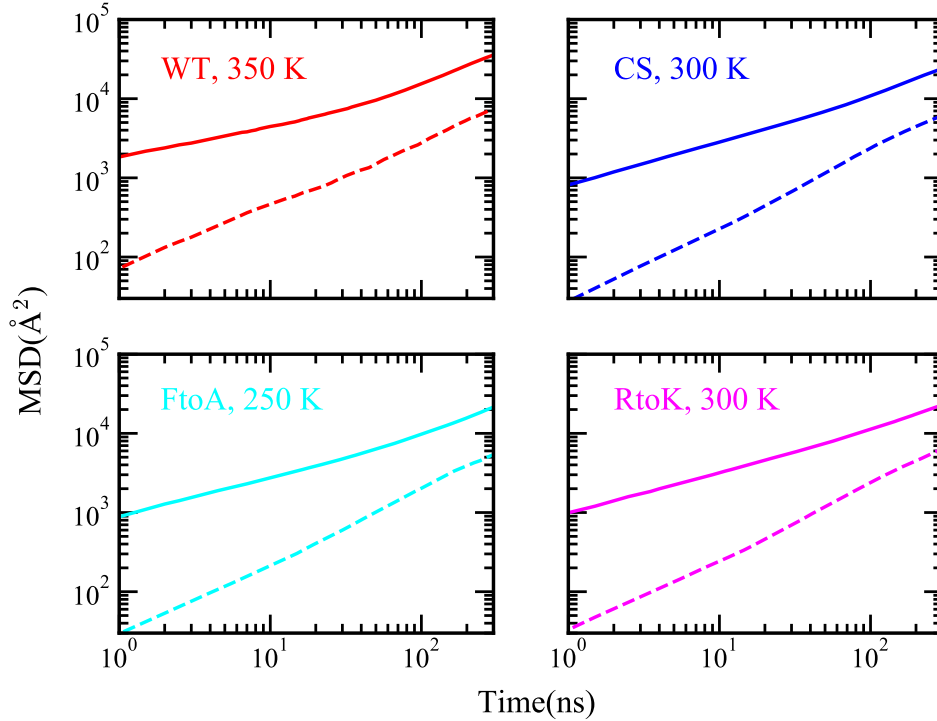


Fig. S4: Center-of-mass diffusion of the simulated Ddx4 IDR systems. Data are from the same systems as those in Fig. S3. The solid curves provide the mean-square deviation of the center-of-mass positions of the IDRs *without* subtracting the the center-of-mass position of the entire system, in which case

$$\text{MSD}(t) = \frac{1}{n} \left\langle \sum_{\mu=1}^n \left| \mathbf{r}_{\mu, \text{CM}}(t + t_0) - \mathbf{r}_{\mu, \text{CM}}(t_0) \right|^2 \right\rangle_{t_0},$$

whereas the dashed curves represent the diffusion of the center of mass of the entire system of n IDRs, given by $\text{MSD}(t) = \langle |\mathbf{r}_{\text{CM}}(t + t_0) - \mathbf{r}_{\text{CM}}(t_0)|^2 \rangle_{t_0}$. Echoing the findings in Fig. S3, a comparison of the solid and dashed curves in the present figure indicates that there is significant diffusion of individual IDRs relative to the center of mass of the entire collection of IDR chains.

LAF-1 RGG WT:

MESNQSNNNGG SGNAALNRGG RYVPPHLRGG DGGAAAAASA GGDDRRGGAG
 GGGYRRGGGN SGGGGGGGYD RGYNDNRDDR DNRRGGSGGYG RDRNYEDRGY
 NGGGGGGGNR GYNNNRGGGG GGYNRQDRGD GGSSNFSRGG YNNRDEGSDN
 RGSGRSYNND RRDNGGDGLE HHHHHH

LAF-1 RGG RtoK:

MESNQSNNNGG SGNAALNKGK KYVPPHLKGG DGGAAAAASA GGDDKKGGAG
 GGGYKKGGGN SGGGGGGGYD KGYNDNKDDK DNKGGSGGYG KDKNYEDKGY
 NGGGGGGGNK GYNNNKGGGG GGYNKQDKGD GGSSNFSKGG YNNKDEGSDN
 KGSGKSYNND KKDNGGDGLE HHHHHH

LAF-1 RGG YtoF:

MESNQSNNNGG SGNAALNRGG RFVPPHLRGG DGGAAAAASA GGDDRRGGAG
 GGGFRRGGGN SGGGGGGGFD RGFNDNRDDR DNRRGGSGGFG RDRNFEDRGF
 NGGGGGGGNR GFNNNRGGGG GGFNRQDRGD GGSSNFSRGG FNNRDEGSDN
 RGSGRSFNND RRDNGGDGLE HHHHHH

Fig. S5: LAF-1 IDR sequences simulated in Fig. 6 of the main text. Amino acid residues are given by one-letter code. The 176-residue LAF-1 RGG WT sequence and its RtoK and YtoF mutants (all with a polyhistidine tag) are the same as those used for in-vitro studies and given in the Supporting Information of Ref. 77. Underscoring the substitution positions considered in our simulations, K, F, R, and Y residues are shown, respectively, in cyan, magenta, blue, and pink, as in Fig. 6a of the main text. Other residues, including A, D, and E which are highlighted in Fig. 3a and Fig. S1 for Ddx4 IDRs, are shown here in black.

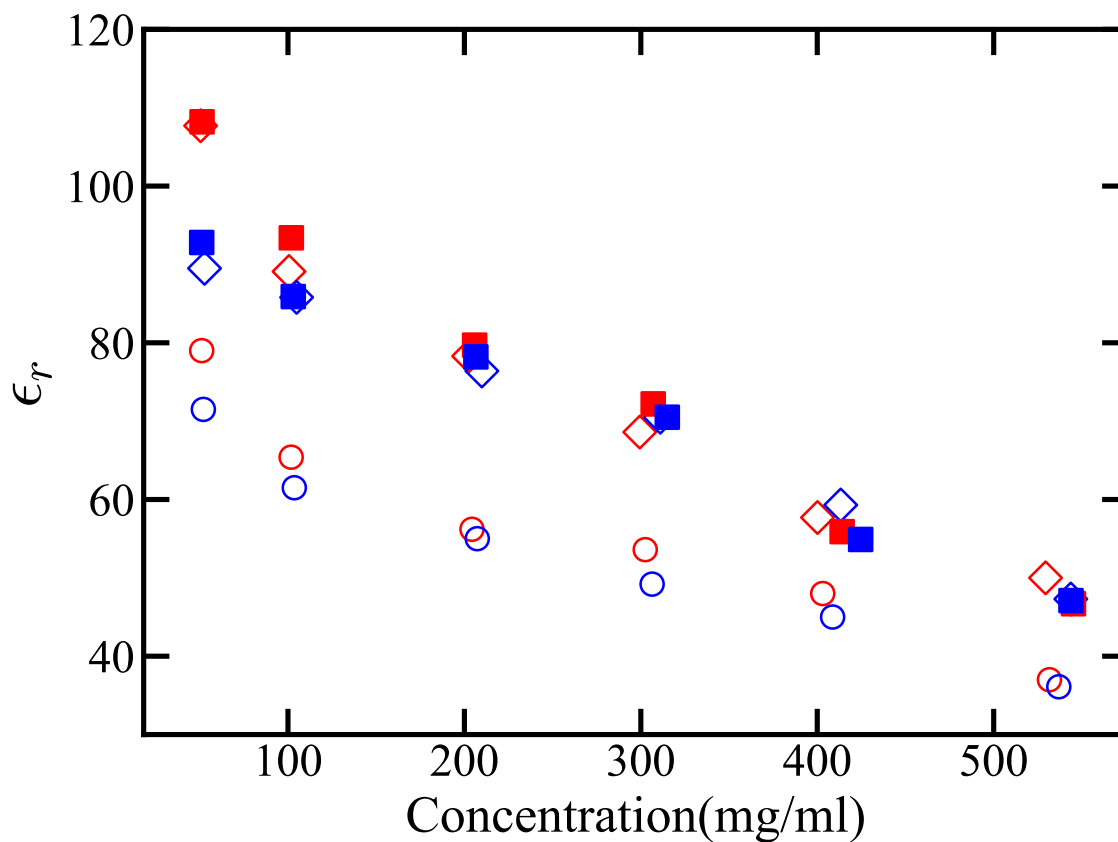


Fig. S6: Simulated IDR-concentration-dependent relative permittivity. Shown results—part of which are also provided in Fig. 7a of the main text—are for the WT Ddx4 IDR. Simulations were conducted using the SPC/E water model with 100 mM NaCl (circles), the TIP3P water model without salt (squares), and the TIP3P model with 100 mM NaCl (diamonds). Red symbols represent ϵ_r values simulated using the full force field, whereas blue symbols denote ϵ_r values simulated while the electric charges on the sidechains of arginine, lysine, glutamic acid, and aspartic acid are artificially turned off. The ϵ_r values plotted here are tabulated in Table S1.

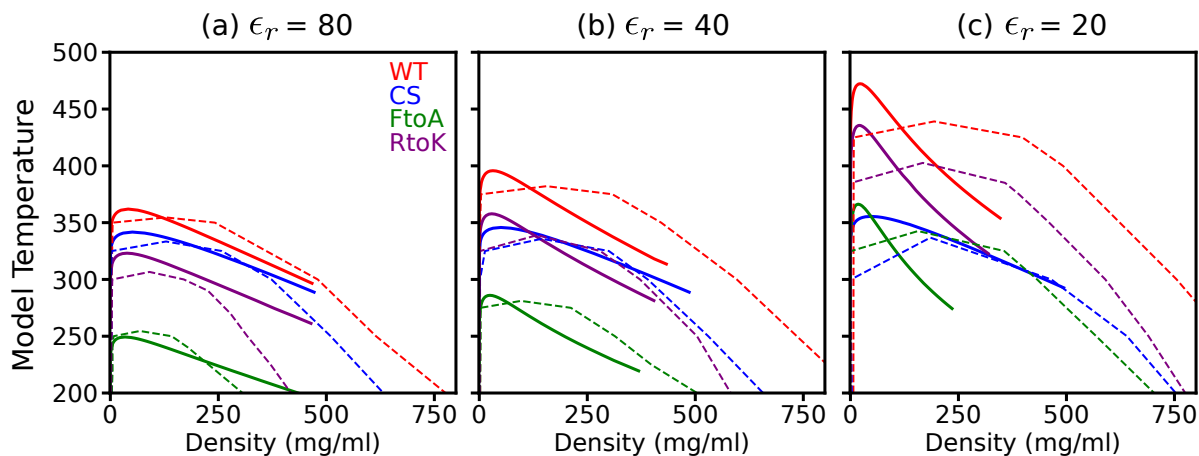


Fig. S7: Comparing analytical theory with simulation for sequence-dependent liquid-liquid phase separation of model Ddx4 systems. Phase diagrams simulated using the explicit-chain KH model under different permittivities (ϵ_r) for the four Ddx4 IDRs from Fig. 4 of the main text are replotted here as dashed curves. Predicted phase diagrams by the RPA+FH theory that afford the best overall fit, at $z/2 = 4.3$, are shown as solid curves.

SI Table

Table S1: IDR-concentration-dependent relative permittivity, ϵ_r , simulated for WT Ddx4 IDR using the SPC/E and TIP3P atomic models of water at $T = 300$ K.

SPC/E + salt ^b		TIP3P, no salt		TIP3P + salt ^b	
[Ddx4] ^a	ϵ_r	[Ddx4] ^a	ϵ_r	[Ddx4] ^a	ϵ_r
51.1 (52.04)	79.0 (71.5)	51.3 (51.1)	108.2 (92.8)	50.5 (52.7)	107.7 (89.5)
101.8 (103.6)	65.4 (61.5)	101.9 (103.0)	93.4 (85.9)	100.6 (104.9)	89.1 (85.8)
204.3 (207.3)	56.2 (55.0)	205.8 (206.5)	79.7 (78.2)	202.4 (209.9)	78.3 (76.4)
302.5 (306.4)	53.6 (49.2)	307.0 (315.0)	72.2 (70.5)	299.4 (311.0)	68.6 (70.5)
403.1 (408.7)	48.0 (45.0)	414.1 (424.6)	55.9 (54.9)	400.1 (413.3)	57.7 (59.3)
531.6 (536.9)	37.0 (36.1)	545.2 (543.8)	46.7 (47.1)	529.4 (543.7)	50.0 (47.3)

^a Concentrations (in mg ml⁻¹) and simulated ϵ_r values given in bold font are for systems that apply the full force field; those given in ordinary roman (non-bold) font and in parentheses are for systems in which the electric charges on the sidechains of arginine, lysine, glutamic acid, and aspartic acid of WT Ddx4 IDR are artificially turned off.

^b [NaCl] = 100 mM.

References

- ¹ C. P. Brangwynne, C. R. Eckmann, D. S. Courson, A. Rybarska, C. Hoege, J. Gharakhani, F. Jülicher, A. A. Hyman, Germline P granules are liquid droplets that localize by controlled dissolution/condensation. *Science* **324**, 1729–1732 (2009).
- ² P. Li, S. Banjade, H.-C. Cheng, S. Kim, B. Chen, L. Guo, M. Llaguno, J. V. Hollingsworth, D. S. King, S. F. Banani, P. S. Russo, Q.-X. Jiang, B. T. Nixon, M. K. Rosen, Phase transitions in the assembly of multivalent signalling proteins. *Nature* **483**, 336–340 (2012).
- ³ M. Kato, T. W. Han, S. Xie, K. Shi, X. Du, L. C. Wu, H. Mirzaei, E. J. Goldsmith, J. Longgood, J. Pei, N. V. Grishin, D. E. Frantz, J. W. Schneider, S. Chen, L. Li, M. R. Sawaya, D. Eisenberg, R. Tycko, S. L. McKnight, Cell-free formation of RNA granules: low complexity sequence domains form dynamic fibers within hydrogels. *Cell* **149**, 753–767 (2012).
- ⁴ T. J. Nott, E. Petsalaki, P. Farber, D. Jarvis, E. Fussner, A. Plochowietz, T. D. Craggs, D. P. Bazett-Jones, T. Pawson, J. D. Forman-Kay, A. J. Baldwin, Phase transition of a disordered nuage protein generates environmentally responsive membraneless organelles. *Mol. Cell* **57**, 936–947 (2015).
- ⁵ A. Molliex, J. Temirov, J. Lee, M. Coughlin, A. P. Kanagaraj, H. J. Kim, T. Mittag, J. P. Taylor, Phase separation by low complexity domains promotes stress granule assembly and drives pathological fibrillization. *Cell* **163**, 123–133 (2015).
- ⁶ Y. Lin, D. S. W. Protter, M. K. Rosen, R. Parker, Formation and maturation of phase-separated liquid droplets by RNA-binding proteins. *Mol. Cell* **60**, 208–219 (2015).
- ⁷ M. Zeng, X. Chen, D. Guan, J. Xu, H. Wu, P. Tong, M. Zhang, Reconstituted post-synaptic density as a molecular platform for understanding synapse formation and plasticity. *Cell* **174**, 1172–1187 (2018).
- ⁸ L. D. Muiznieks, S. Sharpe, R. Pomès, F. W. Keeley, Role of liquid-liquid phase separation in assembly of elastin and other extracellular matrix proteins. *J. Mol. Biol.* **430**, 4741–4753 (2018).
- ⁹ N. B. Nedelsky, J. P. Taylor, Bridging biophysics and neurology: Aberrant phase transitions in neurodegenerative disease. *Nat. Rev. Neurol.* **15**, 272–286 (2019).

- ¹⁰ S. F. Banani, H. O. Lee, A. A. Hyman, M. K. Rosen, Biomolecular condensates: organizers of cellular biochemistry. *Nat. Rev. Mol. Cell Biol.* **18**, 285–298 (2017).
- ¹¹ E. Gomes, J. Shorter, The molecular language of membraneless organelles. *J. Biol. Chem.* **294**, 7115–7127 (2019).
- ¹² R. J. Stewart, C. S. Wang, I. T. Song, J. P. Jones, The role of coacervation and phase transitions in the sandcastle worm adhesive system *Adv. Colloid Interf. Sci.* **239**, 88–96 (2017).
- ¹³ X. Chen, X. Wu, H. Wu, M. Zhang, Phase separation at the synapse. *Nat. Neurosci.* **23**, 301–310 (2020).
- ¹⁴ B. A. Gibson, L. K. Doolittle, M. W. G. Schneider, L. E. Jensen, N. Gamarra, L. Henry, D. W. Gerlich, S. Redding, M. K. Rosen, Organization of chromatin by intrinsic and regulated phase separation. *Cell* **179**, 470–484 (2019).
- ¹⁵ B. Tsang, J. Arsenault, R. M. Vernon, H. Lin, N. Sonenberg, L. Y. Wang, A. Bah, J. D. Forman-Kay, Phosphoregulated FMRP phase separation models activity-dependent translation through bidirectional control of mRNA granule formation. *Proc. Natl. Acad. Sci. U.S.A.* **116**, 4218–4227 (2019).
- ¹⁶ T. H. Kim, B. Tsang, R. M. Vernon, N. Sonenberg, L. E. Kay, J. D. Forman-Kay, Phospho-dependent phase separation of FMRP and CAPRIN1 recapitulates regulation of translation and deadenylation. *Science* **365**, 825–829 (2019).
- ¹⁷ L. E. Wong, A. Bhatt, P. S. Erdmann, Z. Hou, J. Maier, S. Pirkuliyeva, M. Engelke, S. Becker, J. Plitzko, J. Wienands, C. Griesinger, Tripartite phase separation of two signal effectors with vesicles priming B cell responsiveness. *Nat. Comm.* **11**, 848 (2020).
- ¹⁸ Y. Fujioka, J. M. Alam, D. Noshiro, K. Mouri, T. Ando, Y. Okada, A. I. May, R. L. Knorr, K. Suzuki, Y. Ohsumi, N. N. Noda, Phase separation organizes the site of autophagosome formation. *Nature* **578**, 301–305 (2020).
- ¹⁹ Y. Shin, C. P. Brangwynne, Liquid phase condensation in cell physiology and disease. *Science* **357**, eaaf4382 (2017).
- ²⁰ Y.-H. Lin, J. D. Forman-Kay, H. S. Chan, Theories for sequence-dependent phase behaviors of biomolecular condensates. *Biochemistry* **57**, 2499–2508 (2018).
- ²¹ S. Boeynaems, S. Alberti, N. L. Fawzi, T. Mittag, M. Polymenidou, F. Rousseau, J. Schymkowitz, J. Shorter, B. Wolozin, L. Van Den Bosch, P. Tompa, M. Fuxreiter, Protein phase separation: a new phase in cell biology. *Trends Cell Biol.* **28**, 420–435 (2018).

- ²² R. M. Vernon, J. D. Forman-Kay, First-generation predictors of biological protein phase separation. *Curr. Opin. Struct. Biol.* **58**, 88–96 (2019).
- ²³ K. M. Ruff, R. V. Pappu, A. S. Holehouse, Conformational preferences and phase behavior of intrinsically disordered low complexity sequences: insights from multiscale simulations. *Curr. Opin. Struct. Biol.* **56**, 1–10 (2019).
- ²⁴ S. L. Perry, Phase separation: Bridging polymer physics and biology. *Curr. Opin. Colloid Interface Sci.* **39**, 86–97 (2019).
- ²⁵ G. L. Dignon, W. Zheng, J. Mittal, Simulation methods for liquid-liquid phase separation of disordered proteins. *Curr. Opin. Chem. Eng.* **23**, 92–98 (2019).
- ²⁶ S. Alberti, A. Gladfelter, T. Mittag, Considerations and challenges in studying liquid-liquid phase separation and biomolecular condensates. *Cell* **176**, 419–434 (2019).
- ²⁷ H. Cinar, Z. Fetahaj, S. Cinar, R. M. Vernon, H. S. Chan, R. Winter, Temperature, hydrostatic pressure, and osmolyte effects on liquid-liquid phase separation in protein condensates: Physical chemistry and biological implications. *Chem. Eur. J.* **25**, 13049–13069 (2019).
- ²⁸ J.-M. Choi, A. S. Holehouse, R. V. Pappu, Physical principles underlying the complex biology of intracellular phase transitions. *Annu. Rev. Biophys.* **49**, 107–133 (2020).
- ²⁹ P. A. Chong, J. D. Forman-Kay, Liquid-liquid phase separation in cellular signaling systems. *Curr. Opin. Struct. Biol.* **41**, 180–186 (2016).
- ³⁰ X.-H. Li, P. L. Chavali, R. Pancsa, S. Chavali, M. M. Babu, Function and regulation of phase-separated biological condensates. *Biochemistry* **57**, 2452–2461 (2018).
- ³¹ C. F. Lee, J. D. Wurtz, Novel physics arising from phase transitions in biology. *J. Phys. D: Appl. Phys.* **52**, 023001 (2018).
- ³² A. A. Hyman, C. A. Weber, F. Jülicher, Liquid-liquid phase separation in biology. *Annu. Rev. Cell Dev. Biol.* **30**, 39–58 (2014).
- ³³ C. P. Brangwynne, P. Tompa, R. V. Pappu, Polymer physics of intracellular phase transitions. *Nat. Phys.* **11**, 899–904 (2015).
- ³⁴ Y.-H. Lin, J. D. Forman-Kay, H. S. Chan, Sequence-specific polyampholyte phase separation in membraneless organelles. *Phys. Rev. Lett.* **117**, 178101 (2016).
- ³⁵ Y.-H. Lin, J. Song, J. D. Forman-Kay, H. S. Chan, Random-phase-approximation theory for sequence-dependent, biologically functional liquid-liquid phase separation of intrinsically disordered proteins. *J. Mol. Liq.* **228**, 176–193 (2017). Corrigendum: *J. Mol. Liq.* **273**, 676 (2019).

- ³⁶ Y.-H. Lin, H. S. Chan, Phase separation and single-chain compactness of charged disordered proteins are strongly correlated. *Biophys. J.* **112**, 2043–2046 (2017).
- ³⁷ Y.-H. Lin, J. P. Brady, J. D. Forman-Kay, H. S. Chan, Charge pattern matching as a “fuzzy” mode of molecular recognition for the functional phase separations of intrinsically disordered proteins. *New J. Phys.* **19**, 115003 (2017).
- ³⁸ L.-W. Chang, T. K. Lytle, M. Radhakrishna, J. J. Madinya, J. Vélez, C. E. Sing, S. L. Perry, Sequence and entropy-based control of complex coacervates. *Nat. Comm.* **8**, 1273 (2017).
- ³⁹ J. Wang, J.-M. Choi, A. S. Holehouse, H. O. Lee, X. Zhang, M. Jahnel, S. Maharana, R. Lemaitre, A. Pozniakovsky, D. Drechsel, I. Poser, R. V. Pappu, S. Alberti, A. A. Hyman, A molecular grammar governing the driving forces for phase separation of prion-like RNA binding proteins. *Cell* **174**, 688–699 (2018).
- ⁴⁰ J. D. Schmit, J. J. Bouchard, E. W. Martin, T. Mittag, Protein network structure enables switching between liquid and gel states. *J. Am. Chem. Soc.* **142**, 874–883 (2020).
- ⁴¹ Y.-H. Lin, J. P. Brady, H. S. Chan, K. Ghosh, A unified analytical theory of heteropolymers for sequence-specific phase behaviors of polyelectrolytes and polyampholytes. *J. Chem. Phys.* **152**, 045102 (2020).
- ⁴² A. N. Amin, Y.-H. Lin, S. Das, H. S. Chan, Analytical theory for sequence-specific binary fuzzy complexes of charged intrinsically disordered proteins. *J. Phys. Chem. B* **124**, 6709–6720 (2020).
- ⁴³ Y. Lin, J. McCarty, J. N. Rauch, K. T. Delaney, K. S. Kosik, G. H. Fredrickson, J.-E. Shea, S. Han, Narrow equilibrium window for complex coacervation of tau and RNA under cellular conditions *eLife* **8**, e42571 (2019).
- ⁴⁴ J. McCarty, K. T. Delaney, S. P. O. Danielsen, G. H. Fredrickson, J.-E. Shea, Complete phase diagram for liquid-liquid phase separation of intrinsically disordered proteins. *J. Phys. Chem. Lett.* **10**, 1644–1652 (2019).
- ⁴⁵ S. P. O. Danielsen, J. McCarty, J.-E. Shea, K. T. Delaney, G. H. Fredrickson, Molecular design of self-coacervation phenomena in block polyampholytes. *Proc. Natl. Acad. Sci. U.S.A.* **116**, 8224–8232 (2019).
- ⁴⁶ S. P. O. Danielsen, J. McCarty, J.-E. Shea, K. T. Delaney, G. H. Fredrickson, Small ion effects on self-coacervation phenomena in block polyampholytes. *J. Chem. Phys.* **151**, 034904 (2019).

- ⁴⁷ S. Das, A. Eisen, Y.-H. Lin, H. S. Chan, A lattice model of charge-pattern-dependent polyampholyte phase separation. *J. Phys. Chem. B* **122**, 5418–5431 (2018).
- ⁴⁸ N. A. S. Robichaud, I. Saika-Voivod, S. Wallin, Phase behavior of blocky charge lattice polymers: Crystals, liquids, sheets, filaments, and clusters. *Phys. Rev. E* **100**, 052404 (2019).
- ⁴⁹ J.-M. Choi, F. Dar, R. V. Pappu, LASSI: A lattice model for simulating phase transitions of multivalent proteins. *PLoS Comput. Biol.* **15**, e1007028 (2019).
- ⁵⁰ G. L. Dignon, W. Zheng, Y. C. Kim, J. Mittal, Temperature-controlled liquid-liquid phase separation of disordered proteins. *ACS Cent. Sci.* **5**, 821–830 (2019).
- ⁵¹ D. Nilsson, A. Irbäck, Finite-size scaling analysis of protein droplet formation. *Phys. Rev. E* **101**, 022413 (2020).
- ⁵² G. L. Dignon, W. Zheng, Y. C. Kim, R. B. Best, J. Mittal, Sequence determinants of protein phase behavior from a coarse-grained model. *PLoS Comput. Biol.* **14**, e1005941 (2018).
- ⁵³ S. Das, A. N. Amin, Y.-H. Lin, H. S. Chan, Coarse-grained residue-based models of disordered protein condensates: Utility and limitations of simple charge pattern parameters. *Phys. Chem. Chem. Phys.* **20**, 28558–28574 (2018).
- ⁵⁴ A. Statt, H. Casademunt, C. P. Brangwynne, A. Z. Panagiotopoulos, Model for disordered proteins with strongly sequence-dependent liquid phase behavior. *J. Chem. Phys.* **152**, 075101 (2020).
- ⁵⁵ G. L. Dignon, W. Zheng, R. B. Best, Y. C. Kim, J. Mittal, Relation between single-molecule properties and phase behavior of intrinsically disordered proteins. *Proc. Natl. Acad. Sci. U.S.A.* **115**, 9929–9934 (2018).
- ⁵⁶ K. M. Ruff, T. S. Harmon, R. V. Pappu, CAMELOT: A machine learning approach for coarse-grained simulations of aggregation of block-copolymeric protein sequences. *J. Chem. Phys.* **143**, 243123 (2015).
- ⁵⁷ T. S. Harmon, A. S. Holehouse, R. V. Pappu, Differential solvation of intrinsically disordered linkers drives the formation of spatially organized droplets in ternary systems of linear multivalent proteins. *New J. Phys.* **20**, 045002 (2018).
- ⁵⁸ V. Nguemaha, H.-X. Zhou, Liquid-liquid phase separation of patchy particles illuminates diverse effects of regulatory components on protein droplet formation. *Sci. Rep.* **8**, 6728 (2018).

- ⁵⁹ A. Ghosh, K. Mazarakos, H.-X. Zhou, Three archetypical classes of macromolecular regulators of protein liquid-liquid phase separation. *Proc. Natl. Acad. Sci. U.S.A.* **116**, 19474–19483 (2019).
- ⁶⁰ E. W. Martin, A. S. Holehouse, I. Peran, M. Farag, J. J. Incicco, A. Bremer, C. R. Grace, A. Soranno, R. V. Pappu, T. Mittag, Valence and patterning of aromatic residues determine the phase behavior of prion-like domains. *Science* **367**, 694–699 (2020).
- ⁶¹ M. K. Hazra, Y. Levy, Charge pattern affects the structure and dynamics of polyampholyte condensates. *Phys. Chem. Chem. Phys.*, doi:10.1039/d0cp02764b (2020).
- ⁶² H. Cinar, S. Cinar, H. S. Chan, R. Winter, Pressure-induced dissolution and reentrant formation of condensed, liquid-liquid phase-separated elastomeric α -elastin. *Chem. Eur. J.* **24**, 8286–8291 (2018).
- ⁶³ S. Cinar, H. Cinar, H. S. Chan, R. Winter, Pressure-sensitive and osmolyte-modulated liquid-liquid phase separation of eye-lens γ -crystallins. *J. Am. Chem. Soc.* **141**, 7347–7354 (2019).
- ⁶⁴ H. Cinar, R. Oliva, Y.-H. Lin, X. Chen, M. Zhang, H. S. Chan, R. Winter, Pressure sensitivity of SynGAP/PSD-95 condensates as a model for postsynaptic densities and its biophysical and neurological ramifications. *Chem. Eur. J.* **26**, 11024–11031 (2020).
- ⁶⁵ J. P. Brady, P. J. Farber, A. Sekhar, Y.-H. Lin, R. Huang, A. Bah, T. J. Nott, H. S. Chan, A. J. Baldwin, J. D. Forman-Kay, L. E. Kay, Structural and hydrodynamic properties of an intrinsically disordered region of a germ cell-specific protein on phase separation. *Proc. Natl. Acad. Sci. U.S.A.* **114**, E8194–E8203 (2017).
- ⁶⁶ S. Roberts, V. Miao, S. Costa, J. Simon, G. Kelly, T. Shah, S. Zauscher, A. Chilkoti, Complex microparticle architectures from stimuli-responsive intrinsically disordered proteins. *Nat. Comm.* **11**, 1342 (2020).
- ⁶⁷ L. M. Salonen, M. Ellermann, F. Diederich, Aromatic rings in chemical and biological recognition: energetics and structures. *Angew. Chem. Int. Ed.* **50**, 4808–4842 (2011).
- ⁶⁸ R. M. Vernon, P. A. Chong, B. Tsang, T. H. Kim, A. Bah, P. Farber, H. Lin, J. D. Forman-Kay, Pi-Pi contacts are an overlooked protein feature relevant to phase separation. *eLife* **7**, e31486 (2018).
- ⁶⁹ J. P. Gallivan, D. A. Dougherty, Cation- π interactions in structural biology. *Proc. Natl. Acad. Sci. U.S.A.* **96**, 9459–9464 (1999).

- ⁷⁰ J. P. Gallivan, D. A. Dougherty, A computational study of cation- π interactions vs salt bridges in aqueous media: Implications for protein engineering. *J. Am. Chem. Soc.* **122**, 870–874 (2000).
- ⁷¹ P. B. Crowley, A. Golovin, Cation- π interactions in protein-protein interfaces. *Proteins* **59**, 231–239 (2005).
- ⁷² J. Song, S. C. Ng, P. Tompa, K. A. W. Lee, H. S. Chan, Polycation- π interactions are a driving force for molecular recognition by an intrinsically disordered oncoprotein family *PLoS Comput. Biol.* **9**, e1003239 (2013).
- ⁷³ T. Chen, J. Song, H. S. Chan, Theoretical perspectives on nonnative interactions and intrinsic disorder in protein folding and binding. *Curr. Opin. Struct. Biol.* **30**, 32–42 (2015).
- ⁷⁴ S. Miyazawa, R. L. Jernigan, Estimation of effective interresidue contact energies from protein crystal structures: quasi-chemical approximation. *Macromolecules* **18**, 534–552 (1985).
- ⁷⁵ S. Miyazawa, R. L. Jernigan, Residue-residue potentials with a favourable contact pair term and an unfavourable high packing density term, for simulation and threading. *J. Mol. Biol.* **256**, 623–644 (1996).
- ⁷⁶ L. H. Kapcha, P. J. Rossky, A simple atomic-level hydrophobicity scale reveals protein interfacial structure. *J. Mol. Biol.* **426**, 484–498 (2014).
- ⁷⁷ B. S. Schuster, G. L. Dignon, W. S. Tang, F. M. Kelley, A. K. Ranganath, C. N. Jahnke, A. G. Simpkins, R. M. Regy, D. A. Hammer, M. C. Good, J. Mittal, Identifying sequence perturbations to an intrinsically disordered protein that determine its phase-separation behavior. *Proc. Natl. Acad. Sci. U.S.A.* **117**, 11421–11431 (2020).
- ⁷⁸ K. S. Silmore, M. P. Howard, A. Z. Panagiotopoulos, Vapor-liquid phase equilibrium and surface tension of fully flexible Lennard-Jones chains. *Mol. Phys.* **115**, 320–327 (2017).
- ⁷⁹ Y. C. Kim, G. Hummer, Coarse-grained models for simulations of multiprotein complexes: Application to ubiquitin binding. *J. Mol. Biol.* **375**, 1416–1433 (2008).
- ⁸⁰ A. C. Murthy, G. L. Dignon, Y. Kan, G. H. Zerze, S. H. Parekh, J. Mittal, N. L. Fawzi, Molecular interactions underlying liquid-liquid phase separation of the FUS low-complexity domain. *Nat. Struct. Mol. Biol.* **26**, 637–648 (2019).
- ⁸¹ A. E. Conicella, G. L. Dignon, G. H. Zerze, H. B. Schmidt, A. M. D’Ordine, Y. C. Kim, R. Rohatgi, Y. M. Ayala, J. Mittal, N. L. Fawzi, TDP-43 α -helical structure

- tunes liquid-liquid phase separation and function. *Proc. Natl. Acad. Sci. U.S.A.* **117**, 5883–5894 (2020).
- ⁸² F. G. Quiroz, A. Chilkoti, Sequence heuristics to encode phase behaviour in intrinsically disordered protein polymers. *Nat. Mater.* **14**, 1164–1171 (2015).
- ⁸³ K. Kumar, S. M. Woo, T. Siu, W. A. Cortopassi, F. Duarte, R. S. Paton, Cation- π interactions in protein-ligand binding: theory and data-mining reveal different roles for lysine and arginine. *Chem. Sci.* **9**, 2655–2665 (2018).
- ⁸⁴ R. V. Pappu, X. Wang, A. Vitalis, S. L. Crick, A polymer physics perspective on driving forces and mechanisms for protein aggregation. *Arch. Biochem. Biophys.* **469**, 132–141 (2008).
- ⁸⁵ D. R. DeVido, J. G. Dorsey, H. S. Chan, K. A. Dill, Oil/water partitioning has a different thermodynamic signature when the oil solvent chains are aligned than when they are amorphous. *J. Phys. Chem. B* **102**, 7272–7279 (1998).
- ⁸⁶ P. A. Karplus, Hydrophobicity regained. *Protein Sci.* **6**, 1302–1307 (1997).
- ⁸⁷ H. S. Chan, K. A. Dill, Solvation: How to obtain microscopic energies from partitioning and solvation experiments. *Annu. Rev. Biophys. Biomol. Struct.* **26**, 425–459 (1997).
- ⁸⁸ H. S. Chan, Amino acid side-chain hydrophobicity. In: *eLS, Encyclopedia of Life Sciences*. John Wiley & Sons Ltd, Chichester, U.K. (2002). <http://www.els.net> [doi: 10.1038/npg.els.0003005].
- ⁸⁹ J. L. Fauchère, V. Pliška, Hydrophobic parameters II of amino-acid side chains from the partitioning of N-acetyl-amino-acid amides. *Eur. J. Med. Chem.* **18**, 369–375 (1983).
- ⁹⁰ H. S. Chan, Folding alphabets. *Nat. Struct. Biol.* **6**, 994–996 (1999).
- ⁹¹ C. N. Pace, G. Horn, E. J. Hebert, J. Bechert, K. Shaw, L. Urbanikova, J. M. Scholtz, J. Sevcik, Tyrosine hydrogen bonds make a large contribution to protein stability. *J. Mol. Biol.* **312**, 393–404 (2001).
- ⁹² G. D. Rose, A. R. Geselowitz, G. J. Lesser, R. H. Lee, M. H. Zehfus, Hydrophobicity of amino acid residues in globular proteins. *Science* **229**, 834–838 (1985).
- ⁹³ M. S. Moghaddam, S. Shimizu, H. S. Chan, Temperature dependence of three-body hydrophobic interactions: Potential of mean force, enthalpy, entropy, heat capacity, and nonadditivity. *J. Am. Chem. Soc.* **127**, 303–316 (2005).
- ⁹⁴ J. L. MacCallum, M. S. Moghaddam, H. S. Chan, D. P. Tieleman, Hydrophobic association of α -helices, steric dewetting, and enthalpic barriers to protein folding. *Proc. Natl. Acad. Sci. U.S.A.* **104**, 6206–6210 (2007).

- ⁹⁵ R. H. Wood, P. T. Thompson, Differences between pair and bulk hydrophobic interactions. *Proc. Natl. Acad. Sci. U.S.A.* **87**, 946–949 (1990).
- ⁹⁶ M. Makowski, E. Sobolewski, C. Czaplewski, A. Liwo, S. Oldziej, J. H. No, H. A. Scheraga, Simple physics-based analytical formulas for the potentials of mean force for the interaction of amino acid side chains in water. 3. Calculation and parameterization of the potentials of mean force of pairs of identical hydrophobic side chains. *J. Phys. Chem. B* **111**, 2925–2931 (2007).
- ⁹⁷ M. Makowski, E. Sobolewski, C. Czaplewski, S. Oldziej, A. Liwo, H. A. Scheraga, Simple physics-based analytical formulas for the potentials of mean force for the interaction of amino acid side chains in water. IV. Pairs of different hydrophobic side chains. *J. Phys. Chem. B* **112**, 11385–11395 (2008).
- ⁹⁸ J. J. Dwyer, A. G. Gittis, D. A. Karp, E. E. Lattman, D. S. Spencer, W. E. Stites, B. García-Moreno E, High apparent dielectric constants in the interior of a protein reflect water penetration. *Biophys. J.* **79**, 1610–1620 (2000).
- ⁹⁹ J. W. Pitera, M. Falta, W. F. van Gunsteren, Dielectric properties of proteins from simulation: The effects of solvent, ligands, pH, and temperature. *Biophys. J.* **80**, 2546–2555 (2001).
- ¹⁰⁰ C. N. Schutz, A. Warshel, What are the dielectric “constants” of proteins and how to validate electrostatic models? *Proteins* **44**, 400–417 (2001).
- ¹⁰¹ T. Rudas, C. Schröder, S. Boresch, O. Steinhauser, Simulation studies of the protein-water interface. II. Properties at the mesoscopic resolution. *J. Chem. Phys.* **124**, 234908 (2006).
- ¹⁰² H. Nymeyer, H.-X. Zhou, A method to determine dielectric constants in nonhomogeneous systems: Application to biological membranes. *Biophys. J.* **94**, 1185–1193 (2008).
- ¹⁰³ M. Tros, L. Zheng, J. Hunger, M. Bonn, D. Bonn, G. J. Smits, S. Woutersen, Picosecond orientational dynamics of water in living cells. *Nat. Commun.* **8**, 904 (2017).
- ¹⁰⁴ J. Wyman, Jr., Studies on the dielectric constant of protein solutions. I. Zein. *J. Biol. Chem.* **90**, 443–476 (1931).
- ¹⁰⁵ N. Martin, Dynamic synthetic cells based on liquid-liquid phase separation. *ChemBioChem* **20**, 2553–2568 (2019).
- ¹⁰⁶ M. J. Abraham, D. van der Spoel, E. Lindahl, B. Hess, and the GROMACS development team. *GROMACS User Manual version 2016.5*; 2018. <http://www.gromacs.org>.

- ¹⁰⁷ K. Lindorff-Larsen, S. Piana, K. Palmo, P. Maragakis, J. L. Klepeis, R. O. Dror, D. E. Shaw, Improved side-chain torsion potentials for the Amber ff99SB protein force field. *Proteins*, **78**, 1950–1958 (2010).
- ¹⁰⁸ W. L. Jorgensen, J. Chandrasekhar, J. D. Madura, R. W. Impey, M. L. Klein, Comparison of simple potential functions for simulating liquid water. *J. Chem. Phys.* **79**, 926–935 (1983).
- ¹⁰⁹ H. J. C. Berendsen, J. R. Grigera, T. P. Straatsma, The missing term in effective pair potentials. *J. Phys. Chem.* **91**, 6269–6271 (1987).
- ¹¹⁰ W. Humphrey, A. Dalke, K. Schulten, VMD - Visual Molecular Dynamics. *J. Molec. Graphics*, **14**, 33–38 (1996).
- ¹¹¹ J. Hsin, A. Arkhipov, Y. Yin, J. E. Stone, K. Schulten, Using VMD: an introductory tutorial. *Curr. Protoc. Bioinform.* **24**, 5.7.1-5.7.48 (2008).
- ¹¹² W. L. Bragg, A. B. Pippard, The form birefringence of macromolecules. *Acta Cryst.* **6**, 865–867 (1953).
- ¹¹³ J. B. Hasted, D. M. Ritson, C. H. Collie, Dielectric properties of aqueous ionic solutions. Parts I and II. *J. Chem. Phys.* **16**, 1–21 (1948).
- ¹¹⁴ A. Levy, D. Andelman, H. Orland, Dielectric constant of ionic solutions: A field-theory approach. *Phys. Rev. Lett.* **108**, 227801 (2012).
- ¹¹⁵ Z.-G. Wang, Fluctuation in electrolyte solutions: The self energy. *Phys. Rev. E* **81**, 021501 (2010).
- ¹¹⁶ G. Orkoulas, S. K. Kumar, A. Z. Panagiotopoulos, Monte Carlo study of Coulombic criticality in polyelectrolytes. *Phys. Rev. Lett.* **90**, 048303 (2003).
- ¹¹⁷ J. D. Schmit, K. A. Dill, The stabilities of protein crystals. *J. Phys. Chem. B* **114**, 4020–4027 (2010).
- ¹¹⁸ G. J. Martyna, D. J. Tobias, M. L. Klein, Constant pressure molecular dynamics algorithms. *J. Chem. Phys.* **101**, 4177–4189 (1994).
- ¹¹⁹ M. E. Tuckerman, J. Alejandre, R. López-Rendón, A. L. Jochim, G. J. Martyna, A Liouville-operator derived measure-preserving integrator for molecular dynamics simulations in the isothermal-isobaric ensemble. *J. Phys. A: Math. Gen.* **39**, 5629–5651 (2006).
- ¹²⁰ J. A. Anderson, C. D. Lorenz, A. Travesset, General purpose molecular dynamics simulations fully implemented on graphics processing units. *J. Comput. Phys.* **227**, 5342–5359 (2008).

- ¹²¹ J. Glaser, T. D. Nguyen, J. A. Anderson, P. Lui, F. Spiga, J. A. Millan, D. C. Morse, S. C. Glotzer, Strong scaling of general-purpose molecular dynamics simulations on GPUs. *Comput. Phys. Commun.* **192**, 97–107 (2015).
- ¹²² W. L. DeLano, *The PyMOL Molecular Graphics System*; DeLano Scientific: Palo Alto, California, USA, 2002. <http://www.pymol.org/>.
- ¹²³ L. Martínez, R. Andrade, E. G. Birgin, J. M. Martínez, PACKMOL: A package for building initial configurations for molecular dynamics simulations. *J. Comput. Chem.* **30**, 2157–2164 (2009).
- ¹²⁴ B. Hess, H. Bekker, H. J. C. Berendsen, J. G. E. M. Fraaije, LINCS: A linear constraint solver for molecular simulations. *J. Comp. Chem.* **18**, 1463–1472 (1997).
- ¹²⁵ R. W. Hockney, S. P. Goel, J. Eastwood, Quiet high resolution computer models of a plasma. *J. Comp. Phys.* **14**, 148–158 (1974).
- ¹²⁶ U. Essmann, L. Perera, M. L. Berkowitz, T. Darden, H. Lee, L. G. Pedersen, A smooth particle mesh Ewald potential. *J. Chem. Phys.* **103**, 8577–8592 (1995).
- ¹²⁷ G. Bussi, D. Donadio, M. Parrinello, Canonical sampling through velocity rescaling. *J. Chem. Phys.* **126**, 014101 (2007).
- ¹²⁸ H. J. C. Berendsen, J. P. M. Postma, A. DiNola, J. R. Haak, Molecular dynamics with coupling to an external bath. *J. Chem. Phys.* **81**, 3684–3690 (1984).
- ¹²⁹ M. Parrinello, A. Rahman, Polymorphic transitions in single crystals: A new molecular dynamics method. *J. Appl. Phys.* **52**, 7182–7190 (1981).
- ¹³⁰ S. Nosé, M. L. Klein, Constant pressure molecular dynamics for molecular systems. *Mol. Phys.* **50**, 1055–1076 (1983).
- ¹³¹ S. Floros, M. Liakopoulou-Kyriakides, K. Karatasos, G. E. Papadopoulos, Detailed study of the dielectric function of a lysozyme solution studied with molecular dynamics simulations. *Eur. Biophys. J.* **44**, 599–611 (2015).
- ¹³² J. D. Jackson, *Classical Electrodynamics*, 2nd edition (Wiley, New York 1975), pp. 154–155.
- ¹³³ V. A. Markel, Introduction to the Maxwell Garnett approximation: Tutorial *J. Opt. Soc. Am. A* **33**, 1244–1256 (2016).
- ¹³⁴ Q. Wang, T. Taniguchi, G. H. Fredrickson, Self-consistent field theory of polyelectrolyte systems. *J. Phys. Chem. B* **108**, 6733–6744 (2004).
- ¹³⁵ M. P. Allen, D. J. Tildesley, *Computer Simulation of Liquids* (Oxford University Press, New York, 1987).